Integrating Deep Learning into Digital Rock Analysis Workflow

Author:
Alqahtani, Naif

Publication Date:
2021

DOI:
https://doi.org/10.26190/unsworks/22841

Integrating Deep Learning into Digital Rock Analysis Workflow

by

Naif J. Alqahtani

A thesis submitted in fulfillment of the
requirements for the degree of
Doctor of Philosophy at

The University of New South Wales

UNSW
SYDNEY

School of Minerals and Energy Resources Engineering
Faculty of Engineering

Ph.D. Advisors:

A/Prof. Peyman Mostaghimi, UNSW

A/Prof. Ryan T. Armstrong, UNSW

Dr. Pawel Swietojanski, UNSW

August 2021

UNSW SYDNEY | Australia's Global University

Thesis/Dissertation Sheet

Surname/Family Name	:	**Alqahtani**
Given Name/s	:	**Naif J.**
Abbreviation for degree as give in the University calendar	:	**Ph.D.**
Faculty	:	**Engineering**
School	:	**Minerals and Energy Resources Engineering**
Thesis Title	:	**Integrating Deep Learning into Digital Rock Analysis Workflow**

Abstract 350 words maximum:

Digital Rock Analysis (DRA) has expanded our knowledge about natural phenomena in various geoscience specialties. DRA as an emerging technology has limitations including (1) the trade-off between the size of spatial domain and resolution, (2) methodological and human-induced errors in segmentation, and (3) the computational costs associated with intensive modeling. Deep learning (DL) methods are utilized to alleviate these limitations.

First, two DL frameworks are utilized to probe the performance gains from using Convolutional Neural Networks (CNN) to super-resolve and segment real multi-resolution X-ray images of complex carbonate rocks. The first framework experiments the applications of U-Net and U-ResNet architectures to obtain macropore, solid, and micropore segmented images in an end-to-end scheme. The second framework segregates the super-resolution and segmentation into two networks: EDSR and U-ResNet. Both frameworks show consistent performance indicated by the voxel-wise accuracy metrics, the measured phase morphology, and flow characteristics. The end-to-end frameworks are shown to be superior to using a segregated approach confirming the adequacy of end-to-end learning for performing complex tasks.

Second, CNNs accuracy margins in estimating physical properties of porous media 2d X-ray images are investigated. Binary and greyscale sandstone images are used as an input to CNNs architectures to estimate porosity, specific surface area, and average pore size of three sandstone images. The results show encouraging margins of accuracy where the error in estimating these properties can be up to 6% when using binary images and up to 7% when using greyscale images.

Third, the suitability of CNNs as regression tools to predict a more challenging property, permeability, is investigated. Two complex CNNs architectures (ResNet and ResNext) are applied to learn the morphology of pore space in 3D porous media images for flow-based characterization. The dataset includes more than 29,000 3d subvolumes of multiple sandstone and carbonates rocks. The findings show promising regression accuracy using binary images. Accuracy gains are observed using conductivity maps as an input to the networks. Permeability inference on unseen samples can be achieved in 120 ms/sample with an average relative error of 18.9%.

This thesis demonstrates the significant potential of deep learning in improving DRA capabilities.

ORIGINALITY STATEMENT

'I hereby declare that this submission is my own work and to the best of my knowledge it contains no materials previously published or written by another person, or substantial proportions of material which have been accepted for the award of any other degree or diploma at UNSW or any other educational institution, except where due acknowledgement is made in the thesis. Any contribution made to the research by others, with whom I have worked at UNSWor elsewhere, is explicitly acknowledged in the thesis. I also declare that the intellectual content of this thesis is the product of my own work, except to the extent that assistance from others in the project's design and conception or in style, presentation and linguistic expression is acknowledged.'

Signed …….....

Date ……18/8/2021…….....

COPYRIGHT STATEMENT

'I hereby grant the University of New South Wales or its agents a non-exclusive licence to archive and to make available (including to members of the public) my thesis or dissertation in whole or part in the University libraries in all forms of media, now or here after known. I acknowledge that I retain all intellectual property rights which subsist in my thesis or dissertation, such as copyright and patent rights, subject to applicable law. I also retain the right to use all or part of my thesis or dissertation in future works (such as articles or books).'

'For any substantial portions of copyright material used in this thesis, written permission for use has been obtained, or the copyright material is removed from the final public version of the thesis.'

Signed …….. …….....

Date ……6/12/2021…….....

AUTHENTICITY STATEMENT

'I certify that the Library deposit digital copy is a direct equivalent of the final officially approved version of my thesis.'

Signed …….. …….....

Date ……6/12/2021…….....

INCLUSION OF PUBLICATIONS STATEMENT

UNSW is supportive of candidates publishing their research results during their candidature as detailed in the UNSW Thesis Examination Procedure.

Publications can be used in their thesis in lieu of a Chapter if:

- The candidate contributed greater than 50% of the content in the publication and is the "primary author", ie. the candidate was responsible primarily for the planning, execution and preparation of the work for publication
- The candidate has approval to include the publication in their thesis in lieu of a Chapter from their supervisor and Postgraduate Coordinator.
- The publication is not subject to any obligations or contractual agreements with a third party that would constrain its inclusion in the thesis

Please indicate whether this thesis contains published material or not:

☐ This thesis contains no publications, either published or submitted for publication
(if this box is checked, you may delete all the material on page 2)

☐ Some of the work described in this thesis has been published and it has been documented in the relevant Chapters with acknowledgement
(if this box is checked, you may delete all the material on page 2)

☒ This thesis has publications (either published or submitted for publication) incorporated into it in lieu of a chapter and the details are presented below

CANDIDATE'S DECLARATION

I declare that:

- I have complied with the UNSW Thesis Examination Procedure
- where I have used a publication in lieu of a Chapter, the listed publication(s) below meet(s) the requirements to be included in the thesis.

Candidate's Name	**Signature**	**Date (dd/mm/yy)**
Naif J. Alqahtani		18/08/2021

POSTGRADUATE COORDINATOR'S DECLARATION *To only be filled in where publications are used in lieu of Chapters*

I declare that:

- the information below is accurate
- where listed publication(s) have been used in lieu of Chapter(s), their use complies with the UNSW Thesis Examination Procedure
- the minimum requirements for the format of the thesis have been met.

PGC's Name	PGC's Signature	Date (dd/mm/yy)
Ryan Armstrong		**7/12/2021**

For each publication incorporated into the thesis in lieu of a Chapter, provide all of the requested details and signatures required

Details of publication #1:

Full title: Machine Learning for Predicting Properties of Porous Media from 2D X-ray Images

Authors: Naif J Alqahtani, Fatimah Alzubaidi, Ryan T Armstrong, Pawel Swietojanski, and Peyman Mostaghimi

Journal or book name: Journal of Petroleum Science and Engineering

Volume/page numbers: 184 / 106514

Date accepted/ published: 19 Sep 2019 / 26 Sep 2019

Status	*Published*	***X***	*Accepted and In press*		*In progress (submitted)*	

The Candidate's Contribution to the Work

Naif Alqahtani has contributed to more than 50% of this work

Location of the work in the thesis and/or how the work is incorporated in the thesis:

Chapter 3

PRIMARY SUPERVISOR'S DECLARATION

I declare that:

- the information above is accurate
- this has been discussed with the PGC and it is agreed that this publication can be included in this thesis in lieu of a Chapter
- All of the co-authors of the publication have reviewed the above information and have agreed to its veracity by signing a 'Co-Author Authorisation' form.

Primary Supervisor's name	Primary Supervisor's signature	Date (dd/mm/yy)
Peyman Mostaghimi		**7/12/2021**

Details of publication #2:

Full title Flow-Based Characterization of Digital Rock Images Using Deep Learning

Authors: Naif J Alqahtani, Traiwit Chung, Ying Da Wang, Ryan T Armstrong, Pawel Swietojanski, and Peyman Mostaghimi

Journal or book name: SPE Journal

Volume/page numbers: 1-12

Date accepted/ published: 04 Feb 2021 / 24 March 2021

Status	*Published*	***X***	*Accepted and In press*		*In progress (submitted)*	

The Candidate's Contribution to the Work

Naif Alqahtani has contributed to more than 50% of this work

Location of the work in the thesis and/or how the work is incorporated in the thesis:

Chapter 4

PRIMARY SUPERVISOR'S DECLARATION

I declare that:

- the information above is accurate
- this has been discussed with the PGC and it is agreed that this publication can be included in this thesis in lieu of a Chapter
- All of the co-authors of the publication have reviewed the above information and have agreed to its veracity by signing a 'Co-Author Authorisation' form.

Primary Supervisor's name	**Primary Supervisor's signature**	**Date (dd/mm/yy)**
Peyman Mostaghimi		**7/12/2021**

Details of publication #3:

Full title: Super-Resolved Segmentation of X-ray Images of Carbonate Rocks using Deep Learning

Authors: Naif J. Alqahtani, Yufu Niu, Ying Da Wang, Traiwit Chung, Zakhar Lanetc, Aleksandra Zhuravljov, Ryan T. Armstrong, and Peyman Mostaghimi

Journal or book name: Transport in Porous Media

Volume/page numbers: NA

Date accepted/ published: Under Review

Status	*Published*		*Accepted and In press*		*In progress (submitted)*	***X***

The Candidate's Contribution to the Work

Naif Alqahtani has contributed to more than 50% of this work

Location of the work in the thesis and/or how the work is incorporated in the thesis:

Chapter 2

PRIMARY SUPERVISOR'S DECLARATION

I declare that:

- the information above is accurate
- this has been discussed with the PGC and it is agreed that this publication can be included in this thesis in lieu of a Chapter
- All of the co-authors of the publication have reviewed the above information and have agreed to its veracity by signing a 'Co-Author Authorisation' form.

Primary Supervisor's name	**Primary Supervisor's signature**	**Date (dd/mm/yy)**
Peyman Mostaghimi		**7/12/2021**

Dedication

I dedicate this thesis to my late grandmothers,

Zuhrah Bint Sehmah & Aisha Bint Khalifah

for their words of wisdom and infinite love.

may God grant you peace and mercy

Table of Contents

List of Figures

List of Tables

List of Abbreviations and Symbols

Abbreviation	Definition
ANN	Artificial Neural Network
APS	Average Pore Size

BN	Batch Normalization
CAC	Converging Active Contour
CCA	Conventional Core Analysis
CNN	Convolutional Neural Network
CPU	Central Processing Unit
micro-CT	Micro-Computed Tomography
DL	Deep Learning
DNS	Direct Numerical Simulation
DRA	Digital Rock Analysis
EDSR	Enhanced Deep Residual Network
EVS	Explained Variance Score
FC	Fully Connected (Layer)
GAN	Generative Adversarial Network
GPU	Graphics Processing Unit
GT	Ground Truth
HR	High Resolution
IEA	International Energy Agency
IUPAC	International Union of Pure and Applied Chemistry
LR	Low Resolution
MAE	Mean Absolute Error
MARE	Mean Absolute Relative Error
MICP	Mercury Intrusion Capillary Pressure
ML	Machine Learning
MLP	Multi-Layer Perceptron

MRCCM	Multi-Resolution Complex Carbonates Micro-CT Dataset
MSE	Mean Squared Error
MTL	Multi-Task Learning
NN	Neural Network
PFVS	Pore-scale Finite Volume Solver
PNM	Pore Network Modeling
REV	Representative Elementary Volume
RLU	Rectified Linear Unit
RMSE	Root Mean Squared Error
ROI	Region of Interest
SCAL	Special Core Analysis
SEM	Scanning Electron Microscopy
SSA	Specific Surface Area

Symbol	**Definition**
$\boldsymbol{z^l}$	Linear neuron or filter output (before activation)
$\boldsymbol{W^l}$	Weights of the l-th layer
$\boldsymbol{x}$	Layer input
$\boldsymbol{b^l}$	Bias of the l-th layer
$\boldsymbol{EC}$	Euler-Poincare Characteristic
V	Numbers of vertices of a volume
$\mathrm{\epsilon}$	Numbers of edges of a volume
$\boldsymbol{\mathcal{F}}$	Numbers of faces of a volume
$\boldsymbol{\mathcal{L}}$	Numbers of solids of a volume
$\boldsymbol{K}$	Absolute permeability, [L^2]

$\boldsymbol{R}$	Resolution [L]
$\boldsymbol{h^l}$	Activated neuron or filter output
$\boldsymbol{f^l}$	Non-linear activation function
$\boldsymbol{K^l{}_p}$	the p-th filter kernel at the l-th layer
$\boldsymbol{\delta}$	Huber loss scalar
$\boldsymbol{w}$	Local voxel conductivity, [$LM^{-1}T$]
$\boldsymbol{d_{max}}$	Digital equivalent of the largest inscribed radius, [voxels]
$\boldsymbol{d}$	Digital equivalent of the radial distance from the inner wall, [voxels]
$\boldsymbol{\mu}$	Fluid viscosity, [MLT^{-2}]
$\boldsymbol{A_j}$	The ground truth value of the j-th sample
$\boldsymbol{P_j}$	The predicted value of the j-th sample

List of Journal Publications

1- **Alqahtani, Naif J.,** Alzubaidi, Fatimah, Armstrong, Ryan T., Mostaghimi, Peyman. 2020. "*Machine learning for predicting properties of porous media from 2d X-ray images*". Journal of Petroleum Science and Engineering 184: 106514.
doi: https://doi.org/10.1016/j.petrol.2019.106514

2- **Alqahtani, Naif J.,** Chung, Traiwit, Wang, Ying Da, Armstrong, Ryan T., Swietojanski, Pawel, Mostaghimi, Peyman. 2021 *"Flow-Based Characterization of Digital Rock Images Using Deep Learning."* SPE J.
doi: https://doi.org/10.2118/205376-PA

3- **Alqahtani, Naif J.,** Niu, Yufu, Wang, Ying Da, Chung, Traiwit, Lanetc, Zakhar, Zhuravljov, Aleksandr, Armstrong, Ryan T., Mostaghimi, Peyman. 2021. *"Super-Resolved Segmentation of X-ray Carbonate Rock Images for Improved Sub-Resolution Porosity Identification"*, Under review in Transport in Porous Media.

4- Alzahid, Yara A., Mostaghimi, Peyman, **Alqahtani, Naif J.,** Sun, Chenhao, Lu, Xiao, Armstrong, Ryan T. 2019. "Oil mobilization and solubilization in porous media by in situ emulsification". Journal of Colloid and Interface Science 554: 554-564
doi: https://doi.org/10.1016/j.jcis.2019.07.009

List of Conference Publications

1- **Alqahtani, Naif J.,** Armstrong, Ryan T., and Peyman Mostaghimi. *"Deep Learning Convolutional Neural Networks to Predict Porous Media Properties."* Paper presented at the SPE Asia Pacific Oil and Gas Conference and Exhibition, Brisbane, Australia, October 2018.
doi: https://doi.org/10.2118/191906-MS

2- Ar Rushood, Ibrahim , **Alqahtani, Naif J.,** Wang, Ying Da, Shabaninejad, Mehdi , Armstrong, Ryan , and Peyman Mostaghimi. *"Segmentation of X-Ray Images of Rocks Using Deep Learning."* Paper presented at the SPE Annual Technical Conference and Exhibition, Virtual, October 2020.
doi: https://doi.org/10.2118/201282-MS

Acknowledgments

First and foremost, I would like to thank Allah (God) for his endless grace upon me.

Throughout my time at The University of New South Wales (UNSW), there have been several people who helped me complete this work. To begin with, I'm deeply indebted to my main thesis supervisor Associate Prof. Peyman Mostaghimi for his guidance, friendship, and advice. From day one, he has been supportive and patient which helped me overcome many challenges in my research. I would like to pay regard to my thesis co-supervisors Associate Prof. Ryan Armstrong and Dr. Pawel Swietojanski for their constructive feedback and remarkable technical assistance. They have helped me formulate many of the ideas involved in this work. I am sincerely obliged to have such excellent advisors.

I would like to acknowledge my fellow academics in the Multiscale Transport in Porous Media Systems (MUTRIS). Special thanks go to my co-authors Dr. Traiwit, Dr. Ying, Fatimah, Zakhar, and Yufu. I also would like to acknowledge our laboratory manager Mr. Nino, and UNSW Tyree X-ray Imaging facility officer Dr. Amalia for their help in the laboratory and imaging work involved in my thesis. I'm grateful to Saudi Aramco and EXPEC Advanced Research Centre for sponsoring my education at UNSW. Special thanks go to my friends at UNSW: Dr. Faisal, Dr. Abdulaziz, Dr. Mohammed, Suleiman, Moath, Abdulmajeed, Hamad, Ibrahim, and Hussain. Thanks for the memories!

Lastly but by no means least, I would like to thank my family without whom I endure no chance of completing this work. I am beyond indebted to my parents for their encouragement, love, and prayers. My sincere thanks to my beloved, supportive, and patient wife Raghad. To my beloved brothers, sisters, uncles, aunties, and cousins back in Saudi Arabia, thanks for your love and support. Many thanks go to my bigger family here in Australia, the Gracie Barra St. Peters Family. The friendships and memories I made will last forever.

Thesis Abstract

Digital Rock Analysis (DRA) has expanded our knowledge about natural phenomena in various geoscience specialties. DRA as an emerging technology has limitations including (1) the trade-off between the size of spatial domain and resolution, (2) methodological and human-induced errors in segmentation, and (3) the computational costs associated with intensive modeling. Deep learning (DL) methods are utilized to alleviate these limitations.

First, two DL frameworks are utilized to probe the performance gains from using Convolutional Neural Networks (CNN) to super-resolve and segment real multi-resolution X-ray images of complex carbonate rocks. The first framework experiments the applications of U-Net and U-ResNet architectures to obtain macropore, solid, and micropore segmented images in an end-to-end scheme. The second framework segregates the super-resolution and segmentation into two networks: EDSR and U-ResNet. Both frameworks show consistent performance indicated by the voxel-wise accuracy metrics, the measured phase morphology, and flow characteristics. The end-to-end frameworks are shown to be superior to using a segregated approach confirming the adequacy of end-to-end learning for performing complex tasks.

Second, CNNs accuracy margins in estimating physical properties of porous media 2d X-ray images are investigated. Binary and greyscale sandstone images are used as an input to CNNs architectures to estimate porosity, specific surface area, and average pore size of three sandstone images. The results show encouraging margins of accuracy where the error in estimating these properties can be up to 6% when using binary images and up to 7% when using greyscale images.

Third, the suitability of CNNs as regression tools to predict a more challenging property, permeability, is investigated. Two complex CNNs architectures (ResNet and ResNext) are applied to learn the morphology of pore space in 3D porous media images for flow-based characterization. The dataset includes more than 29,000 3d subvolumes of multiple sandstone and carbonates rocks. The findings show promising regression accuracy using binary images. Accuracy gains are observed using conductivity maps as an input to the networks. Permeability inference on unseen samples can be achieved in 120 ms/sample with an average relative error of 18.9%.

This thesis demonstrates the significant potential of deep learning in improving DRA capabilities.

1 Introduction

X-ray tomographic imaging and modeling of rocks, commonly referred to as Digital Rock Analysis (DRA), has notably expanded our geoscientific knowledge over the last few decades [1-4]. The tomographic images obtained through DRA technology provide unprecedented detail of porous media internal geometry, capable of resolving pore structures down to a few micrometers or even sub-micrometers [3, 5]. Digital rocks offer a prompt method for studying many aspects related to rocks and porous materials in general. This has helped address questions on such diverse topics as contaminant and reactive transport [6-8], carbon dioxide (CO_2) sequestration [9-14], geomechanics [15, 16], and hydrocarbon recovery [17-19].

The digital nature of the analyses and frameworks in DRA makes it a suitable candidate for Machine Learning (ML) and Computer Vision applications [20, 21]. These applications include the automation of routine analyses [22-24], especially those that require time-consuming human interferences. Other applications include the reduction of the uncertainty associated with human error and hardware limitations [25], predictive modeling [26, 27], and the scalability to demanding datasets and projects occasionally referred to as “Big Data.” Deep Learning (DL) [28] has emerged as a branch of ML, with many breakthroughs impacting diverse scientific sectors such as medical imaging [29, 30] and remote sensing [31]. DL utilizes a family of algorithms called Neural Networks (NNs) [32] to learn specific tasks from the representation of input signals such as photographic and volumetric images. DL and NNs will be further discussed in section 1.4.1. With major improvements in imaging and computing capabilities, DL training strategies, and network design, the coupling of DRA and DL has attracted growing

interest in many geoscientific research areas, as illustrated by the increase in publications depicted in Figure 1-1. This increase is due to the spread of feasible high-resolution X-ray imaging instruments and the growth in computational power available in modern Graphics Processing Units (GPU). This enables sophisticated DL models for various DRA applications to be trained using larger datasets that include volumetric images of rocks [33].

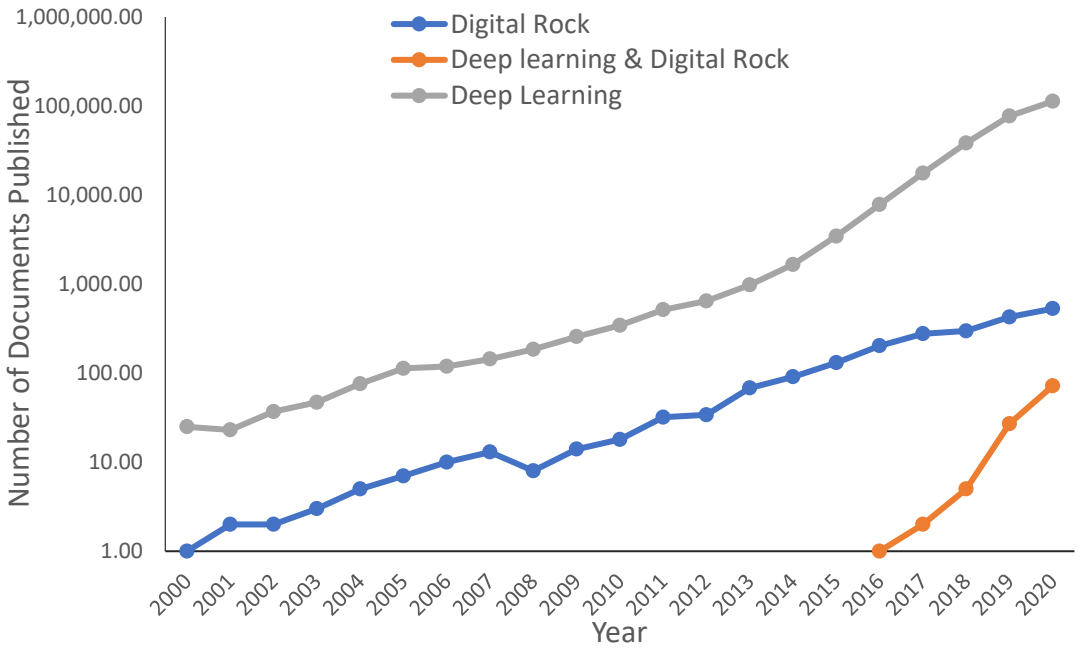

Figure 1-1: The increase in the number of documents published per year that includes "Digital Rock", "Deep Learning", and both keywords together. Source Data is retrieved from Scopus (27 July 2021).

1.1 Digital Rock Analysis in Petroleum Engineering

The worldwide demand for and consumption of energy is expected to continue to rise, due to population growth and industrialization. The International Energy Agency (IEA), one of the world's largest bodies providing analyses and data on the topic of global energy, publishes an annual report showing global energy trends in supply and consumption. Figure 1-2 shows these trends from the 2020 report (IEA, 2020). The highest three energy sources in the figure are extracted from underground reserves and are inherently finite.

The introduction of DRA as technology for reservoir rock characterization has gained the attention of many giant oil & gas companies, including Schlumberger, Saudi Aramco, Halliburton, and Shell [34-39]. Many of these companies have launched startup projects offering full digital core analysis services. DRA is seen as having potential to reduce the expenses, time, and uncertainty when making investment decisions in devolving reservoir prospects [40].

Every year, thousands of meters in depth of reservoir rock samples are unearthed during coring operations globally for formation evaluation [41, 42]. Such rock samples are examined in the laboratory through Conventional Core Analysis (CCA) [41, 43] and Special Core Analysis (SCAL) [44, 45]. CCA determines basic rock physical properties such as porosity, grain density, and air permeability [42]. Samples representing the reservoir average properties based on CCA are then subjected to SCAL to determine other physical properties such as relative permeability, wettability, and capillarity characteristics [42]. Although CCA and SCAL help characterize rocks and fluids in the reservoir, these analyses can be extremely time-consuming. Usually, a core plug sample is taken every foot from

the coring barrel containing reservoir core in conventional reservoirs [41]. From working in core analysis, the author has found that running a full spectrum of CCA and SCAL on an entire reservoir core material composed of 300 core plugs takes at least several months due to the slow nature of analyses. This hinders the ability to quickly evaluate reservoir prospects in order to make timely decisions regarding field development. DRA provides a complementary alternative to reduce the uncertainty in field development [46, 47]. The field of view in DRA usually encapsulates representative domains of typical reservoir rocks and still possess fine resolution capturing important pore structure details for estimating properties of the rock [1, 2, 47]. Moreover, the time required to complete rock characterization is an order of magnitude lower than that associated with CCA and SCAL, because multiple analyses and simulations can be run in parallel. The estimated time to carry out a full DRA study that includes imaging, image processing, and modeling can range from few hours to several days, depending on image size in voxels [48, 49].

The following sub-sections discuss frameworks involved in DRA technology and provide an introductory explanation of DL.

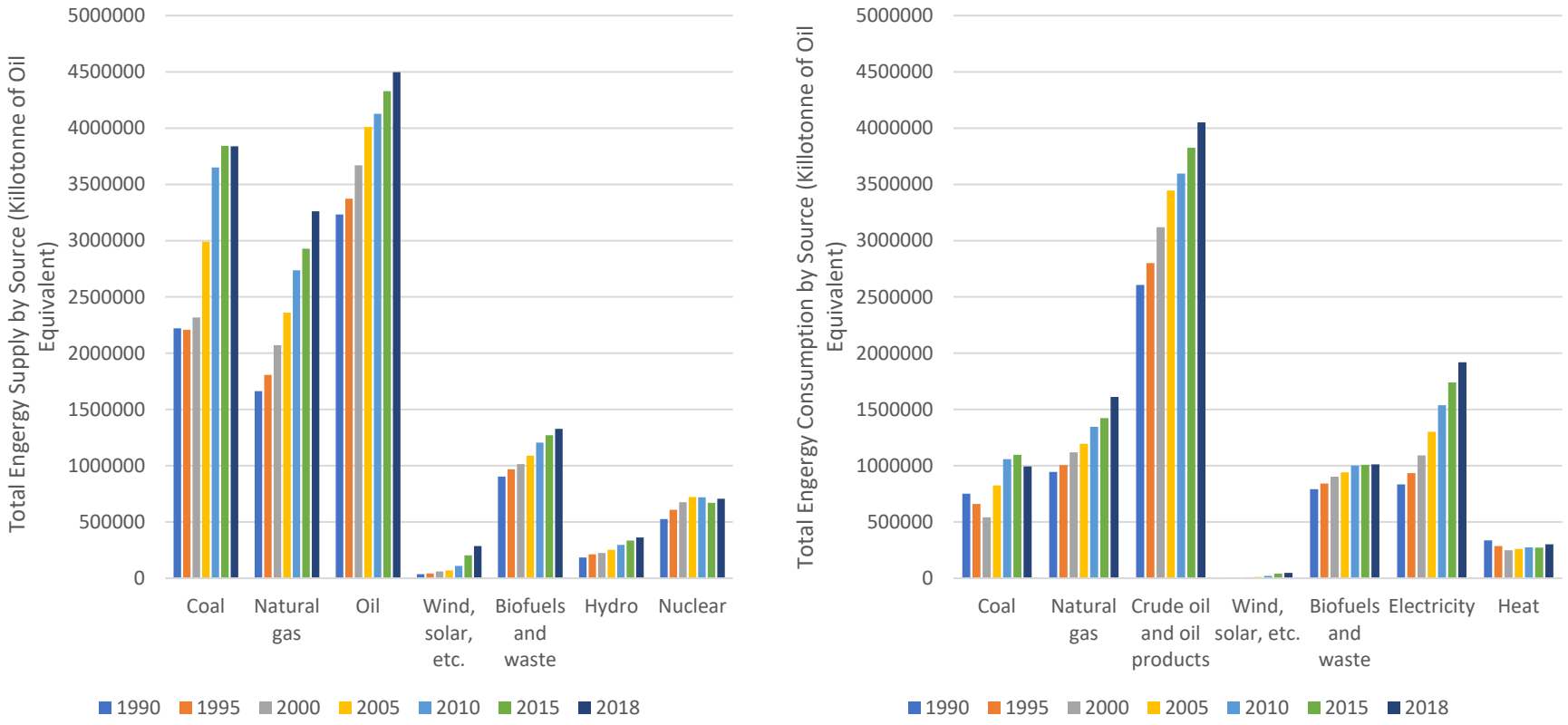

Figure 1-2: The worldwide energy supply (left) and consumption (right) of energy by source showing oil, gas, and coal as the primary sources of energy. Source data are retrieved online from the International Energy Agency (iea.org) report (28 July 2021).

1.2 Digital Rock Analysis: frameworks and characterization methods

DRA methods using X-ray micro-computed tomography (micro-CT) consist of the following steps: (1) image acquisition, (2) image filtering and processing, (3) image segmentation, and (4) image analyses and pore-scale modeling. Each of the following sub-sections will discuss a given step and its limitations.

1.2.1 Raw Micro-CT Image Acquisition

X-ray micro-CT imaging facilitates obtaining a digital representation of rocks in a non-destructive and non-invasive manner [1, 3, 16, 50]. X-ray images were introduced as radiographs (2D projection planes) to study many materials along only one dimension where planar or orthogonal visuals are obtained [51, 52]. The ability of X-ray beams to penetrate a given material at a specific location depends on the initial beam intensity, the investigated material atomic number, and the material density. The local linear attenuation coefficient μ(s) along ray path(s) of a monochromatic X-ray in a radiograph can be described using Beer's law as:

$$I = I_0 e^{-\mu(s)} \qquad (1\text{-}1)$$

where I is the transmitted intensity of the X-ray passing through the object and I_0 is the original incident beam intensity (from the source). Consequently, low-density matter such as air or water will generally allow more X-ray passage than will high-density matter such as minerals. The mid-1970s saw a new technique called Computerized Transverse Axial Tomography [52, 53]. This method enables 3D rock images to be obtained by reconstructing a 3D volume from a set of 2D x-ray projections that are recorded while the sample is rotated at various angles. The reconstruction of a set of 2D images involves

solving mathematical inversion equations [54] for determining μ at each location inside the scanned volume [50]. This allows distinguishing the materials with different densities. For details regarding reconstruction algorithms and implementation, see [54-57].

The imaging setups used to obtain computed tomography have evolved significantly [58]. Most of the modern micro-CT setups use X-ray tubes (laboratory-based micro-CT) [59, 60] or synchrotron-based radiation [61]. Although the synchrotron-based methods provide better spatial resolution and signal-to-noise ratio [62], synchrotron facilities are few and generally have a high operating cost. In contrast, lab-based micro-CT poses a lower X-ray source flux and is often less costly for scientific research [63-65]. Figure 1-3 shows the lab-based helical micro-CT (Mark 1, ThermoFisher) at the Tyree X-ray facilities at the University of New South Wales.

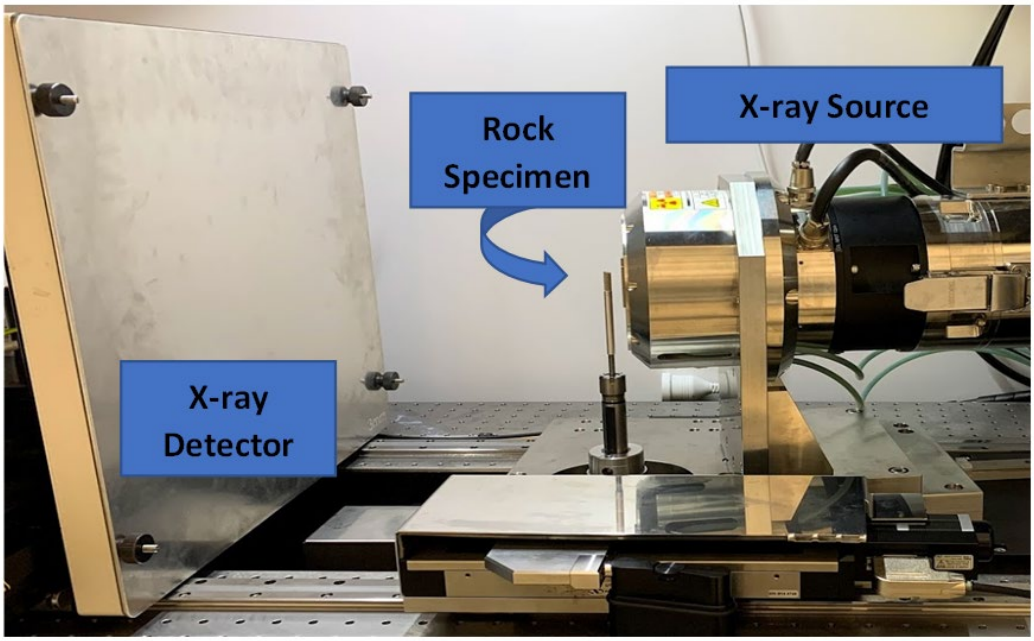

Figure 1-3: The helical micro-CT instrument at the Tyree X-ray facility at the University of New South Wales.

In such a micro-CT setup, the X-ray source and detector are kept stationary. The rock sample is placed on a rotating stage where many radiographic projections (or accumulations) are recorded during imaging. The imaging configuration determines to a high extent the image quality and spatial resolution. The imaging configuration includes the exposure time, number of accumulations, the X-ray source flux, detector specifications, and sample position with respect to the X-ray source and detector.

1.2.2 Raw Image Processing and Artifacts Removal:

After the reconstruction of the 3D image from the radiographs, it is common to digitally manipulate the raw volume to remove artifacts affecting micro-CT imaging. Most X-ray sources in micro-CT scanners generate a polychromatic beam (a beam with a spectrum of X-ray energies and wavelengths), which attenuates low-energy X-rays in a beam, resulting in an apparent high attenuation coefficient at the outer regions of the scanned volume. This is known as beam hardening and is one of the most frequent artifacts in

computed tomography. Beam hardening can be reduced using (1) attenuating filters that block low-energy X-rays, (2) smaller samples, and (3) software-based corrections during reconstruction. Images could also contain ring artifacts, which appear as circles with different voxel intensities emerging from the center of the rotational axis. They are usually caused by miscalibration of X-ray detectors. This can be fixed during scanning by applying high-strength attenuating filters, or digitally using software packages such as Qmango [66], TomoPy [67], and SarePy [68, 69] before or after reconstruction.

Partial volume effect is another common imagine artifact [2]. This artifact happens notably in limited-resolution (i.e. large voxel size) images when an X-ray beam passes through heterogeneous materials an average attenuation coefficient of the materials. This causes blurring of edges (air, grains, and fluids), which hinders subsequent image analysis. Partial volume effects can be noticeable when analyzing rocks with features below typical micro-CT resolution (i.e., microporosity, coal cleats, and hairline micro-fractures), such as carbonates [70-72], coal [73], and shale [74-76] samples. Figure 1-4 shows examples of the three aforementioned artifacts.

Artifacts arising from the imaging procedure or the reconstruction approach are not the only ones that can worsen image quality. Common examples include streak artifacts [77], commonly caused by high-density materials (i.e., minerals), and cone-beam effects [78] caused by the incomplete sampling of the mathematical 3D radon space (the topological space under investigation), which reduces the quality of the tomogram slices far from the center of the cone. Moreover, artifacts can also be associated with secondary radiation [79] and sample movement.

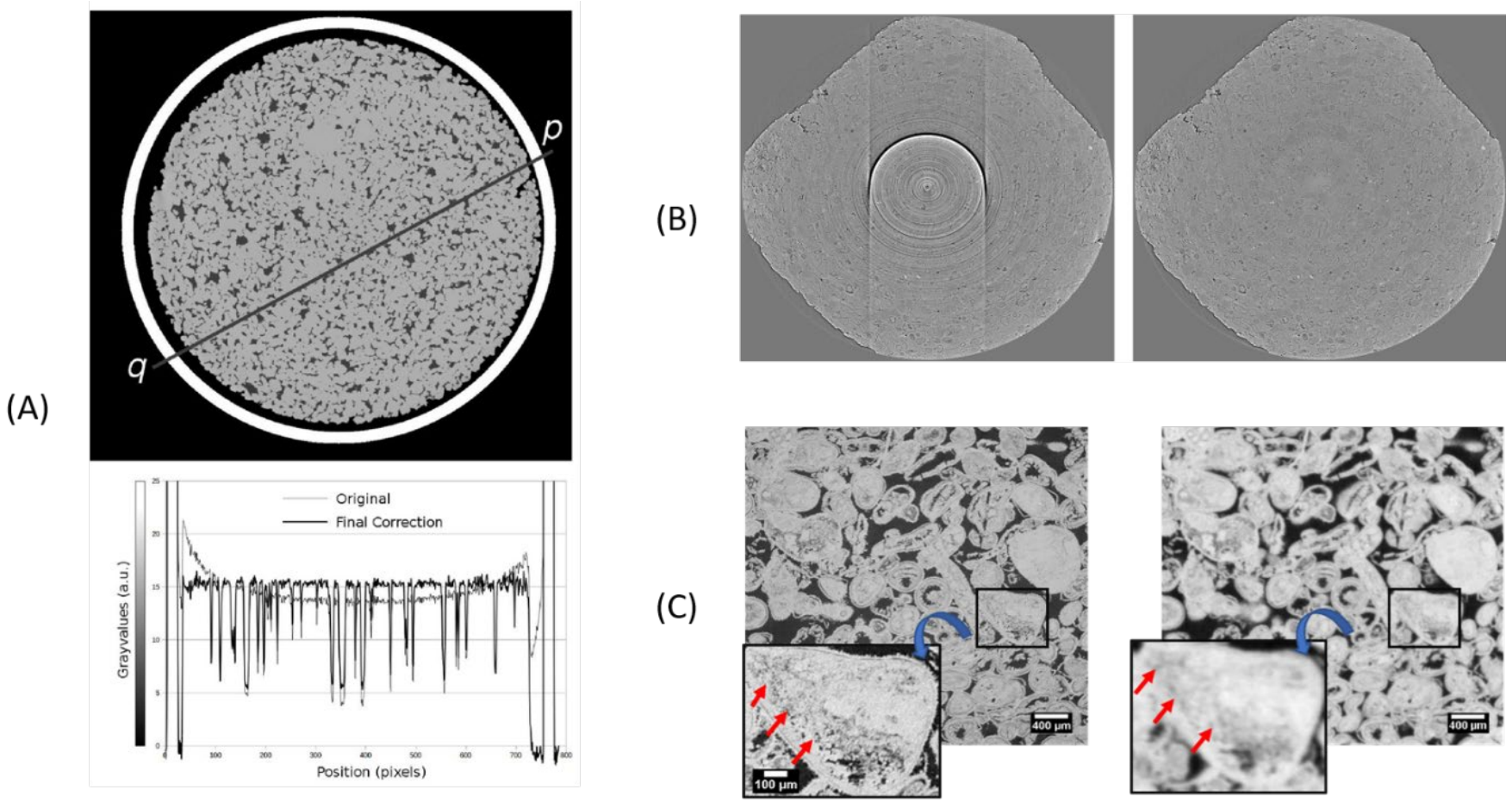

Figure 1-4: A depiction of typical imaging artifacts in micro-CT scanning. (A) Beam hardening, causing a “cupping effect” (upper) where intensity values (lower) are shown before and after correction using the method described in Holt, et al. [80]. (B) Ring artifacts causing concentric circular stripes on a limestone sample (left), and digital ring artifact removal (right) using the algorithm proposed by Vo, et al. [68]. (C) Partial volume effects are illustrated by comparing low-resolution (right) and high-resolution carbonate images (left), which cause blurring of micropores (see red arrows). Illustrations in (A) and (B) are modified after Holt, et al. [80], and SarePy documentation by Vo, et al. [68], respectively.

Although micro-CT provides a detailed representation of the morphology of rock samples, researchers are sometimes interested in more features such as which minerals compose a given section of a sample. Combining data from other techniques with micro-CT scanning can lower the imaging artifacts and enhance the detail and interpretability of images. For example, micro-CT data are frequently merged with scanning electron microscopy methods in order to determine microporosity and minerals [81, 82]. Also, multi-resolution micro-CT scans can be merged together to obtain a more robust analysis on a larger field of view [83].

The last step in raw image processing involves reducing noise effects for improved subsequent segmentation, analyses, and modeling. Noise is inherent in all signal-acquisition processes, including imaging. Noise can be reduced through elongated imaging (exposure time). It is also common to apply image filters to reduce the effect of noise and preserve phase boundary sharpness. Common examples of image filters are Gaussian, mean, non-local mean, and anisotropic diffusion. Louis [84] gave an example (shown in Figure 1-5) of the impact of applying a Gaussian filter, artificial noise, and a non-local mean filter to a micro-CT sandstone image. Figure 1-5 (a) shows a Boise sandstone image that has already been denoised. A Gaussian filter in (b) smooths the grains of the sandstone, at the cost of blurring the edges as if the image were acquired at a lower resolution. In (c), artificial salt and pepper noise is added, rendering histogram-based segmentation or analyses unachievable. Lastly, in (d), noise reduction using a non-local mean filter preserves the smoothness of phases and sharpness of the edges.

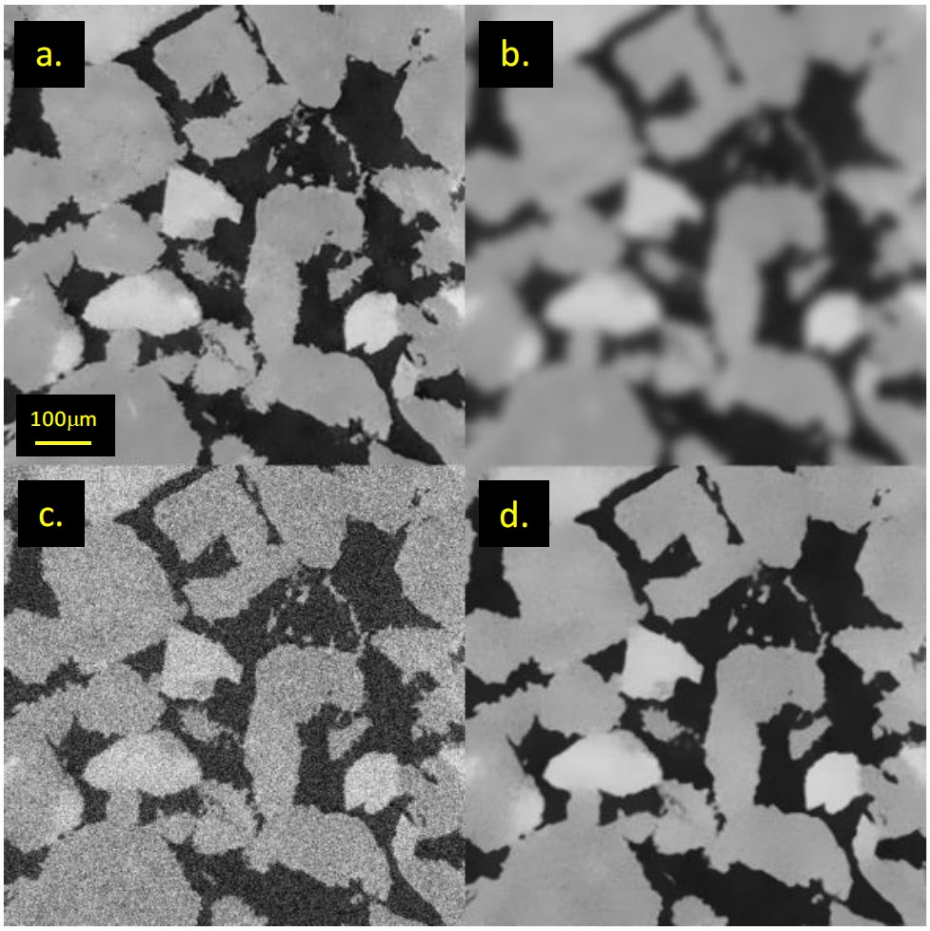

Figure 1-5: Micro-CT image of Boise sandstone. (a) Denoised image. (b) Gaussian filter smoothing, causing blurred edges. (c) The addition of noise, which precludes histogram-based segmentation. (d) The non-local mean filter restores the smoothness and sharpness of the grains. Retrieved from Louis [84].

1.2.3 Image Segmentation

Upon noise removal, segmentation is often applied to label the existing phases such as pore space and minerals of the raw greyscale image under investigation. This facilitates subsequent image analyses ranging from the simple computation of the phases' volume fractions (including porosity and fluid saturations), to modeling complicated flow and transport mechanisms. Hence, segmentation is indispensable to the DRA framework.

Segmentation in digital rocks often aims to identify the pore space for estimating porosity and modeling unreactive single-phase flow. For this purpose, it suffices to

segment images into two phases: (1) pore space and (2) solid phase containing all minerals. For more advanced simulation studies including modeling reactive flow [85] and mixed wetting flow [86], multi-label segmentation may be required if fluids or minerals need to be identified. Numerous segmentation approaches in DRA have been reviewed [3, 87], and the following discussion will highlight the most frequently reported methods only. Segmentation methods can be classified based on the methodology: (1) histogram-based thresholding algorithms, (2) locally adaptive algorithms, and (3) ML-based methods. Global thresholding approaches are based on selecting an optimum grey-level intensity threshold(s) based on the histogram of the image, to make a binary or multi-label mask. The selection of threshold can be made automatically using Otsu [88] and K-means [89, 90] or manually by user input. One major drawback of global thresholding is its sensitivity to imaging artifacts such as cupping, partial volume effects, and noise [87, 91].

Locally adaptive methods are often designed to handle noise and other degrading imaging effects. This is achieved by incorporating image features such as greyscale intensity gradients and local spatial covariance [87]. Frequently used locally adaptive methods in DRA are indicator kriging [72, 92], watershed transform [93], hysteresis [94], and converging active contour (CAC) [66]. Most of these methods require the user to determine initial seeds or a range of greyscale intensities for each phase. The algorithm thereafter populates the untagged voxels with the appropriate phase/label based on a predefined policy or set of instructions. Kriging methods assume a local spatial correlation between the phases in rock images by creating an indicator variable from two hysteresis thresholds (often initially defined by the user). Then, a model semi-

variogram can be initialized from the local empirical indicator data. Ordinary kriging (a system of constrained linear equations) is used to assign a local membership or class globally through a moving kernel that's based on the semi-variogram model. Ordinary kriging equations are solved so as to minimize variance estimate of class membership probability. The voxels are labeled with the highest membership probability. Further details on geostatistical image segmentation can be found in [95, 96]. Other suggested hysteresis methods [94] involve choosing multiple thresholds to define "definite" solid or void intensity ranges. The void and solid voxel greyscale intensity distributions can be regarded as Gaussian mixtures and hence estimated using Expectation Minimization methods [97].

Watershed is a region-based method in which an image is "flooded" to create basins or (catchments) according to the topography of greyscale intensity values. Troughs are filled, commencing with local minima. At a certain stage, as the level rises, the basis or catchments would meet forming dams or "watersheds." The landscape would be then comprised of basins separated by the watersheds. Predefined thresholds would be required to set endpoints or limits for the flooding procedure specific to each phase in the image. Voxels setting on the catchments' lines are then assigned a label based on the mathematical mode of the local neighborhood [98]. Watershed has been utilized in many digital rock analyses [23, 25, 99]. CAC [66] relies on combining the watershed transform and active contours [100] to classify voxels. Again, seeds or thresholds have to be predefined by the user. This algorithm overcomes a known disadvantage with watersheds, in which the boundaries of catchments are traversed by a given class simultaneously while the catchments grow. The main drawback of CAC is its

computational cost even when utilizing a fast marching cube algorithm to advance the boundaries [98]. CAC has been utilized for many DRA studies such as porosity estimation [101], reactive transport flow modeling [102], and contact angle measurements [103].

ML-based segmentation methods can be categorized as supervised or unsupervised [104]. In supervised methods, the algorithm uses a set of segmented instances to learn how to classify voxels and identify phases, where the input and output are given and labeled. In unsupervised methods, only the input is given and the algorithm must classify the voxels. Common examples of unsupervised segmentation approaches are K-means, Fuzzy C-mean, and Self-Organizing Maps [105, 106]. Because these methods require the user to set up the clustering and classification parameters, they do not entirely eliminate user bias. Further reading about unsupervised methods can be found in [22, 104, 107].

Supervised ML segmentation approaches map raw greyscale images to labeled images by learning a classification function. The aim afterward is to accurately segment unseen data using the learned function [108]. The many variants of supervised ML algorithms that can be used for digital rock segmentation include support vector machines [109-111], decision trees [112], and neural networks [23, 106, 113]. Neural networks (NNs), which are the core building block of modern DL algorithms, can extract hierarchal features automatically from input to learn the segmentation function. NN segmentation is among the most promising learning methods and has been widely applied to more complex tasks such as medical image segmentation [114] and autonomous driving [115].

1.2.4 Image Analyses and Pore-scale Modeling

Upon obtaining segmented images, a variety of morphological measurements can be estimated directly from the pore, fluid (if present), and mineral phases. These

measurements can be either geometrical or topological. Geometrical measurements inferred directly from the existing phases include volume fractions (i.e., porosity and fluid saturation) [81, 116, 117], surface area [118], shape factors [119], and fluid contact angle [120]. Topological measurements are concerned with the connectivity of the phases and include estimating Euler characteristic [117], coordination number, and tortuosity of flow paths [121-123]. In addition to characteristics obtained via image analyses, numerical methods can be applied for modeling/estimating solute transport [124, 125], formation factor [16], single-phase flow [48, 126, 127], reactive transport [128, 129], plasticity and geomechanics [130, 131], and multi-phase flow [132, 133]. Such measurements are of great value for a wide range of applications involving flow in porous media, including ground-water transport [116], oil and gas recovery [116], CO_2 capture and storage [13], and battery manufacturing [134, 135].

Traditionally, modeling single-phase flow in pore space can be achieved through a variety of approaches depending on the level of detail and accuracy required. Pore space geometry can be significantly simplified by extracting a pore network that captures the connectivity of pore space but uses spheres to represent pore bodies and sticks to represent pore throats. Such idealized geometries reduce the computational cost associated with estimating velocity and pressure fields. Pore networks are typically sufficient for estimating the absolute permeability and assessing connectivity. Algorithms for pore network extraction include maximal ball [136-138], medial axis [139], and watershed-based extraction [140-142]. One drawback of such methods is the ambiguity of the criteria of distinguishing pore bodies from pore throats [137]. This

occasionally creates disagreement in the computation of topological and flow characteristics [143].

More accurate results can be obtained from direct numerical simulation (DNS) on the pore space. A common DNS framework solves a suite of conservation of mass and momentum equations, often referred to as the Navier-Stokes equations [144]. Approaches to solving such equations include Lattice Boltzmann Methods and Finite Methods [145, 146]. The downside of these techniques is that they require exhaustive computation capabilities because the solution involves solving non-linear partial differential equations, often iteratively [49, 145-148]. Laplacian-based geometrical equations for approximating the conductivity of pore voxels have been suggested to reduce computation requirements in pore-scale simulation [149, 150]. This method estimates conductivity through geometric approximation and can be solved using Finite Methods. However, these methods still require agglomeration and domain decomposition techniques for estimating single-phase flow on 3D images larger than $1{,}000^3$ voxels [49, 151].

For multi-phase flow, pore networks and direct numerical methods have been applied to probe displacement mechanisms and relative permeability [1, 132, 148]. Pore network models apply theoretical and analytical principles of immiscible and capillary-dominated displacement on the extracted networks [152, 153]. However, the capability of such methods is limited in matching experimental data or capturing accurate physics of displacement such as representing wettability [154]. For example, the idealized geometries used to construct networks (triangles, circles, star-shape, etc.) do not capture the surface roughness of the pore space, which is a major factor in wetting

mechanisms [154, 155]. DNS such as Level Set [156-158], Volume of Fluid [159, 160], and Lattice Boltzmann Methods [132, 147, 161] have been extensively applied for modeling for computing relative permeability. However, these methods are often applied to simulate displacement on images no larger than 600^3 voxels [156, 161].

The advances in micro-CT imaging enable capturing fine details of pore space geometry at a resolution of a few micrometers and image sizes of more than 2000^3 voxels [49, 162]. Such images can capture representative elementary volumes of many conventional rock samples [48, 163]. However, applying full-scale multi-phase flow simulation on such large volumes is memory-demanding and would require supercomputing. This issue is further discussed in the following section.

1.3 Challenges in Digital Rock Analysis

DRA is a powerful tool to characterize porous media. However, because DRA is sequential, bottlenecks and inaccuracies in the imaging, processing, and modeling pipelines can have profound effects downstream. For example, imaging artifacts may cause blurring to grain boundaries and small features (i.e., micropores and microfractures), leading to incorrect segmentation. This can lead to a loss of connectivity and inaccurate flow and transport modeling. The following are some of the most influential bottlenecks and error sources in DRA.

- **User Bias**. The user's selection of the parameters involved in image processing and modeling affects the results obtained from DRA. Segmentation is arguably one of the most critical steps in DRA that typically require user input [87]. Manual choice of thresholds and initial seeds of greyscale values are often required to complete segmentation [98]. Therefore, the outcome can vary greatly based on user

selections. Many studies investigated the effect of segmentation on the computed rock properties [34, 87, 164-168]. Leu, et al. [168] used a synchrotron-based micro-CT to image a Berea sandstone and evaluated the effects of multiple segmentation techniques on porosity, permeability, and capillary pressure. They showed that the choice segmentation method can cause discrepancies and miscalculation of capillary pressure curves, flow path geometries, and permeability.

- **Field of View and Resolution Tradeoff**. The spatial range at which DRA operates is constrained by the imaging resolution and the field of view. Intuitively, imaging larger rock volumes increases the possibility of capturing a representative elementary volume (REV). Nevertheless, this can be achieved with a lower resolution, which is sometimes necessary to remain within the limits of micro-CT detectors. REV is the smallest volume that captures the heterogeneity of a porous medium without significant variations in the measured macroscopic properties. REV is an important concept in DRA to obtain accurate and size-independent flow simulations that are insensitive to modeling effects (e.g., boundary conditions) [169]. Typical core plugs for CCA and SCAL analyses have a 1:2 ratio of diameter to length. The diameter of these core plugs is often 1 inch or 1.5 inches. A 1-inch core plug can be covered in a micro-CT scan, but this requires low resolution (i.e., >25 micrometer/voxel) with a micro-CT detector producing radiographs of size 2048×2048 pixels. This fails to resolve some of the pore space that would affect modeling flow, for example, in conventional rocks. This can be avoided if the REV were determined to be small enough to permit imaging under the highest attainable resolution. Many efforts have been devoted to obtaining REVs of different materials

or REV based on a specific physical property (i.e., porosity or permeability) [48, 170, 171].

For determining the optimal tradeoff between the field of view and resolution, Saxena, et al. [169] calculated the coefficient of variation (a statistical measure) in the permeability and the porosity of sandstone volumes of various sizes and resolutions. Their results showed that at least 10 voxels are needed for resolving pore throats to obtain reliable single-phase flow simulation. if this condition is not met, the main author suggested correcting the simulation results using a correlation based on Mercury Intrusion Capillary Pressure (MICP) experiments [172].

The tradeoff becomes more constrained in more complex porous media. For example, carbonates contain microporosity below typical imaging resolution, and larger volumes need to be considered when computing REVs of physical properties [72, 81, 173].

- **Computational Cost**. The computational cost associated with DRA is proportional to the size of the image domain under investigation. While this applies to all steps in DRA, it is more apparent in modeling flow and transport than in other steps [48]. Micro-CT scanners can produce images containing more than one billion voxels. Processors in consumer-grade workstations cannot handle the level of detail provided by imaging techniques to model flow directly on pore space [1]. For example, solving Stokes flow in porous media to determine the permeability from an image 700^3 voxels in size would require a central processing unit (CPU) time exceeding 10 days using a conventional workstation [48]. Also, Yang, et al. [174] compared algorithms for simulating flow and solute transport on a cylindrical sphere pack model having dimensions 8.8 mm × 16 mm and imaged at 20 micrometer/voxel

resolution. They showed that the CPU time of Lattice Boltzmann and Finite Volume methods range from 9 hours to 61 hours. This limitation is also controlled by the method of choice to carry on the simulation [150]. On typical workstations, single-phase permeability can be computed using the Lattice Boltzmann Method or Finite Methods for volumes less than 500^3 voxels. Other simplified methods such as pore network models and Laplace solvers can handle larger volumes, typically up to 1000^3 voxels [150]. Multi-phase flow simulations and relative permeability computations for such images are often executed on supercomputers [175]. Therefore, applying numerical methods to estimate flow and transport on large images >1000^3 voxels can be relatively considered expensive. This ultimately hinders the full exploitation of DRA as a technology for formation evaluation.

1.4 Deep Learning

The last few years have seen a notable transformation in ML and data science, embodied by major advancements in deep learning (DL). Computational capacity has increased sufficiently to solve many complex learning tasks that had been unapproachable, such as computer vision [176], mastering the games of Go and chess [177, 178], and predicting protein folding [179]. The algorithms used in today's most advanced DL models can be regarded as a progression to the perceptron model proposed in 1958 by Rosenblatt [180]. In this model, a *perceptron*, which is a machine algorithm, was used for pattern recognition. This algorithm had a single-layer perceptron with a step activation function. Later, multilayer perceptron (MLP) [181] and backpropagation methods [182] were introduced to form a basic learning scheme of NNs [183, 184]. The ability of NNs was greatly enhanced by the introduction of convolution on 2D signals

(i.e., images) [185, 186]. Convolutional neural networks (CNNs) incorporate the extraction of low-level local features, weight sharing (reducing the number of free parameters), and backpropagation for visual pattern recognition [185]. Advances in computer hardware, including the introduction of Graphics Processing Units (GPU), facilitated training deeper CNNs, achieving a breakthrough in challenging object recognition datasets in 2012 [176]. These datasets contained a large number of similar objects classes that were hard to classify using computer algorithms. Since then, major technology companies including Facebook, Google, Tesla, and Microsoft founded dedicated research teams for DL research. Lately, DL techniques have been applied to various representations of data and multi-dimensional images such as 3D grids (e.g., voxel images), graphs, and geodesics [187, 188]. A timeline summarizing the major technological advancements in ML and DL is shown in Figure 1-6.

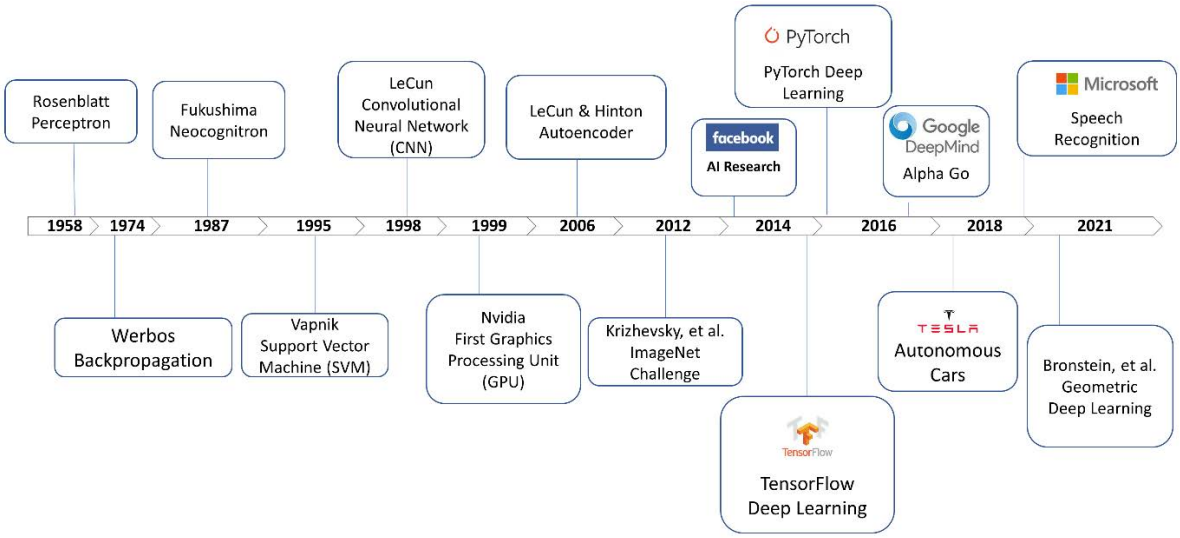

Figure 1-6: The evolution of machine learning, with a focus on deep learning.

Interestingly, the foundations of DL algorithms build upon two simple ideas. First, the concept of “representation learning,” in which hierarchical and distinguishing features

capture the regularity or essence of performing a specific task [189]. Learning the representation through feature extraction unravels the explanatory factors of variations behind data patterns. Research on visual patterns showed many benefits in combining local low-level features (i.e., edges) with higher ones (entire objects). DL methods apply this concept automatically by learning to combine features through receptive fields (convolutional kernels) [185]. Second, learning by incorporating efficient optimization methods (e.g., gradient descent methods), often implemented using backpropagation [182, 183, 186, 187]. The mathematical principles of these two principles are discussed in [28].

Artificial Neural Networks (ANNs), Convolutional Neural Networks (CNNs), Recurrent Networks (RNNs), and Generative Adversarial Networks (GANs) are commonly used architectures for DL. ANNs are often used to handle basic classification and regression problems of 1D input signals, which are often represented using a vector of discrete values. ANNs consist of input layers, hidden layers, and output layers. Each of these layers is connected as shown in Figure 1-7: A simple Artificial Neural Network (ANN) architecture. The input layer processes a vector of discrete values by passing the signal from the nodes ("neurons") of each layer to the subsequent "hidden" layer(s). At each layer (l), a number (N) of inputs (x) is assigned a trainable weight (W) and bias (b). The output is activated through a nonlinear activation function (e.g., sigmoid operator) and passed to the next layer, where the same mathematical operations are repeated. The error for the network output is computed and backpropagated to update the trainable weights. ANNs can be used as universal approximators and for correlating parameters.

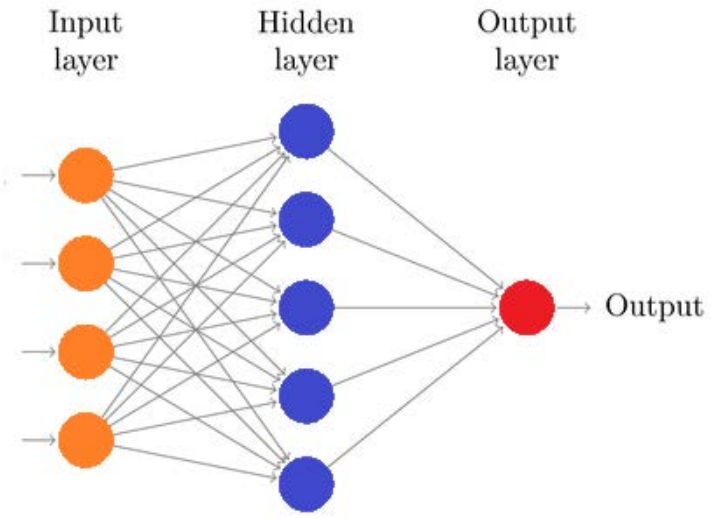

Figure 1-7: A simple Artificial Neural Network (ANN) architecture. The input layer processes a vector of discrete values by passing the signal from the nodes ("neurons") of each layer to the subsequent "hidden" layer(s).

CNNs process 2D or 3D images by applying convolutional operators called "filters" that learn a weighted sum for extracting features from the images. These filters are tuned automatically throughout the training process to optimize feature extraction. A detailed discussion on CNN components and their mathematical implementation is provided in section 3.3.3 of this thesis. RNNs [190, 191] constitute a set of networks for processing sequential data corresponding to different positions or times. Most of the applications of RNNs are well-suited to language processing and time-related problems [192, 193]. Generative Adversarial Networks [194] consist of two networks: a generator and a discriminator. The generator conditions the input signal to generate realistic images as much as possible, while the discriminator penalizes the generator for images poorly conditioned or for fake-looking images. GANs can be utilized for applications such as segmentation, denoising, and generating 2D and 3D images [195, 196].

1.4.1 Deep Learning in Digital Rock Analysis

The technological capabilities of DRA have greatly increased through the incorporation of ML methods [20, 21]. Improvement in GPU computations, DL methods, and optimization techniques made working with big data like micro-CT images feasible. In the last five years, DL has been utilized in many digital rock applications such as binary/multimineral segmentation [23, 25, 113, 197], image enhancement and interpolation with super-resolution networks [198-202], image generation [203-205], petrophysical properties regression [26, 206-208], and flow field modeling [209-211]. For a broader review of the literature on DL in pore-scale imaging and modeling, Wang, et al. [20] discussed many aspects related to DL applications in DRA, including common network architectures used, applications, and limitations. In addition, examples of related work are mentioned in the introduction of each chapter in this thesis. Chapter 2 discusses the work published on image super-resolution and segmentation. Chapters 3 and 4 present the effort directed toward predictive modeling of physical properties using DL.

1.5 Thesis Objectives and Outline

The main objective of this thesis is to develop, validate, and integrate DL capabilities that aid the development and design of more accurate and reliable DRA frameworks. This includes mitigating existing limitations (see section 1.3) in imaging hardware, processing, and modeling schemes. The automation offered by DL tackles these limitations and offers efficient alternatives that can be summarized as follows:

Eliminating methodological and human interference inaccuracies. Previous studies have shown that some filtering, segmentation, and modeling algorithms in DRA have

associated methodological inaccuracies. Some practices/approaches help to gain reliable DRA results while requiring little if any additional computational resources. This avoids the user bias and experience that can lead to discrepancies in results obtained from DRA. This thesis applies DL algorithms that can learn from the best practices automatically and hence eliminate the need for user judgment or the risk of applying inaccurate methods.

Alleviating the need for intensive computation. Estimating the physical properties of digital rocks often involves applying multiple algorithms that sometimes can be computationally intensive, for example, simulating flow directly on rock images for obtaining permeability. An alternative approach based on CNNs regression is proposed. The framework can learn the geometry of pore space and predict multiple physical properties in one feed-forward CNN inference rather than using iterative numerical solutions. The rapid predictive modeling capabilities offered by DL are showcased in this thesis.

Expanding capabilities that cannot be achieved using imaging hardware. The heterogeneity of some porous media, especially those with complex structures and pore size distribution, require fine-detail imaging for reliable modeling. This makes the tradeoff between resolution and domain representation more critical. DL can reliably translate large domains of low-resolution images to high-resolution through super-resolution. Novel DL techniques for super-resolving and segmenting complex carbonate images are presented for this purpose.

As such, this thesis answers four key questions linked to the previous points:

I. **Is it possible to develop end-to-end DL schemes that can minimize user bias and process low-resolution images to reliably produce high-quality segmented data? If so, how is this improvement reflected in the computed physical properties of the processed medium?**

II. **Can CNNs be used as regression tools for predicting the physical properties of porous media directly from 2D segmented micro-CT images? Can raw greyscale images be used?**

III. **What accuracy margins are expected when applying 3D residual network architectures for estimating permeability directly from volumetric images of sandstones and carbonates rocks?**

IV. **Can pore space representation or network architecture improve DL models' performance and regression accuracy?**

The thesis is structured to integrate DL in several DRA focus areas. These focus areas are (1) image processing, (2) image analysis, and (3) pore-scale modeling. To highlight this further, a flowchart is presented in showing the DRA areas targeted, where DL capabilities are harnessed for obtaining a better DRA.

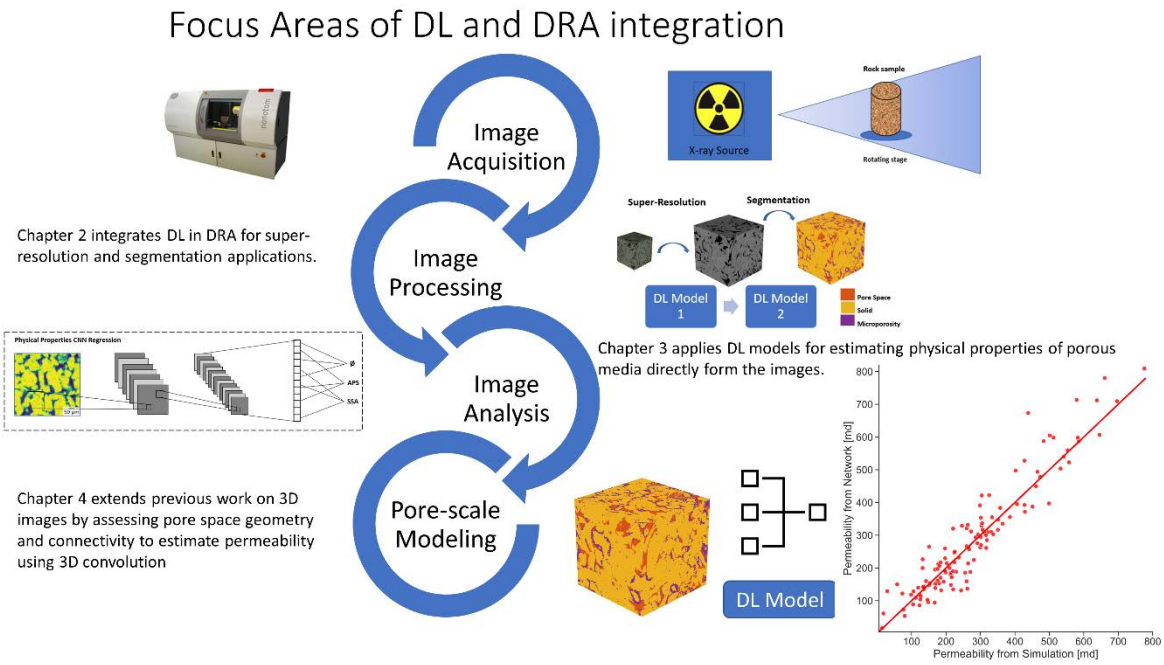

Figure 1-8: Focus areas in DRA workflow for DL integration

The remaining thesis chapters are organized as follows:

Chapter 2, titled "Super-Resolved Segmentation of X-ray Images of Carbonate Rocks using Deep Learning," a paper under review at the journal *Transport in Porous Media*, is designed to answer the first question stated above. In this chapter, DL frameworks are created for obtaining a super-resolved segmentation of two complex carbonate rocks. These CNN-based frameworks are developed with the objective of identifying macropores, micropores, and solid phases from low-resolution images. A dataset comprised of low- and high-resolution 3D micro-CT images of the carbonates are prepared. Two training frameworks are implemented for training, where the super-resolved segmentation is obtained in an end-to-end scheme and using two networks (super-resolution and segmentation) separately. The network segmentation accuracy is assessed by comparing various voxel-wise metrics, topological properties, and flow characteristics with those of other segmentation methods.

Chapter 3, titled “Machine Learning for Predicting Properties of Porous Media from 2D X-ray Images” and published in the *Journal of Petroleum Science and Engineering,* addresses the second question and implements CNNs as rapid predictive modeling tools using 2D X-ray rock images. The proposed frameworks estimate the porosity, specific area, and average pore size using binary or greyscale sandstone images as input. A dataset consisting of more than 5,000 images of three sandstones is prepared for training. The absolute and relative errors of the network regression on testing images are quantified for each physical property. Error analysis and training wall-time are further discussed.

Chapter 4, titled “Flow-Based Characterization of Digital Rock Images Using Deep Learning” and published in the *Society of Petroleum Engineers Journal*, builds upon the work presented in Chapter 3. This chapter answers the third and fourth questions. Residual Networks (ResNet and ResNext), which are advanced CNN architectures, are applied to characterize digital rock images. The intrinsic permeabilities of the 3D subvolumes of multiple sandstones and carbonates (<29,000 subvolumes) are computed using a numerical solver. Then, ResNet and ResNext are trained to predict the continuous values of permeability using the 3D subvolumes as input. The effects of network depth and pore space geometry representation (the use of binary images versus conductivity maps) on the regression accuracy are discussed. The models were tested against unseen data, where explained variance score, absolute error, and relative error were quantified. This chapter highlights the scalability, automation, and potential of DL methods in the predictive modeling of geometry-dependent properties.

Lastly, Chapter 5 summarizes the main findings and recommends directions for future work.

2 Super-Resolved Segmentation of X-ray Images of Carbonate Rocks using Deep Learning

Naif J. Alqahtani[A], Yufu Niu[A], Ying Da Wang[A], Traiwit Chung[A], Zakhar Lanetc[A], Aleksandr Zhuravljov[B], Ryan T. Armstrong[A] & Peyman Mostaghimi[A]

A School of Minerals and Energy Resources Engineering, The University of New South Wales, Sydney, Australia

B Institute of Environmental and Agricultural Biology, University of Tyumen, Tyumen, Russia

The content of this chapter is a research paper titled "Super-Resolved Segmentation of X-ray Images of Carbonate Rocks using Deep Learning" under review in Transport in Porous Media (2021). This chapter addresses the first research question of the thesis: Is it possible to develop end-to-end DL schemes that can minimize user bias and process low-resolution images to reliably produce high-quality segmented data? If so, how is this improvement reflected in the computed physical properties of the processed medium?

To address these questions, the chapter introduces DL techniques that adopt CNN autoencoders to obtain super-resolved segmentation of complex carbonate rocks. This requires the user only to input the image once the model is accurately trained. This chapter demonstrates the capability of DL techniques to 1) eliminate user bias inaccuracies and 2) rectify the imaging hardware rigid constraints using super-resolution. These limitations are two outstanding challenges in the current Digital Rock Analysis (DRA).

Abstract

Reliable quantitative analysis of digital rock images requires precise segmentation and identification of the macroporosity, microporosity (sub-resolution porosity), and solid\mineral phases. This is highly emphasized in heterogeneous rocks with complex pore size distributions such as carbonates. Multi-label segmentation of Carbonates using classic segmentation methods such as multi-thresholding are highly sensitive to user bias and often fail in identifying low-contrast sub-resolution porosity. In recent years, DL has introduced efficient and automated algorithms that are capable of handling hard tasks with precision comparable to human performance, with application to digital rocks super-resolution and segmentation emerging. Here, we present a framework for using Convolutional Neural Networks (CNNs) to produce super-resolved segmentations of Carbonates rock images for the objective of identifying sub-resolution porosity. The volumes used for training and testing are based on two different Carbonates rocks imaged in-house at low and high resolutions. We experiment with various implementations of CNNs architectures where super-resolved segmentation is obtained in an end-to-end scheme and using two networks (super-resolution and segmentation) separately. We show the capability of the trained model of producing accurate segmentation by comparing multiple voxel-wise segmentation accuracy metrics, topological features, and measuring effective properties. The results underline the value of integrating DL frameworks in DRA.

Keywords: Carbonate rocks, Segmentation, Microporosity, Super-resolution, Deep Learning, Digital rock

2.1 Introduction

Digital Rock Analysis (DRA) has emerged as one of the superior technologies for studying porous media at the pore-scale [1-4, 212]. DRA integrates high-resolution X-ray microtomographic imaging (micro-CT) with advanced computational methods for predicting geomaterial effective properties [48, 126, 132]. DRA complements classic and slower laboratory investigations, namely Conventional Core Analysis (CCA) and Special Core Analysis (SCAL), through fast and reproducible modeling frameworks [46, 213]. A standard 'image and model' framework usually consists of multiple steps including image segmentation. Image segmentation is paramount for accurate pore-scale modeling [66, 87]. Segmentation techniques commonly reported in the literature for DRA are global and adaptive thresholding [165, 214], watershed algorithms [25, 166], and converging active contours [66]. Thorough reviews of segmentation methods have been presented and compared for DRA in the literature [87, 98, 214]. However, the downside of all these methods is that they require a certain level of user judgment and tuning. As a result, the segmentation outcome is highly susceptible to user bias and experience [25].

Carbonate rocks host more than half of the world's oil and gas reserves [215]. Carbonates often exhibit complex multimodal pore systems with sizes ranging from the nanoscale to the meter scale (cave systems scale)[216]. As a result, the characterization of such geomaterials is often challenging using micro-CT imaging, as the typical imaging resolution is often in the order of few micrometers [1].

The term microporosity is often used in the literature to describe smaller pore structures in porous media. For example, the International Union of Pure and Applied Chemistry

(IUPAC) defines a micropore as a pore with a width not exceeding 2 nanometers. Choquette and Pray [217] defined a micropore in carbonate rocks as a pore smaller than 62.5 micrometers in diameter. While Pittman [218] described micropores as pores less than one micrometer in diameter. In recent micro-CT studies, the fraction of the pore space with structures smaller than the voxel size is termed microporosity or sub-resolution [128, 162, 219]. For this study, the latter definition is used to define pores less than voxel size or pores smaller than 2.68 micrometers in size. Microporosity identification is important for flow and reactive transport modeling in porous media. The identification of sub-resolution porosity using dry images is subjective to the image quality in terms of the degree of noise and instrument resolution besides the segmentation algorithm used [162]. Alternative non-invasive methods include combining micro-CT imaging with two-dimensional Scanning Electron Microscopy (SEM) [220, 221], and Differential Imaging [219, 222-224]. While SEM images provide unprecedented details of the pore geometry, the framework is time-consuming and the nature of two-dimensional analysis introduces high uncertainty, especially when it comes to the three-dimensional connectivity\continuity of the phases. Differential imaging frameworks involve taking X-ray scans of dry and contrast agent- saturated samples to identify microporosity. The process is perhaps one of the best options to resolve sub-resolution experimentally, boosting the contrast between the phases and making the segmentation task less prone to error. However, the method does not entirely remove inherited user bias in the segmentation method of choice and requires time-consuming sample flooding with a contrast agent, image registration and processing.

DL frameworks using Convolutional Neural Networks (CNNs) introduced fast and robust methods for automated image processing [225, 226]. If trained properly, these networks eliminate the user bias and achieve expert-level annotations\processing [25]. The interest in integrating DL in DRA frameworks is evident in recent years [20] with application to lithology classification [227], image denoising [201, 228], binary and multi-phase segmentation [23, 113, 197], super-resolution [198, 199, 229], and predictive modeling of rock properties [26, 99, 207, 208, 210]. Thorough reviews have been published showing the diverse applications of DL in geoscience and DRA [20, 21]. For segmentation problems in DRA, DL frameworks can be used to produce binary and multi-mineral segmentation according to the modeling problem. Binary segmentation is suitable for easier problems such as single-phase non-reactive flow [197, 230], while multi-minerals segmentation is used for more detailed simulations such as reactive transport [85]. In general, DL showed promising results compared to classic methods such as thresholding. Niu, et al. [25] investigated the use of LeNet-5, a CNN architecture, for segmenting 2D images of North Sea Sandstone. The results showed that CNN segmentation outperformed the classic Otsu thresholding and watershed method by comparing their physical properties. Karimpouli and Tahmasebi [23] experimented the use of SegNet architecture to produce a multi-mineral segmentation of a limited number of Berea sandstone images augmented through stochastic reconstruction. The average reported pixel-wise categorical accuracy for the best model is %96. For super-resolution, [199] experimented the use of different super-resolution network variants for obtaining high-resolution 2D images. The study shows the superiority of the performance of networks to classic methods, such as bicubic interpolation, with a 50-70% reduction in relative error. Other efforts by [198, 200] applied a similar scheme using 3D images for

training to obtain super-resolved volumes. The results show a better refinement of edge sharpness and reduction of noise compared to other classic interpolation methods. Kamrava, et al. [229] used a hybrid method of stochastic and DL algorithms to generate super-resolved images of shale formations. The stochastic reconstruction algorithm is used as an augmentation method for generating many image realizations that can be used for training. The results show the superiority of the trained network when the porosity and other metrics are used for comparison with other methods. Janssens, et al. [231] used real multi-resolution carbonate paired images to obtain more accurate segmentation that can be used as ground truth (GT) training data. However, the high-resolution data is not used as-is but downsampled using voxel averaging to obtain a grid size of similar dimensions to low-resolution data. The results of the study reveal improvements when computing several physical properties of the medium. All the previous efforts directed towards super-resolution have used interpolation methods (such as bicubic interpolation) to generate synthetic images pairs as a training dataset. This might not be ideal for practical applications because synthetically downsampled images do not possess the same features of real low-resolution images in terms of noise and partial volume effects. Several efforts have been directed towards reducing this limitation such as the use of unpaired data for training [228, 232]. In this work, multi-resolution scans have been used as-is, where the data has only been cropped and segmented to reveal the true interpolation\translation improvement offered by DL.

Herein, we propose a framework for using CNNs to generate a super-resolved segmentation of carbonates for better identifying sub-resolution porosity. We use a set of multi-resolution micro-CT scans to create a unique high (HR) and low-resolution (LR)

dataset. While acquiring multi-resolution images is common in super-resolution methods, the presented approach alleviates the known trade-off between the field of view and spatial resolution. LR images capture a large field of view while HR images show more details and smaller features (i.e., identifying microporosity). By referring to the term 'super-resolved', we describe the process of translating 'real' LR micro-CT domains to greyscale or segmented HR domains using CNNs. The settings of imaging spatial resolution are designed carefully to resolve sub-resolution in the samples considered as much as possible based on the laboratory experiment. We utilize high-resolution region of interest scanning to fully facilitate easy identification of sub-resolution porosity in the HR imaging characterized by a distinguishable range of intensity values. The LR spatial resolution resolves microporosity poorly, showing partial volume effects. The HR images are segmented and utilized as GT for the CNN training. The gray LR and the segmented HR images are utilized for different DL experiments where the main target is to identify sub-resolution porosity accurately using the LR as an input. We compare the segmentation accuracy using three metrics: voxelwise accuracy, geometry-based metrics, and the physical flow characteristics. This framework can be utilized to optimize current frameworks where the only requirement is to obtain a high-resolution region of interest and train the CNNs to interpolate the segmentation to a bigger field of view using the LR images.

2.2 Materials and Methods

2.2.1 Materials Description

Two carbonate Images shown in Figure 2-1 were considered for training the CNNs. The first one is Indiana Limestone (ILS) which originates from the Salem formation near Bedford, Indiana, USA. ILS is mainly monomineralic rock with 98.8% calcite with the rare

occurrences of quartz (<1%) and clay minerals (<1%). The main solid phases seen in ILS are Allochems, detrital skeletal of marine organisms (i.e., organic detritus), and authigenic calcite cement. Different types of porosities can be distinguished clearly in the HR micro-CT images including macroporosity (resolved and connected porosity between particles\grains), microporosity on the outer shells of the ooliths\carbonate grains (Intercrystal porosity), vugs (isolated or poorly connected pores that are larger than 1/16 mm in diameter), and intra-ooliths porosity (porosity within individual ooliths). The second carbonate is a more heterogeneous Middle Eastern carbonate (MEC) characterized by a variety of microporous ooliths, skeletal and non-skeletal microporous grains. Calcite accounts for more than (99%>) with the existence of minerals like aragonite and micrite. Similar porosity systems that can also be distinguished using the HR images are macroporosity, moldic intra-ooliths porosity (these are formed through selective processes i.e., local dissolution), vugs, and microporous equant cement. Features identifying porosity systems in carbonates have been further discussed in the literature [173, 233-235].

For the preliminary characterization of the samples, Brine permeability, Helium porosity, and permeability measurement were obtained for a 1-inch in diameter by 2-inch core plug of each rock (see Figure 2-1). Then, smaller 6 mm core plugs were drilled from the bigger cores for micro-CT imaging. Finally, Mercury Intrusion Capillary Pressure (MICP) tests were performed on the 6 mm plugs. These tests were performed to assess in (1) choosing the imaging spatial resolutions and (2) choosing safe thresholds for GT segmentation.

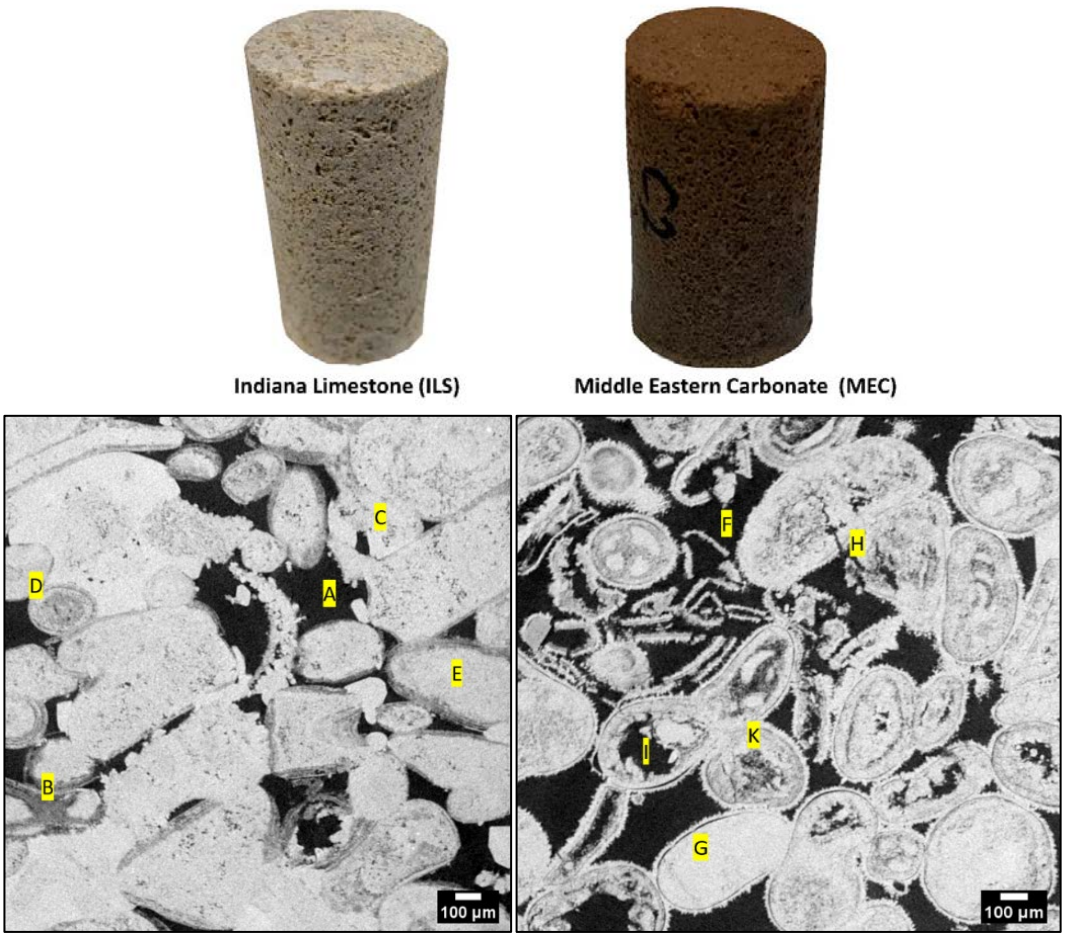

Figure 2-1: (Upper): 1-inch core plug photographs of the Indiana Limestone and the Middle Eastern Carbonate. (Lower): a showcase of a 2D slice of the Indiana Limestone (Left) showing (A) macro-porosity, (B) microporosity on the outer shells of the ooliths (C) vugs, (D) intra-oolith microporosity, (E) solid grain. Middle Eastern Carbonate (right) showing (F) macro-porosity, (G) solid ooliths, (H) microporous equant cement, (I) intra-grain vugs, and (K) microporous ooliths.

2.2.2 Methods

2.2.2.1 Image Acquisition and Processing:

Image acquisition was carefully designed in a way that clearly distinguishes a high percentage of the microporosity at least with a different shade of gray in the HR images. The MICP analysis shown in the Appendix (Figure C) shows a range of micropores below the imaging resolution in Table 1 with a peak of around 1 micrometer. While this is very common in carbonate rocks, we attempt to identify the majority of the microporosity

(showing different voxel intensity than pure solid matrix) as a third phase besides pore and solid phases. Similar approaches have been presented for identifying microporosity and characterizing carbonate rocks in the literature [162, 236, 237]. The imaging and procedures presented for this purpose are adequate for identifying important pore structures to predict permeability using Darcy's law [162]. This is confirmed by comparing permeability from flow simulation with experimental core flooding on larger cores as we show in the result section. Smaller percolating pore structures unresolved using micro-CT images have experimentally been shown a very low permeability of fewer than 5 milli-Darcy in carbonates [238]. The LR images were obtained with a voxel size four times larger than the HR. Both carbonate rocks were imaged at the Tyree X-ray facilities at the University of New South Wales using HeliScanTM micro-CT (Mark I). The system has a Hamamatsu X-ray tube with a diamond window and a high-quality flatbed detector (3,072 × 3,072 pixels, 3.75 fps readout rate). The samples were scanned in a double helix trajectory with 2880 projections per revolution and a filter length of 3 mm in the scanning conditions described in Table 2-1. The reconstruction was performed using QMango software [55, 239] developed by the Australian National University. The imaging setup used to obtain the images with different resolutions is shown in Figure 2-2. A rectangular central domain was cropped from each image and segmented into three phases (pore, solid, and micropores) using two methods: Otsu's multi-thresholding algorithm [88] and Avizo Software TM Segmentation Editor (version 2020.3; FEI Visualization Sciences Group) that uses a combination of watershed and hysteresis algorithms. Otsu's multi-thresholding and watershed-hysteresis based methods have been utilized in literature for segmenting carbonate into three phases [72, 235, 240]. Due to the size of the data, the manual creation of segmentation masks

is not feasible. So, the ground truth segmentation of HR data was obtained through Avizo. In the Avizo segmentation editor, a conservative approach for segmentation was followed by choosing a 'Safe' range of intensities for each phase for the watershed\hysteresis processes. The safe ranges involve first choosing two cutoff thresholds that are certainly pore space and certainly solid matter. All voxels with intensities below the lower threshold are pore, and all voxels higher than the upper threshold are solid. Then, a third range for microporosity with upper and lower thresholds laying between the pore and solid threshold was defined where only obvious microporous textures were labeled. This was achieved based on a visual inspection of all slices of the volume. These regions were then initiated as seeds for watershed\hysteresis. The watershed transforms floods unlabeled regions using the image gradient using the Canny method [241]. The safe thresholding of GT resolved pore space was chosen to have a 'macro' pore space volume fraction equals to the one found in the MICP analysis for each sample (see Appendix).

This method for identifying microporosity and other similar methods [72, 235, 240] can perhaps be plausible for mono-mineralic rocks. In mono-mineralic rocks, the lower grey-scale levels in the solid matrix can be only associated with the existence of sub-resolution porosity (less dense materials). Also, it is important to emphasize this approach has limitations whereby the defined solid phase may still pose a small percentage of porosity at a lower scale (assuming microscale features can be distinguished). However, the effect of these fine-scale porosities is minor when computing macroscale effective properties, i.e., permeability. The identification of

microporosity in multi-mineral rocks would require differential imaging frameworks [219, 222-224].

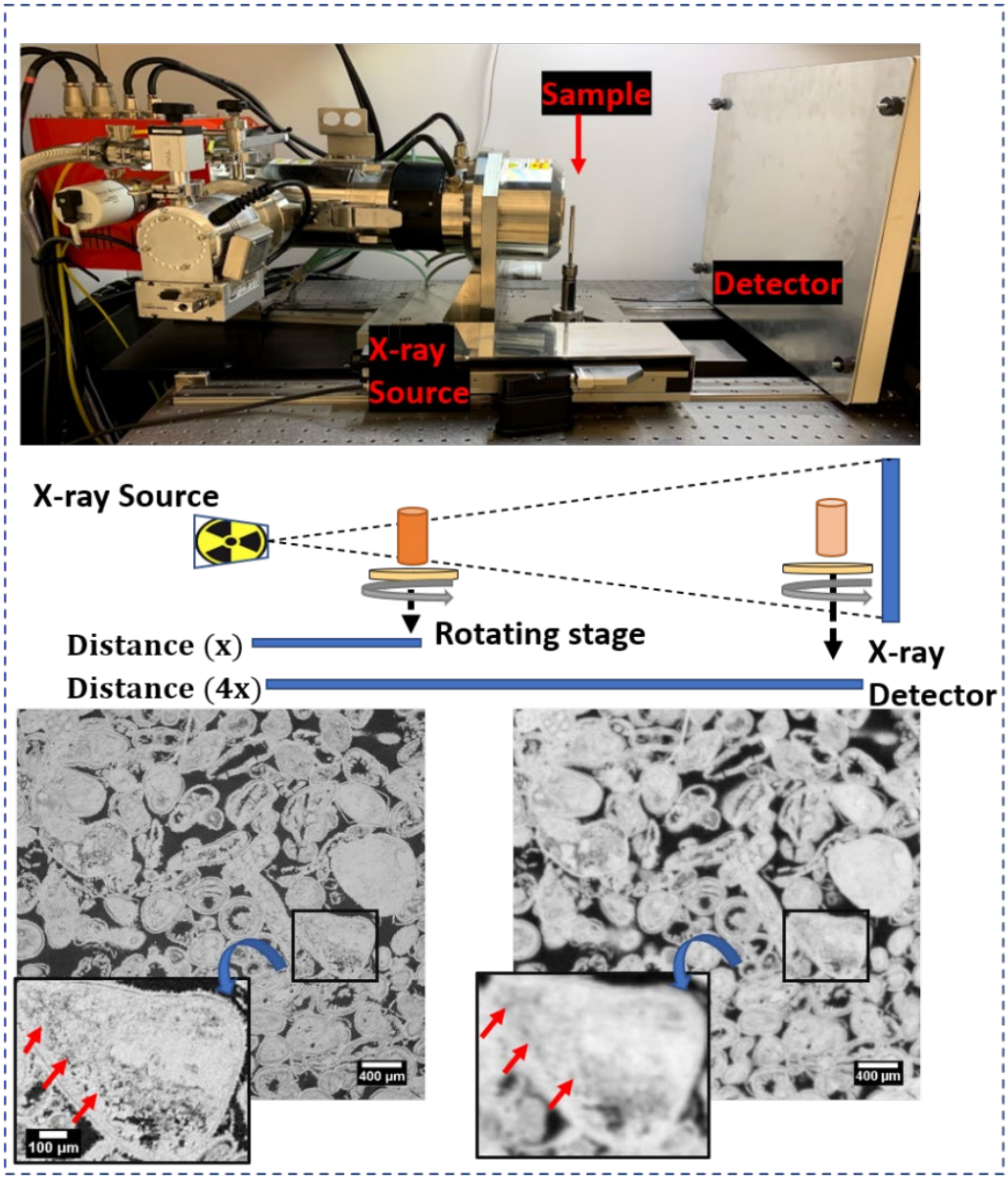

Figure 2-2: The Tyree X-ray micro-CT setup (upper), A schematic showing the imaging procedure used to obtain a multi-resolution image (middle), and slices of the middle eastern carbonate where the magnification showing the resolved microporosity (lower).

Table 2-1:Scanning conditions of the ILS and MEC samples.

Sample Name	Voxel Size (μm)	Distance from source (mm)	Exposure time (sec)	Scan duration (Hrs)	Image size (voxels)
HR MEC	2.68	5.8	0.64	10.5 h	1520×1520×4100
LR MEC	10.72	23.2	0.64	5.1 h	380×380×1025
HR ILS	2.68	5.8	0.64	9.42 h	1520×1520×3552
LR ILS	10.72	23.2	0.64	4.75 h	380×380×888

2.2.2.2 Dataset, Network Architectures, Training, and Inference:

The dataset used for training is titled "Multi-Resolution Complex Carbonates Micro-CT Dataset (MRCCM)" and has been published in the Digital rock Portal (https://www.digitalrocksportal.org/projects/362). The data repository comprises multi-resolution raw tomograms and processed volumes of both carbonate rocks. The MICP analysis of both samples is included in the repository.

Two different frameworks shown in Figure 2-3 were used to obtain the super-resolved segmentation. In one framework we segmented and super-resolved images in one Encoder-Decoder network (End-to-End super-resolved segmentation). In the second framework, we applied a 3D Enhanced Deep Residual Network (EDSR) [242] to obtain a super-resolved grayscale image and then segment the super-resolved using a separate encoder-decoder network. All the network architectures considered are three-dimensional because 3D CNNs tend to learn geometrical features in 3D space which helps in preserving topological features, i.e., connectivity, and generally delivers better results compared to 2D networks [113].

The encoder-decoder networks used in both frameworks are mainly based on the U-net architecture [225]. This architecture was originally designed for 2D image segmentation purposes and has shown excellent performance for biomedical image segmentation and was later modified to handle volumetric data. U-net incorporates symmetric skip connections to link shallow features in the encoder to the equivalent level of the decoder through concatenation\summation. The skip connections improve CNNs performance by alleviating common drawbacks in backpropagation [243] such as vanishing gradients in deep CNNs [244]. Furthermore, the skip connections also help to preserve and combine local and well-detailed features, such as edges, with global features without deep supervision [245]. In this work, we implemented multiple U-net variants where we compared the use of standard U-Net implementation against Residual U-Net. Residual U-Net borrows concepts from ResNet where residual blocks are utilized to achieve better performance.

All networks were trained using Adam optimizer with β1=0.9 and β2=0.999, and L2 regularization of 1e-5 and starting learning rate of 2e-4. The learning rate is halved dynamically during training each time the segmentation evaluation metric reaches a plateau (no improvement) on a separate validation set. The Sørensen–Dice coefficient [246, 247] is used to compute loss between the network output and GT. The Sørensen–Dice coefficient is given in Equation (2-1):

$$\boldsymbol{Sørensen\text{–}Dice\ coefficient}(\boldsymbol{X},\boldsymbol{Y}) = \mathbf{2} \times |\boldsymbol{X} \cap \boldsymbol{Y}| \ / \ (|\boldsymbol{X}| + |\boldsymbol{Y}|) \qquad \mathbf{(2\text{-}1)}$$

where X, Y are two images, and the operator |X| refers to the number of voxels in image X. The symbol ⋂ *refers to the intersection between the voxels of the two images.* The

training was run at least for 100K iterations and stopped when the network learning rate falls below a predefined threshold (1-e6). PyTorch, a DL software package, was used to train the models on an NVIDIA TITAN RTX GPU installed on a PC with Intel I7-8700 CPU @3.20 GHz and a RAM of 64 GB. The U-net\U-Resnet models were trained with a batch size of 2 and domain size of 643 greyscale volumes where the network output a domain size of 2563 super-resolved segmented volume. For the EDSR-U-ResNet framework, the images were first upsampled using EDSR and then segmented using domain sizes of 128^3. In total, 2300 training MEC subvolumes and 1800 ILS training subvolumes were used for training the presented models.

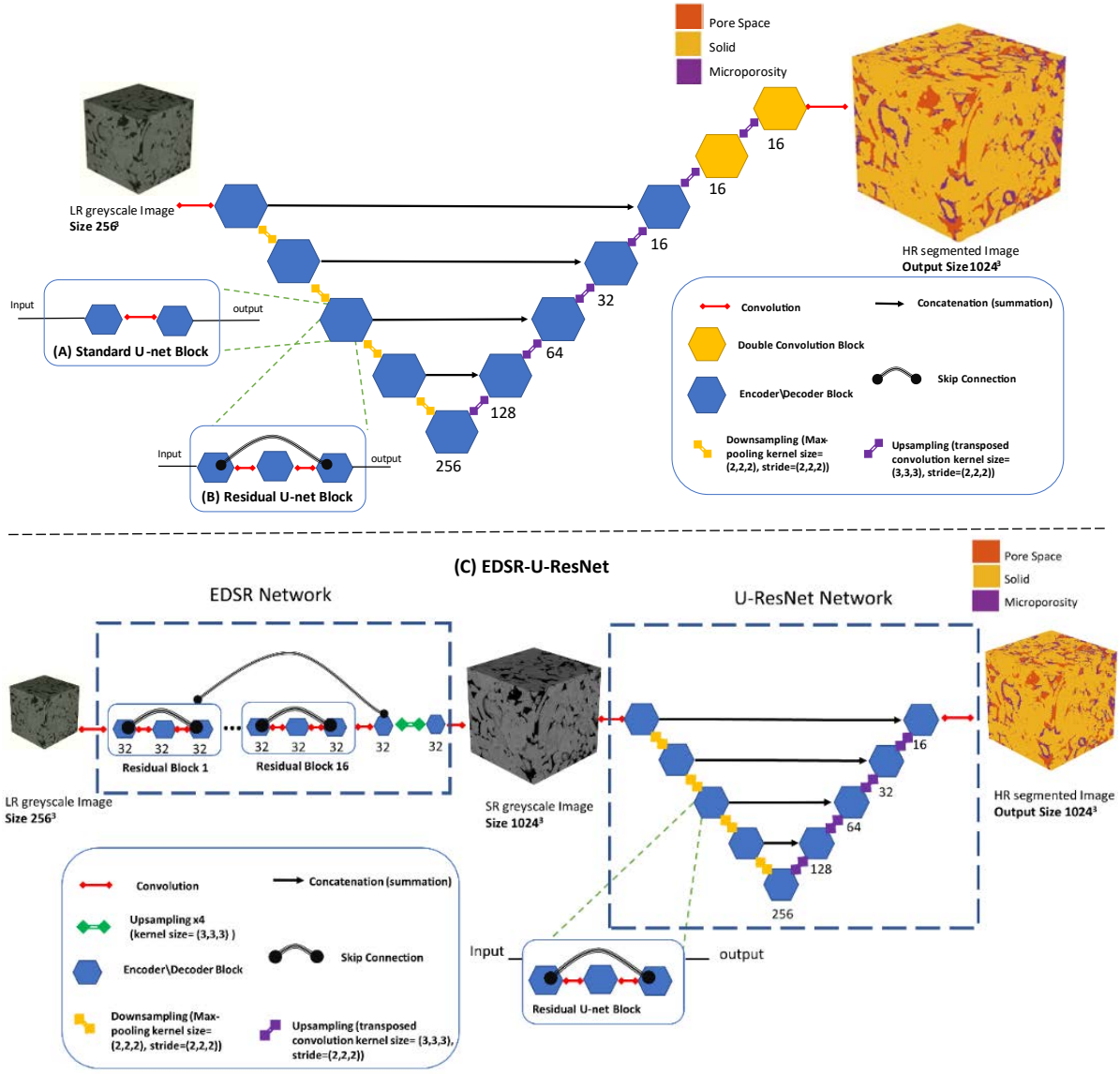

Figure 2-3: A schematic showing the network architectures used for obtaining super-resolved segmentation. The top schematic is showing two highlighted architectures where (A) standard U-net block consists of double convolutional layers as in [225] and (B) the Residual U-net block (U-ResNet) consists of triple convolutional layers with skip connections [248]. The double convolution blocks (highlighted in yellow) at the end of the network increase the input domain size four times. The numbers under each block represent the number of feature maps at each level. In the bottom schematic super-resolved greyscale images are obtained using an EDSR network (C), then segmented using a U-ResNet network. The segmentations obtained from this network is referred to as EDSR-U-ResNet.

A brief description of the evaluation metrics considered is reported. These metrics include voxel-wise accuracy segmentation, topological characterization of each phase,

and measurements of the effective flow properties. Because of the nature of the problem and the imaging framework and processing, several implications might affect how the results are assessed. These implications are caused by:

- Registration of the HR and LR images is not exact, a misalignment in the range of 1-2 voxels may affect the voxel-wise metrics results.
- Image quality\noise levels will significantly control the cutoff volume of resolved features\textures in the HR images, which may be impossible to identify in the LR images.
- Watershed Transform, the GT segmentation method for HR images, requires the user to define "*safe*" thresholds that act as a seed for determining the extent for each phase. While the method minimizes the effect of user bias in general, it still may affect the GT segmentation creation. Regardless of this happening as a source of error, the improvement in segmentation is granted because LR greyscale images are translated based on the HR images of the same region. This leaves less chance of erratic segmentation or user misjudgment.

All the numbers reported are computed from the testing set volumes. These volumes are not used while training or validation.

A. Voxel-wise Accuracy:

We assessed the voxel-wise segmentation accuracy using two segmentation metrics, namely: the Jaccard similarity index [249] and the accuracy of voxel classification using confusion matrices. Jaccard similarity index of phase (P) in two volumes (A) and (B) is given in Equation (2-2):

$$\boldsymbol{Jaccard}(\boldsymbol{A}_{(\boldsymbol{P})}, \boldsymbol{B}_{(\boldsymbol{P})}) \;=\; |\boldsymbol{A}_{(\boldsymbol{P})} \cap \boldsymbol{B}_{(\boldsymbol{P})}| \;/\; |\boldsymbol{A}_{(\boldsymbol{P})} \cup \boldsymbol{B}_{(\boldsymbol{P})|}| \qquad (2\text{-}2)$$

where $\mathrm{A}_{(\mathrm{P})}$ and $\mathrm{B}_{(\mathrm{P})}$indicate the voxels in volumes A and B that are labeled as phase P, respectively. The operator $|\mathrm{A}|$ indicates the number of voxels in volume A. The symbols ∩ and ∪ refer to the intersection and the union between the voxels of the two images, respectively. The confusion charts show the true and predicted voxels percentages of each phase. The diagonal values of the chart represent truly classified voxels percentage and the off-diagonal values represent misclassified voxels percentage. The rate of false positivity and negativity are also reported outside the confusion matrices.

B. Morphological Measurements:

We measured two geometrical properties of each phase which are the porosity and the specific surface area (SSA). Furthermore, the topological connectivity was measured by computing Euler-Poincare characteristic (EC) for resolved macropores only. The porosity of each phase was computed through voxel counting. The specific surface area was computed through the discretization of the Crofton formula [250]. EC was estimated using graph portioning where the numbers of vertices (V), edges (Є), faces ($\mathcal{F}$), and solids ($\mathcal{L}$) of the volume were computed. EC is given in Equation (2-3)[250]:

$$\boldsymbol{EC} = \#\mathrm{V} \; - \#\mathrm{Є} + \#\boldsymbol{\mathcal{F}} - \#\boldsymbol{\mathcal{L}} \qquad (2\text{-}3)$$

Volume fractions, SSA EC are computed using MatImage, an open-source Matlab library for image processing [251].

C. Flow characteristics and pore networks:

For assessing the flow characteristics of the output segmentation, single and multi-phase flow simulations were performed. The comparison includes the segmentations obtained from the HR and LR images using Otsu and watershed methods and the trained models. Also, macropore and micropore pore network models were extracted for each image separately using PoreSpy [252]. Coordination numbers and average pores and throats sizes were compared from the extracted pore network models. The macropore network model was extracted from the resolved pore phase and the micropore network model was extracted from the microporosity phase. The micropore network extraction aimed to give a general indication about the connectivity of the textures looking microporous and should not be misinterpreted to indicate the actual connections of unresolved pore space.

For single-phase flow, we signified the importance of assigning conductivity to the microporosity phase by comparing flow simulations with\without a conductivity assigned to the microporosity phase. The permeability was computed using the Pore Finite Volume Solver (PFVS) [49, 150, 151]. PFVS assigns a conductivity to each voxel according to the proximity of the voxel to the solid wall and the radius of the inscribed flow channel that the voxel belongs to. For simplicity, the microporosity phase was assigned a voxel conductivity based on the Hagen-Poiseuille [141, 253, 254] law where the permeability (K) of a pore throat is assumed to follow Equation (2-4):

$$K \approx \frac{R^2}{8} \qquad (2\text{-}4)$$

for fluid flow with a low Reynolds number where R is the hydraulic throat radius. The contribution of microporosity is known to have lower permeability compared to macropores by several orders of magnitude [162]. Therefore, the assignment of microporosity conductivity was based on the average pore throat radius estimated through the MICP analysis ran on the same cores (See Appendix). The conductivity in the microporous phase is estimated to be 2.45×10^{-13} m^2 in the MEC and 1.25×10^{-13} m^2 in the ILS.

For the multi-phase flow simulation, relative permeability was computed using MorphLBM [255]. This method applies an accelerated morphologically coupled multiphase Lattice Boltzmann Method directly on the macropore space. The microporosity phase is assumed to be fully saturated with the wetting phase and the absolute permeability of macropores is only considered. In the beginning, the fluid configuration is initialized morphologically and updated after LBM steady-state conditions are reached, with small increments of erosion and dilation to target saturation. The LBM simulation continues its execution at the same time as the small morphological increments are updated. Once the target saturation is achieved, the LBM is performed until the capillary number is stable. Then, the steady-state relative permeability point is recorded, and another cycle is launched. For the simulation compared in the results section, imbibition simulations were performed on each segmentation with relaxation applied every 1,000 LBM timestep between morphs. The saturation increments were set to 5% with a capillarity tolerance of less than 10^{-3} per 1000 timesteps. The system capillary number was held below 10^{-5} to mimic capillary-

dominated two-phase flow dynamics. The wettability was set to be uniform at 45 degrees for all solid voxels for simplicity.

2.3 Results and Discussion

All the comparisons reported were based on unseen\testing subvolumes of size 1024^3 voxels for the HR images and 256^3 voxels for the LR images that correspond to a volume of size 20.6 mm^3. This volume was considered here only for comparison purposes and might be subject to further heterogeneity effects at a bigger scale. The methods presented don't involve upscaling of the physical properties of the medium of interest but rather compares the segmentation accuracy of the models. As such, representative elementary volume analysis is not strictly required for this purpose. Overall, 14 segmented volumes were compared for each of the two carbonate rock types, of which 4 segmented volumes were obtained from the HR and LR through Otsu and Avizo watershed segmentation methods, and 3 segmented HR volumes obtained through the frameworks described in section 2.2.2.2.

2.3.1 Voxel-wise Accuracy

Voxel-wise accuracy was computed based on a separate testing volume of size 256^3 in LR that were super-resolved to a volume of size 1024^3 and compared with the GT segmentation (watershed segmentation) for both carbonate rocks. Both testing volumes are around 20% of the entire tomogram imaged of each rock. The network frameworks generate batches of size 128^3, that are stitched together to construct the testing volume. Three super-resolved segmentation for each rock was segmented and reconstructed, using U-net, U-Resnet, and EDSR-U-ResNet. The voxel-wise percentage of each phase is shown as a confusion matrix for ILS and MEC in Figure 2-4 for all the

networks. Overall, the U-ResNet scheme provides the best voxel-wise accuracy. The U-net results in second place and is very close to the performance margins of U-ResNet. EDSR-U-Resnet shows the highest discrepancy especially in segmenting the MEC rock sample. The same trends are observed in Figure 2-5 as indicated by Jaccard similarity Index where in general U-Resnet tends to perform better than the other models. The confusion matrices in Figure 2-4 and Jaccard indices in Figure 2-5 show the microporosity phase with the highest margins of error (compared to solid and pore phases) both in falsely positive and negative classified voxels. Additionally, the error margins are higher in MEC compared to ILS in general, and this is likely due to the complex microporous textures in the MEC sample.

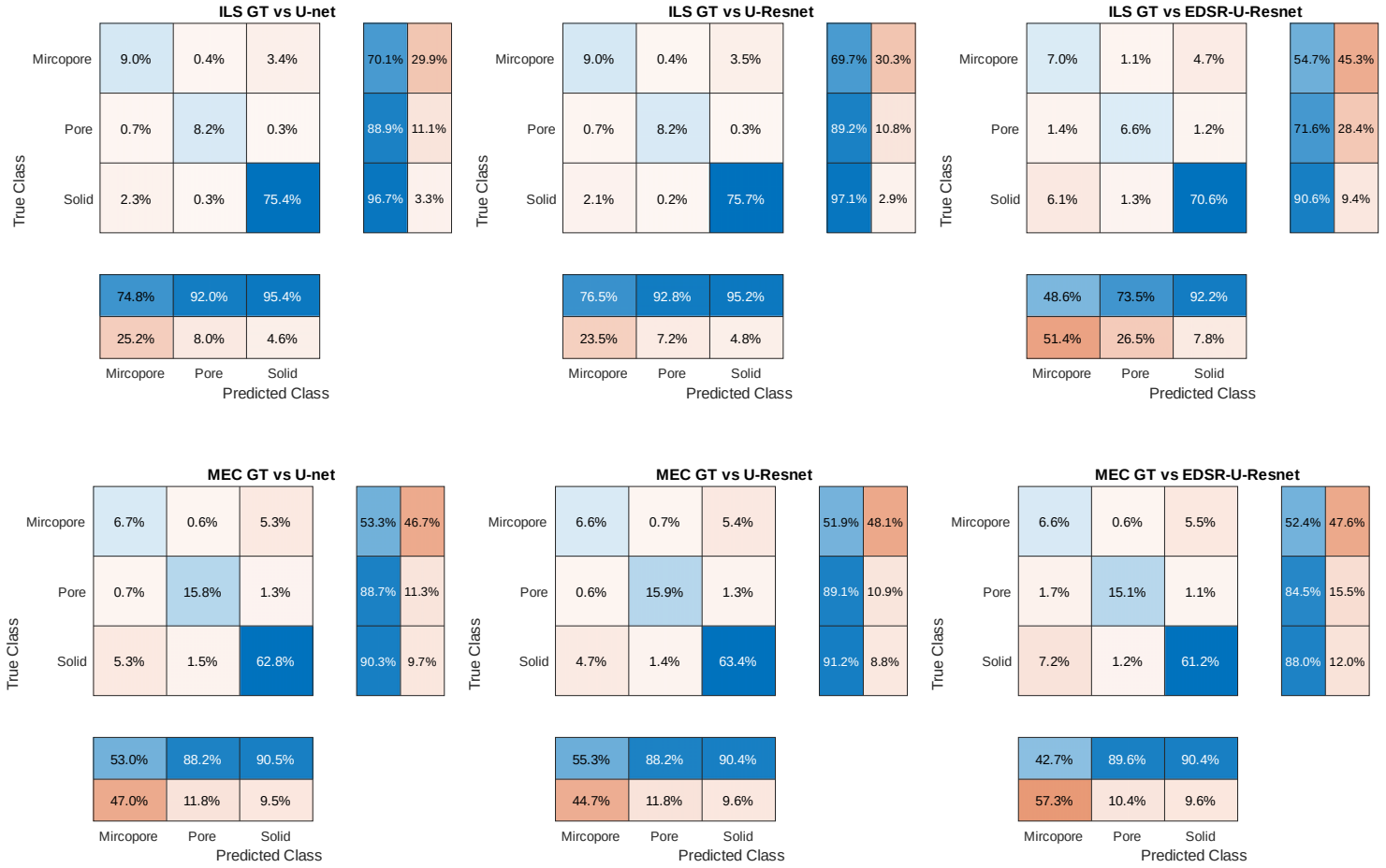

Figure 2-4: The confusion matrices showing the percentage of a phase in each cell. The rows of a confusion matrix represent the true class\GT, and the columns represent the predicted class by the network model. Diagonal and off-diagonal cells represent correctly and incorrectly identified phases classes, respectively. The row and column summaries shown outside the confusion matrices correspond to the percentages of false positive and false negative rates for true and predicted classes, respectively. Warmer color codes show higher error margins.

A comparison between a region of interest for the different models' segmentations is shown in Figure 2-6 and Figure 2-7. The difference maps in Figure 2-6 and Figure 2-7 reveal the misclassified voxels happen mostly at the boundaries, especially the solid\microporosity boundary. This fact is also clearly shown by the confusion matrices in Figure 2-4. This is expected as the greyscale intensities of these boundaries can be impossible to detect, at least visually (see LR images in Figure 2-6 and Figure 2-7). Overall, the incorrect microporosity segmentation perhaps arises from two causes, (1) partial volume effects in LR images which might be interpreted as microporosity by the models, and (2) the tendency of the models to smooth out edges of highly unresolved features\textures. The partial volume effects on the segmentation output are mostly evident near the grain boundaries characterized by strong blurring effects. The network performance is likely to improve by regularization [256] and using more task-specific loss functions [257].

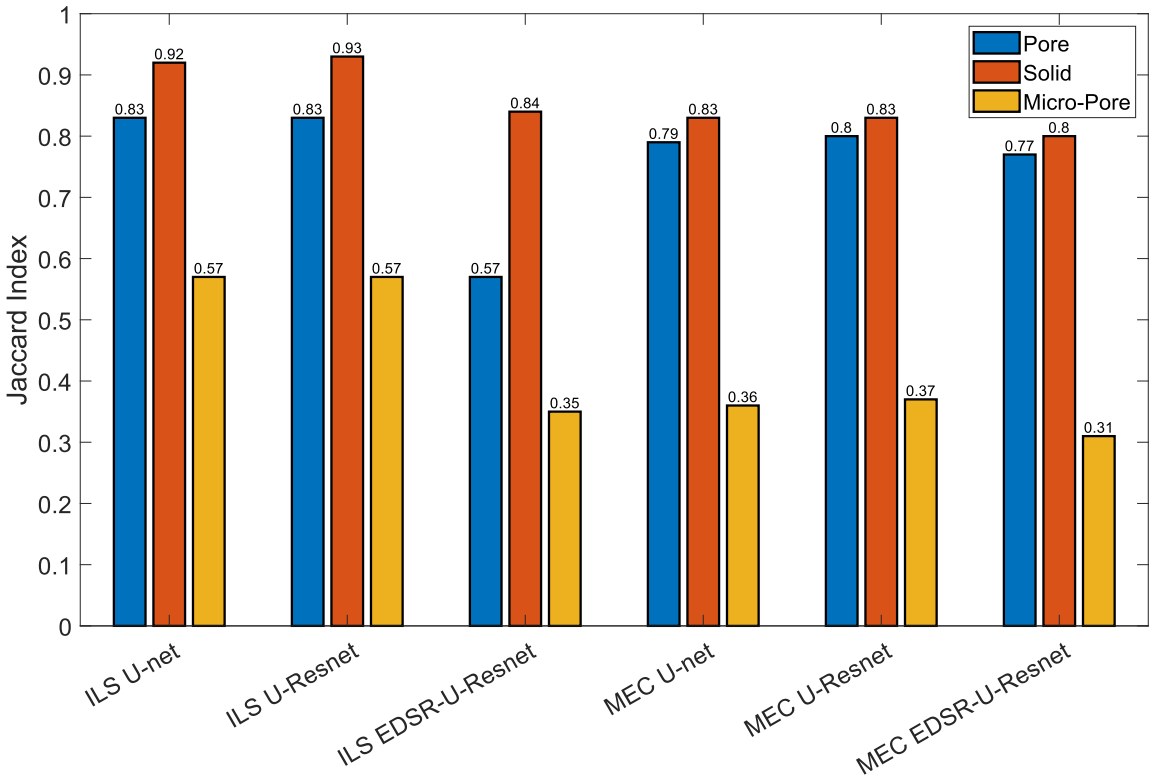

Figure 2-5: Jaccard similarity index of each phase computed for networks' segmentations as compared to the GT segmentation.

From the network architecture perspective, the models' performance ranking was consistent on both rocks where U-Resnet performed best. While the EDSR-U-Resnet framework uses two networks to obtain a super-resolved segmentation as shown in Figure 2-3, this framework poses the highest discrepancy in voxel-wise accuracy. The comparison with other studied models that utilize end-to-end frameworks (LR to HR segmented image) might suggest that EDSR super-resolved greyscale images might not preserve the important features for accurate segmentation.

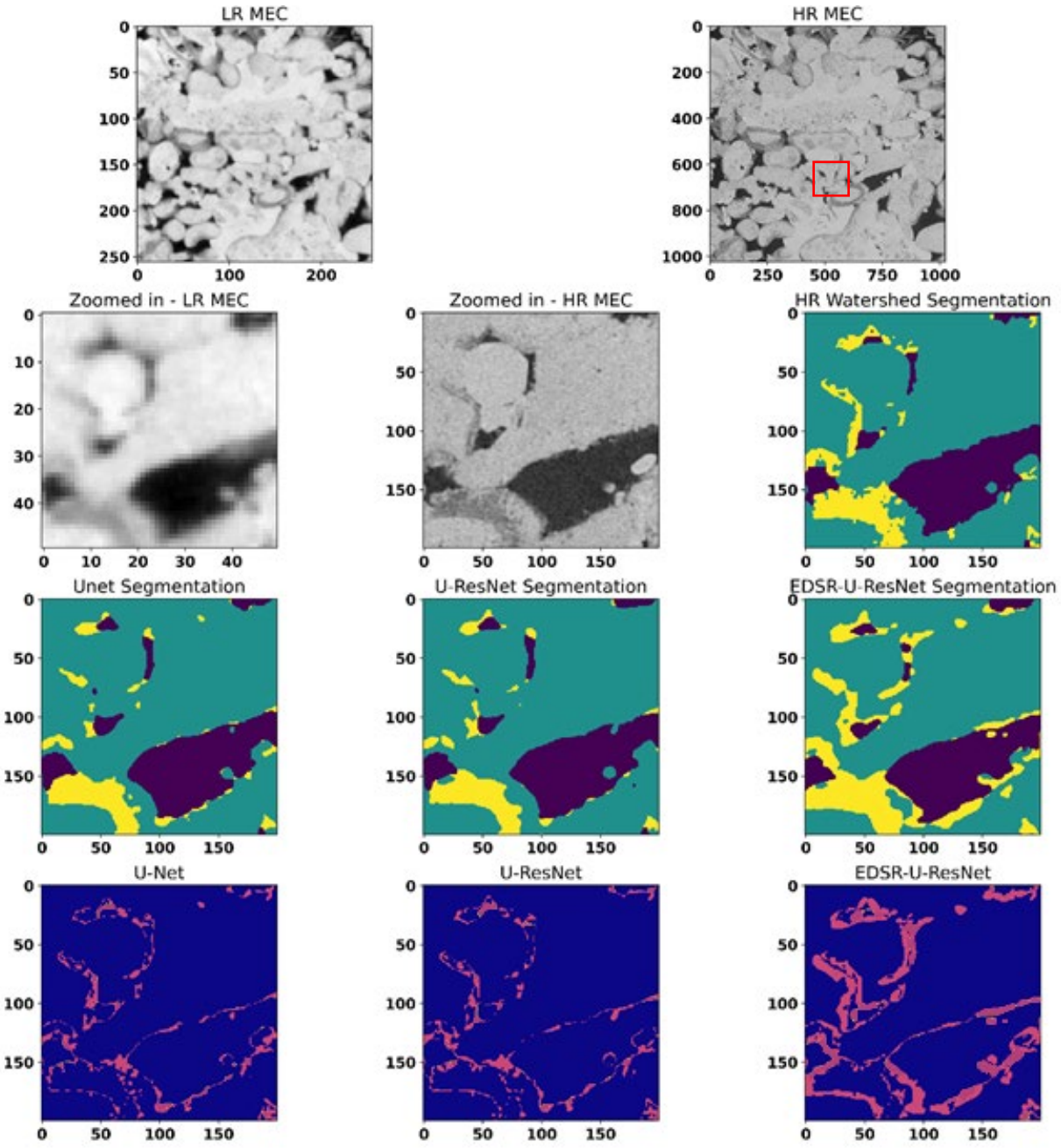

Figure 2-6: 1st row: 2D slices of the ILS testing volume (LR and HR). 2nd and 3rd rows: LR (input to networks) and HR resolution greyscale region of interest as shown in the first row (red square), and the corresponding segmentation (GT watershed and networks segmentations). 4th row: difference maps where networks are compared to GT. The blue color corresponds to correctly classified voxels and the pink color to misclassified phase classes.

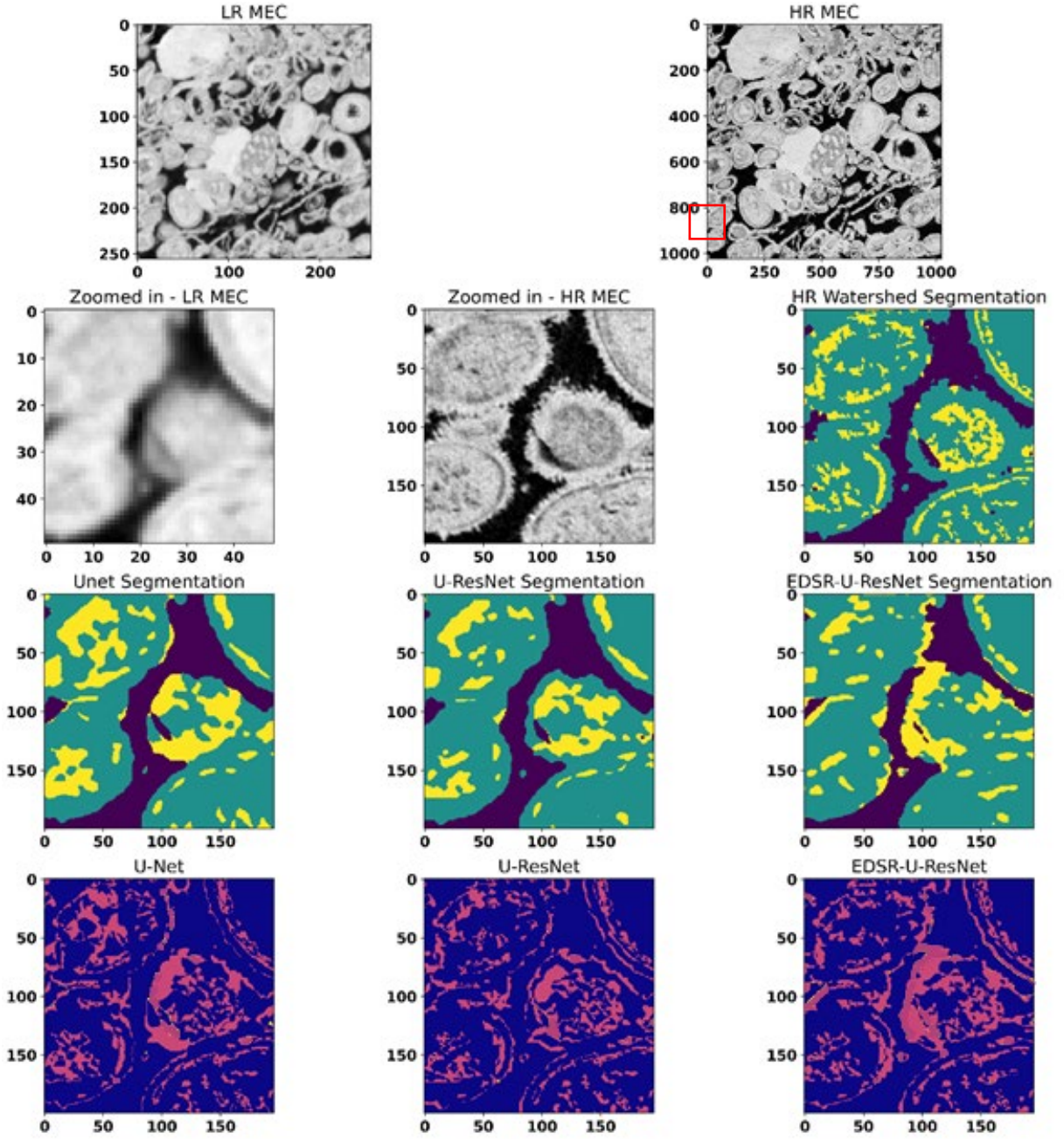

Figure 2-7: 1st row: 2D slices of the LR and HR MEC testing volume. 2nd and 3rd rows: LR (input to networks) and HR resolution greyscale region of interest as shown in the first row (red square), and the corresponding segmentation (GT watershed and networks segmentations). 4th row: difference maps where networks are compared to GT. The blue color corresponds to correctly classified voxels and the pink color to misclassified phase classes.

2.3.2 Morphological Comparison

As an addition to the reported voxel-wise metrics of networks segmentation accuracy, the morphological characteristics of the watershed, Otsu, and the networks segmented volumes are reported. In this section, the watershed and Otsu segmentation of LR and HR volumes are included for a broader comparison. This will give an indication of how CNNs can improve segmentation if compared with other classic methods. The comparison includes the volume fraction and SSA of each phase, and the Euler number of the effective medium pore space. These values are reported for the testing volumes of ILS and MEC in Table 2-2 and Table 2-3, respectively. The measured volume fractions of the trained network segmented volumes clearly provide better results and lower relative difference if compared with the classic methods of segmenting LR volumes. The network segmentations are mainly erratic in estimating the microporosity phase as suggested by previous results, however, more conforming than Otsu HR segmentation where microporosity is overestimated if compared to the GT. The end-to-end models (U-net and U-Resnet) estimate the volume fractions with a relative difference of less than 10%, while the error is found to be up to 22% using the EDSR-U-Resnet framework. The error margins in estimating the SSA of the different segmentations are higher than the volume fractions estimation error margins. However, the SSAs of the network segmentations are again found to be consistent, with a relative difference of less than 50%, while all the other segmentation showed significant relative errors (more than 100%) in the estimation of SSA in some phases. The extreme errors in estimating the SSA perhaps arise from the tendency of the classic methods to create a microporosity phase at solid grains and pore space boundary. This ‘coating’ effect is a byproduct of strong partial volume effects and the nature of sharp global thresholding in classic methods.

Consequently, this observation is expected in the segmentation of the LR volumes where partial volume effects are evident.

The topological connectivity of each segmentation macropore space is assessed based on the measured Euler Characteristic (EC). The results show significant variations in the computed connectivity of pore space with relative differences of around 80% to GT using the trained networks. The variation in EC mostly likely arises from strong imaging artifacts including the translation of partial volume effects to false microporosity. This may create undesired connections between solid grains and hence altering the computed EC. An example of this segmentation error can be seen in the EDSR-U-ResNet segmentation in Figure 2-7. Also, there is always a limitation on the signal\representation that can be resolved as pore space in some parts of the LR images causing connectivity loss in the output network segmentation. Irrespectively, the network segmentations improve the connectivity measured when compared to the LR watershed and Otsu segmentation as shown in Table 2-2 and Table 2-3. It is also anticipated that global thresholding (Otsu method) creates many isolated holes and solids, and redundant loops, hence the high error margins.

Table 2-2: A set of morphological measurements of the Indiana limestone testing volume reported for different segmentation methods. Percentages inside brackets show the relative differences with respect to ground truth segmentation values. EC was calculated for macropore space only.

Indiana Limestone (ILS)	Pore Vol. (%)	Solid Vol. (%)	Micropore Vol. (%)	Pore SSA	Solid SSA	Micropore SSA	EC
HR – watershed (GT)	9.17 (0.0%)	77.95 (0.0%)	12.88 (0%)	0.0199 (0.0%)	0.0621 (0.0%)	0.0628 (0.0%)	8860(0.0%)
HR - Otsu	9.08 (-1.0%)	75.36 (-3.3%)	15.56 (21%)	0.0248 (24.6%)	0.0106 (-82.9%)	0.1302 (107.3%)	-61980 (599%)
U-Net	8.86 (-3.4%)	79.07 (1.4%)	12.07 (-6%)	0.0159 (-20.3%)	0.0362 (-41.7%)	0.0371 (-40.9%)	-1061 (-88%)
U-Resnet	8.81 (-3.9%)	79.45 (1.9%)	11.74 (-9%)	0.0158 (-20.6%)	0.0356 (-42.7%)	0.0354 (-43.7%)	-989 (-88%)
EDSR-U-Resnet	8.92 (-2.7%)	76.60 (-1.7%)	14.48 (12%)	0.0168 (-15.5%)	0.0450 (-27.6%)	0.0465 (-25.9%)	-4261 (-51%)
LR - watershed	8.29 (-9.6%)	84.91 (8.9%)	6.80 (-47%)	0.0407 (104.7%)	0.0738 (18.8%)	0.0525 (-16.4%)	-38 (-99%)
LR - Otsu	8.33 (-9.2%)	76.85 (-1.4%)	14.83 (15%)	0.0451 (126.8%)	0.0962 (54.9%)	0.1393 (121.7%)	-573 (-93%)

Table 2-3: A set of morphological measurements of the Middle Eastern Carbonate testing volume reported for different segmentation methods. Percentages inside brackets show the relative difference with respect to ground truth segmentation values. EC was calculated for macropore space only.

Middle Eastern Carbonate (MEC)	Pore Vol. (%)	Solid Vol. (%)	Micropore Vol. (%)	Pore SSA	Solid SSA	Micropore SSA	EC
HR – watershed (GT)	17.81 (0.0%)	69.53 (0.0%)	12.66 (0.0%)	0.0434 (0.0%)	0.1288 (0.0%)	0.1066 (0.0%)	-30806 (0.0%)
HR - Otsu	16.23 (-8.9%)	63.76 (-8.3%)	20.01 (58.0%)	0.0512 (18.1%)	0.1698 (31.8%)	0.2178 (104.3%)	-115448 (274%)
U-Net	17.90 (0.5%)	69.37 (-0.2%)	12.72 (0.5%)	0.0345 (-20.4%)	0.0812 (-37.0%)	0.0594 (-44.3%)	-5877 (-80%)
U-Resnet	17.97 (0.9%)	70.15 (0.9%)	11.88 (-6.2%)	0.0351 (-19.0%)	0.0806 (-37.4%)	0.0575 (-46.0%)	-5979 (-80%)
EDSR-U-Resnet	16.79 (-5.7%)	67.68 (-2.7%)	15.53 (22.6%)	0.0320 (-26.2%)	0.0803 (-37.7%)	0.0727 (-31.8%)	-2205 (-92%)
LR - watershed	14.27 (-19.9%)	72.20 (3.8%)	13.53 (6.9%)	0.0757 (74.7%)	0.1364 (5.9%)	0.1183 (11.0%)	-515 (-98%)
LR - Otsu	12.67 (-28.8%)	67.12 (-3.5%)	20.20 (59.5%)	0.0751 (73.1%)	0.1458 (13.2%)	0.2165 (103.1%)	-1520 (-95%)

2.3.3 Macro- and Micropore Networks, Single and Multi-phase Flow Analyses

The flow features of the segmented volumes are probably the most crucial measures for assessing the accuracy of the super-resolved segmentation. Hence, pore and micropore networks, single and multi-phase flow simulations are analyzed. Macro- and micro-pore networks are extracted 'separately' for the different segmentations considered. The statistics of these networks and the single-phase permeability values are reported in Table 2-4 and Table 2-5 for the ILS and MEC samples, respectively.

The coordination number (i.e., the average number of pore throats connected to a pore body) is computed to estimate the connectivity from the macropore and micropore networks. The results show more consistent trends when computing the coordination number of the macropore compared to the micropore networks. For the macropore networks, the LR segmentations show lower coordination numbers compared to the GT, this is perhaps due to the loss of tight pore throats during segmentation. However, the CNNs segmentation seems to preserve similar connections showing minor differences in the computed coordination number. For the micropore networks, the CNNs segmentation seems to overestimate the connections in general. This is mainly because the adherence to boundaries of the super-resolved segmentation is prone to relatively high errors. The average pore sizes, pore throat lengths, and diameters show in general a similar trend, where the CNNs improve the computed statistics. Moreover, it is also generally observed that the ILS results are again more conforming compared to MEC because of the lower microporosity in ILS.

Table 2-4: Statistics of the macro- and micropore networks and the PFVS single-phase permeability for the ILS testing sample using different segmentation methods.

Indiana Limestone (ILS)	Coordination Number	Avg. Pore Size (m)	Avg. Throat Length (m)	Avg. Throat Diameter (m)	K_{macro} (mD)	$K_{macro + micro}$ (mD)
HR – watershed (GT)	2.5 /2.1	2.4E-5 /1.5E-5	9.8E-5 /1.2E-4	2.2E-5 /1.2E-5	139	175
HR - Otsu	2.6 /1.6	2.2E-5 /1.0E-5	1.0E-4 /2.0E-4	1.9E-5 /7.1E-6	91	129
U-Net	2.7 /3.1	3.0E-5 /2.1E-5	9.4E-5 /8.0E-5	2.6E-5 /1.7E-5	147	180
U-Resnet	2.6 /3.2	2.9E-5 /2.1E-5	9.5E-5 /8.1E-5	2.6E-5 /1.8E-5	142	174
EDSR-U-Resnet	2.1 /2.9	2.6E-5 /2.2E-5	9.5E-5 /8.0E-5	2.6E-5 /1.7E-5	130	176
LR - watershed	1.7 /1.3	7.6E-5 /5.1E-5	2.6E-4 /2.9E-4	4.7E-5 /3.3E-5	35	41
LR - Otsu	2.1 /1.6	7.2E-5 /1.0E-5	2.8E-4 /2.0E-4	3.9E-5 /7.1E-6	67	104

Table 2-5: Statistics of the macro- and micropore networks and the PFVS single-phase permeability for the MEC testing sample using different segmentation methods.

Middle Eastern Carbonate (MEC)	Coordination Number	Avg. Pore Size (m)	Avg. Throat Length (m)	Avg. Throat Diameter (m)	K_{macro} (mD)	$K_{macro + micro}$ (mD)
HR – watershed (GT)	2.5 /1.4	2.0E-5 /9.8E-6	9.2E-5 /1.4E-4	2.0E-5 /6.7E-6	960	1007
HR - Otsu	2.7 /2.2	2.0E-5 /9.8E-6	9.3E-5 /2.8E-4	1.6E-5 /5.8E-6	490	560
U-Net	2.9 /2.8	2.7E-5 /1.8E-5	9.1E-5 /7.9E-5	2.3E-5 /1.2E-5	1125	1411
U-Resnet	2.8 /2.7	2.7E-5 /1.8E-5	9.1E-5 /7.8E-5	2.3E-5 /1.2E-5	1114	1348
EDSR-U-Resnet	2.3 /2.6	2.7E-5 /1.9E-5	9.2E-5 /8.4E-5	2.5E-5 /1.2E-5	1133	1216
LR - watershed	1.9 /3.3	1.9E-5 /4.3E-5	7.3E-5 /7.5E-4	1.1E-5 /2.3E-5	751	819
LR - Otsu	2.0 /1.1	1.7E-5 /5.1E-5	7.4E-5 /4.2E-4	9.4E-6 /2.6E-5	411	499

For single-phase flow, the permeability in Table 2-4 and Table 2-5 is computed with and without assigning conductivity to the micropore phase. The addition of microporosity conductivity increases the computed permeability, as both rocks pose relatively high percentages of unresolved porosity. However, the contribution to the computed permeability might not be as significant to the macropore phase. In any case, the CNNs segmentation show more accurate permeability values compared to the simulation ran on LR segmented images. More interestingly, U-net and U-ResNet specifically present more accurate permeability values than the HR Otsu segmentation with and without microporous conductivity. Looking over all the results and metrics, it might be concluded that U-ResNet and U-net provide the best and second-best results, respectively. The permeability of the ground truth and networks show in general a good agreement with the experimental Helium permeability (Klingenberg-corrected) on bigger cores of the ILS (221 mD) and MEC (1092 mD) samples.

For further comparison, multiphase flow experiments are run on the U-ResNet, LR, and HR watershed segmentations of both rocks using MorphLBM. The secondary imbibition experiments are simulated on the testing volumes macropore space using the Australian National Computational Infrastructure (NCI) supercomputer Gadi. The microporosity is assumed to be fully saturated with the wetting phase. The simulation of the LR watershed segmentation did not converge to a solution. The reason is likely to be the low connectivity of the pore space and the narrow flow paths. The results from the GT and U-ResNet show a good match on both MEC and ILS samples. The computed relative permeability curves in Figure 2-8 show similar saturation endpoints for water (wetting phase) and oil (non-wetting phase). The topology of the non-wetting phase during pore

desaturation is observed to be analogous in both GT and U-ResNet segmentation (see Figure 2-9). The difference maps visualized in Figure 2-9E show minor differences in the non-wetting phase distribution. These differences happen mainly: (1) at the boundary of grains\fluids interface (segmentation differences) and (2) the filling\desaturation of smaller pores, which perhaps arise from differences in the overall pore topology.

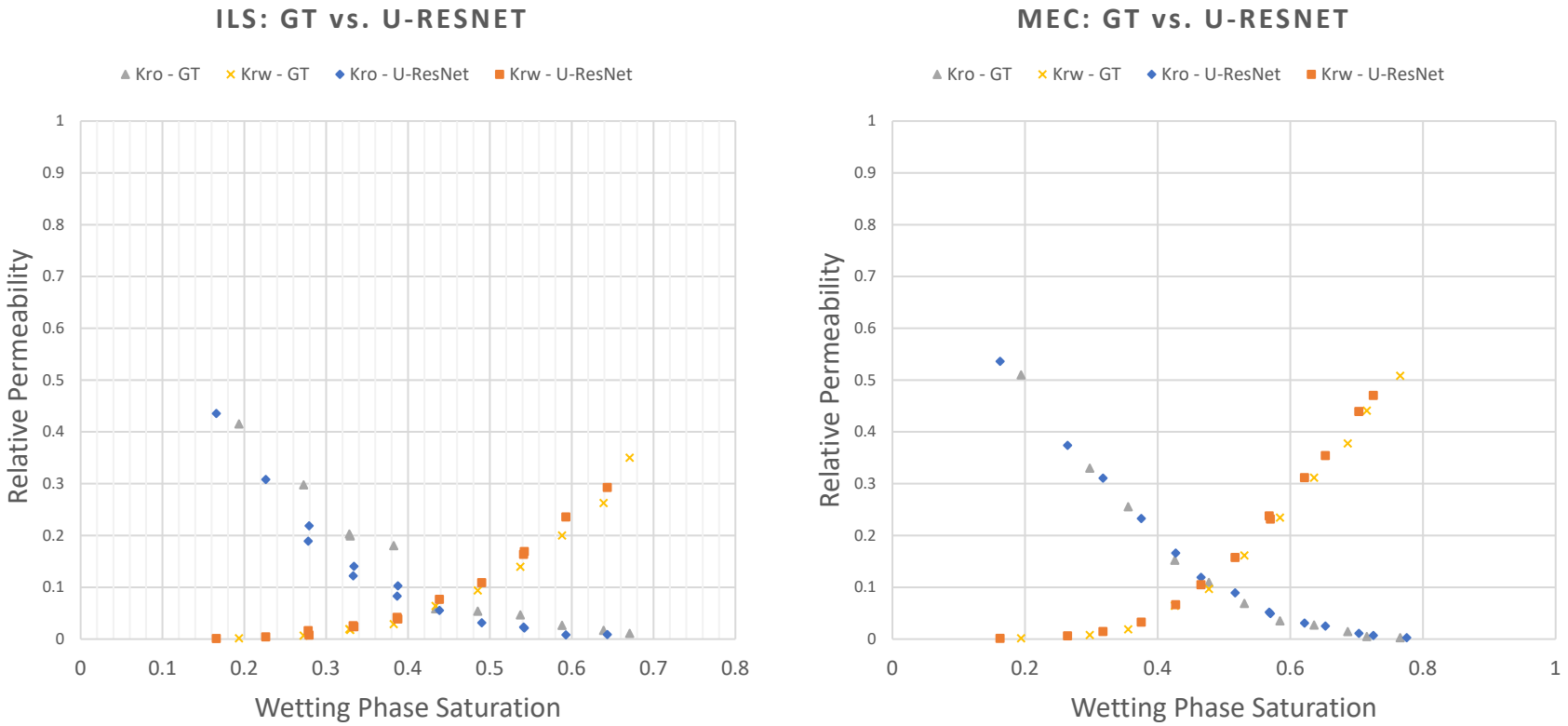

Figure 2-8: Secondary Imbibition Relative Permeability Curves of (left) the Indiana limestone and (right) Middle Eastern Carbonate. The ground truth and U-ResNet segmentation are compared. Matching curves and relative permeability endpoints with minimal differences are observed.

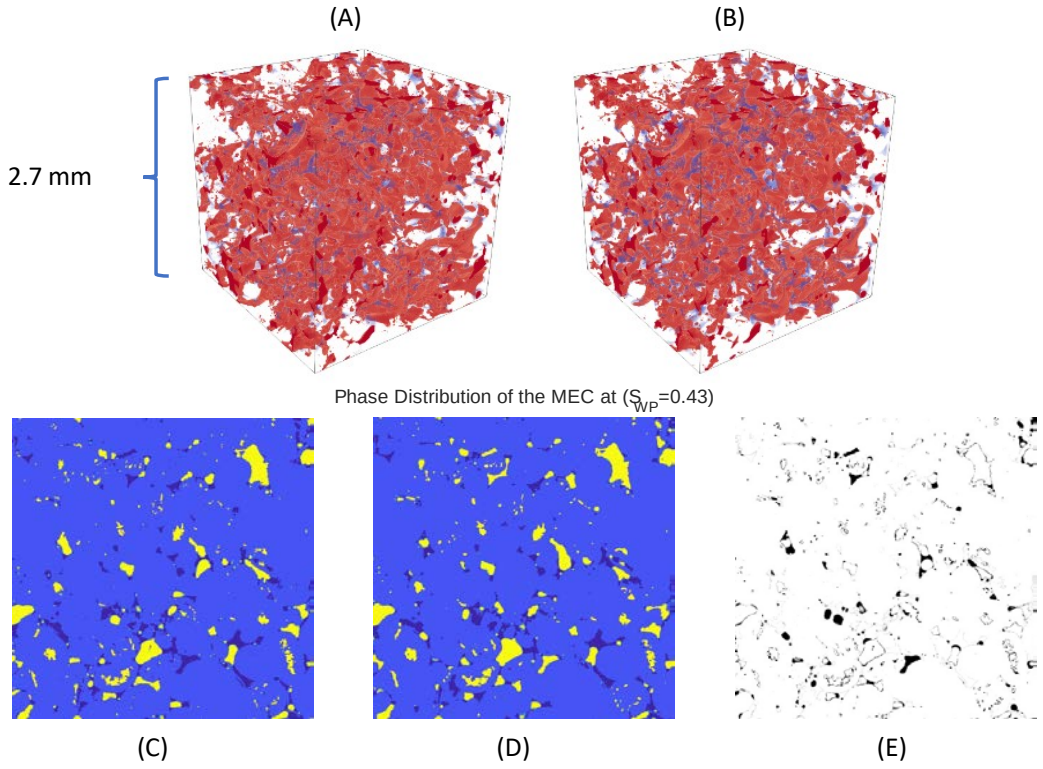

Figure 2-9: Visualizations of the imbibition simulation on the Middle Eastern Carbonate cubic sample at wetting phase saturation of (S_{wp} =0.43). Upper: 3D visuals of the non-wetting phase distribution (red) in the (A) GT and the (B) U-ResNet segmentation. Lower: 2D slices showing the non-wetting phase distribution (yellow) of (C) the GT and (D) U-ResNet segmentations. The difference map in (E) shows that most of the discrepancies happen in the filling of smaller pores and the boundaries of solid and fluids (segmentation differences).

2.4 Conclusion

The segmentation\identification of pore space, sub-resolution porosity, and the solid matrix are vital for reliable DRA frameworks. DL workflows involving the utilization of CNNs to enhance the segmentation of greyscale images improve the overall outcome. CNNs can work in an end-to-end scheme to super-resolve and segment raw X-ray images, without any interference from the user. This reduces the user prejudice associated with classic segmentation methods which often require user input. Two CNNs

training configurations were considered to super resolve and segment greyscale images into pore space, solids, and micropores. Firstly, U-Net and U-ResNet were trained in an end-to-end manner to super-resolve and segment images in one network. Secondly, EDSR-U-Resnet was trained to super-resolve greyscale images at once then segment the image (two different networks). The output segmentation of all the CNNs frameworks shows relatively consistent voxel-wise accuracy compared to the GT segmentation. The U-ResNet displayed the best performance with Jaccard indices of 0.92, 0.83, and 0.57 for solid, pore, and micropore phases, respectively. U-Net show very close voxel-wise accuracy margins to U-ResNet (with less than 1% difference in Jaccard score). In general, the highest error margins are observed in the identification of the microporosity phase. This is perhaps due to the effects of the noise (partial volume effects) and extreme sub-resolution in the input LR images, making it impossible to identify microporosity by the CNNs (or even judging visually). The results also show the phases volume fractions of network segmentation are more conforming than using only LR segmentation or HR Otsu segmentation as compared to GT. The same trends in terms of network consistency are observed in measuring specific surface area, however, with higher relative errors (up to 46% using U-ResNet). The connectivity of the pore space as measured using EC number show also high relative differences, when network and GT segmentations are compared (up to 92%). Regardless, the network segmentations show lower relative error compared to HR Otsu, LR watershed, and Otsu segmentations (see Table 2-2 and Table 2-3).

Additionally, macro- and micropore networks comparisons with GT show better results in terms of connectivity, pores, and pore throats sizes for CNNs segmentation. The same

outcome trends are observed in single-phase permeability and relative permeability curves. Overall, the end-to-end training frameworks are found to be superior to using two networks for super-resolution and segmentation confirming the suitability of end-to-end learning to perform more complex tasks. The reason is likely to be the loss of important embedded features that distinguish the different rock phases to obtain precise segmentation when upsampling LR images using the super-resolution network. This leads to a general conclusion that end-to-end CNNs training for X-ray imaging super-resolution and processing promise a lot of improvements to current DRA frameworks. Similar applications to this study can be applied based on single or multiple rock types, where image acquisition includes LR imaging capturing high field of view and HR region of interest imaging capturing more explicit details of pore geometry. Also, the CNNs methods presented here do not necessarily highlight all potential improvements that can be gained. The CNNs frameworks presented only show a general workflow for improving the accuracy in segmentation and modeling. The interpolation of the presented methods on other rocks type can be established by adding subvolumes from the medium of interest to the current dataset and commencing training in a transfer learning scheme. This eliminates the need for training the models from the ground up. The results obtained with more sophisticated CNNs architectures, training data, and ad hoc strategies are anticipated to boost the outcome accuracy. CNNs architectures such as HRNet-OCR [258], and EfficientNet [259] are few examples of the active research of improving network design and performance. The automation of DRA using CNNs would also benefit from including important physical properties, i.e., permeability, as a component in the loss function for optimizing the CNNs performance.

3 Machine Learning for Predicting Properties of Porous Media from 2D X-ray Images

Naif Alqahtani, Fatimah Alzubaidi, Ryan T. Armstrong, Pawel Swietojanski & Peyman Mostaghimi

School of Minerals and Energy Resources Engineering, The University of New South Wales, Sydney, Australia

The contents of this chapter are from a published research paper titled "Machine Learning for Predicting Properties of Porous Media from 2D X-ray Images" Journal of Petroleum Science and Engineering (2020). This chapter answers the second question of the thesis: Can CNNs be used as regression tools for predicting the physical properties of porous media directly from 2D segmented micro-CT images? Can raw greyscale images be used?

The previous chapter demonstrated the capability of DL techniques in processing and segmentation a dataset of Low-Resolution rock images which is a vital step before characterizing the rock and extracting key physical properties. In this chapter, the scope is extended by demonstrating how CNNs can be used as a predictive modeling tool for estimating geometry-based rock properties using 2d X-ray sandstone rock images. The main objective of this chapter is to prove that CNN-based frameworks can rapidly predict key physical properties using binary and greyscale micro-CT images as input with reasonable accuracy.

Abstract

In this chapter, Convolutional Neural Networks (CNNs) are trained to rapidly estimate several physical properties of porous media using micro-computed tomography (micro-CT) X-ray images as input data. The tomograms of three different sandstone types are subdivided to create a dataset consisting of 5,262 training images and 2,000 testing images. Porosity, specific surface area, and average pore size of each image are computed. The proposed CNN framework is trained with binary images and greyscale images separately and the corresponding computed properties. The results from testing the model are promising as the relative error in the determination of porosity, surface area, and average pore size is less than 6% when the model is trained with binary images and less than 7% when greyscale images are used. Other aspects related to model training and optimization are discussed.

Keywords: Machine Learning, Convolutional Neural Network, Digital Rock, Rock properties

3.1 Introduction

In the last two decades, X-ray micro-computed tomography (micro-CT) imaging has expanded our knowledge on physical processes and transport in porous media [1, 2]. Micro-CT imaging provides a three-dimensional representation of porous media internal geometry that can resolve pore structures up to few micrometers or even sub-micrometers [1, 117]. The three-dimensional rock images, often referred to as "Digital Rocks", are obtained by reconstructing a set of two-dimensional x-ray projections recorded while a sample is rotated at different angles [260, 261]. Digital rocks offer a method for petrophysical characterization and provide complementary analyses for traditional laboratory experiments, which are often time-consuming [1]. Digital rocks have been extensively used to study various aspects of rocks such as mineralogy, porosity, pore size distribution, and clay content [46]. Moreover, numerical simulations can be applied on digital rocks for studying various physical processes, such as mechanical properties of rocks [129, 262] predicting rock permeability [126, 263, 264], multi-phase flow, and fluid topology characterization [147, 265, 266] and simulating rock electrical properties [267, 268] by solving the governing equations of different pore-scale phenomena. A typical procedure for rock image analysis includes image acquisition, image processing, and the numerical simulation of the pore space process on the processed images [98, 165]. Image processing involves using image enhancement filters to reduce noise and artifacts of raw images and improve the signal-to-noise ratio [66, 261]. This results in a better phase segmentation through enhancing the image characteristics and increasing the contrast between the phases [168]. This process may not be necessary when processing images with high resolution and quality, as it does not result in a remarkable improvement of the image features [106]. The

segmentation process is the “cornerstone” of the DRA procedure [165]. The significance of the segmentation method choice is confirmed by Leu, et al. [168], where a sensitivity analysis was conducted to measure the impact of the segmentation on the DRA. The study compared the petrophysical properties derived from three different segmentation approaches and validated the results with experimental data. The findings demonstrated that different segmentation methods may result in significant discrepancies in the computed permeability, due to the variations in the pore geometry derived by each segmentation method. The most commonly used segmentation approach is the global thresholding [87, 168]. However, according to the comparative study presented by Iassonov, et al. [87], most of the global thresholding methods fail to produce reliable phase segmentation results, in particular, user-biased methods which require the manual determination of the threshold value, while locally adaptive methods yield more consistent segmentation, such as watershed-based segmentation and converging active contours methods [66].

On the other side, developments in machine learning (ML) have tackled many problems within various fields of science and engineering [269]. ML has been applied in different areas within petroleum engineering [270-272] including production and drilling optimization [273], reservoir characterization [274, 275], and image enhancement of digital rocks tomograms [276]. In particular, ML has been widely used in well log data analysis, such as permeability estimation [271, 277], lithology interpretation [278], and rock typing from electrical logs by predicting the permeability and litho-facies [270]. One of the most popular models in these studies was Artificial Neural Networks (ANNs) [180, 279]. ANNs are non-linear computational algorithms that adaptively learn to perform

tasks through training [32]. A typical structure of a feed-forward ANNs consists of a series of layers, each containing a number of hidden units or “neurons”. Each layer implements an affine transform (a weighted sum of its inputs plus a bias term) followed by a non-linear (typically) element-wise transformation. The output of one layer forms an input to another. Model parameters (weights and biases) are then iteratively updated using error backward-propagation algorithm and stochastic gradient descent differentiable loss function, that corresponds to the problem - i.e. minimise a difference (in some sense) between expected and produced by a network prediction. [32, 104, 279].

The application of ML to date on digital rocks for predicting the petrophysical properties of rocks is relatively limited. Characterization of rock permeability as a key petrophysical parameter of rocks has been investigated using machine learning techniques [280, 281]. Van der Linden, et al. [280] used ANNs as a fitting tool to perform quantitative analysis of the connectivity of the porous system in relation to microstructural properties of pores and grains. Their analysis showed that permeability is highly correlated to specific attributes of the grain and pore networks. They reported that the most dominant feature in determining permeability is the “pore network closeness centrality”, a metric for describing the centrality of the shortest paths between pores, as it controls the internal connectivity and transmission efficiency. They also showed that this metric renders many features describing pore/grain networks redundant in explaining porous media conductance.

Convolutional Neural Networks (CNNs) [185] are a class of ANNs that gained significant attention in recent years in visual recognition problems [176, 282]. CNNs have a similar generic structure to ANNs, with special convolutional and pooling layers. Each convolutional layer has a number of filters that are applied over multiple locations in the input data (image). Applying the same filter across multiple image locations results in weight sharing (fewer learnable parameters) and preserves spatial relationships. Further details about ANNs and CNNs can be found in Goodfellow, et al. [28]. ANNs/CNNs differ from classic machine learning algorithms as they can automatically learn a relevant hierarchy of features (rather than rely on hand-engineered filters\algorithms to extract specific features) to perform classification or regression tasks. This is often useful when dealing with complex real data, such as images [189, 283]. Sudakov, et al. [206] investigated the feasibility of applying machine learning algorithms for permeability prediction using micro-CT images of a Berea sandstone sample. The actual permeability of the sample was calculated using pore-scale network modeling, which is a simplified representation of the rock geometry. They used various features describing rock geometry such as Minkowski functionals to feed several fitting algorithms such as gradient regression trees (XgBoost) [284] and ANNs. They also used CNNs in an end-to-end scheme, that is predicting permeability by feeding binary images to the CNN. Their results confirm the applicability of machine learning algorithms used for permeability estimation and reported CNN had the best regression performance compared to the other methods. This proposed model, however, was trained and tested on subsamples of a homogenous sandstone, characterised by a narrow range of permeability distribution which might not be ideal to generalise to other rock types. In a similar

scheme, digital rock images were also recently used as an input for CNNs to predict P and S-wave velocities from binary two-dimensional Berea sandstone images [24].

Herein, we extend previous work on using CNNs as predictive tools and examine the applicability of CNNs as a regression method to estimate important characteristics of porous media namely: porosity, specific surface area, and average pore size using 2D slices derived from various digital rock images. The proposed framework automates several digital rock subprocesses where the end-user is expected to provide a raw/greyscale image to find its physical property. Such automation can be useful for the scalability to large datasets. This chapter studies properties that are important for the determination of rock permeability. The model predictions are based on either binary or greyscale images as well as with or without segmentation. Finally, detailed analyses of CNN error are presented, followed by recommendations for future work.

3.2 Materials

Three different sandstone samples are selected for this study: Bentheimer, Berea, and Gosford. The samples were imaged at the Tyree X-ray facility at the University of New South Wales. Those are later used to estimate, and test considered models. A subsample of each sandstone is shown in Figure 3-1. These sandstones textures exhibit different grain shapes, minerals, and clay content. Details about the size and resolution of images are reported in Table 3-1.

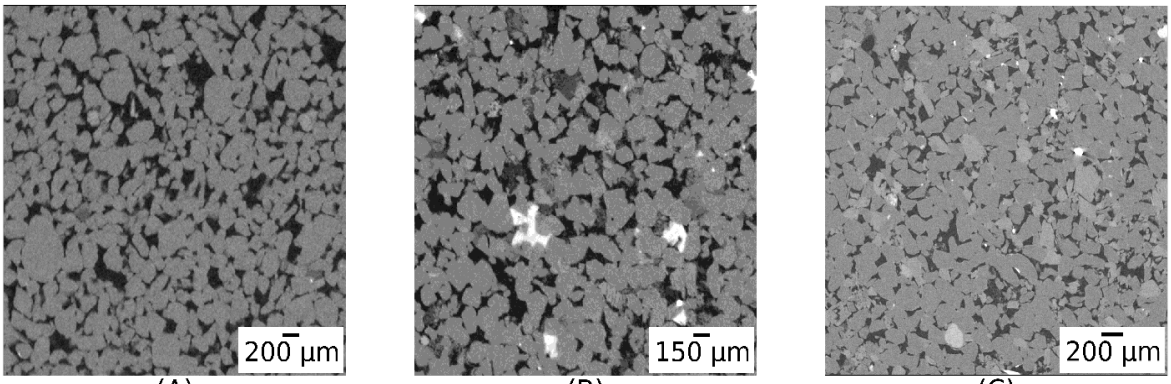

(A) (B) (C)

Figure 3-1: Two-dimensional tomograms of Bentheimer sandstone (A), Berea sandstone (B), and Gosford sandstone (C).

A dataset consisting of 7,626 images is created by subdividing large tomograms of three sandstone samples into smaller regions of interest (ROI). Each ROI is 128×128 pixels and captures various structures that are present in the larger tomograms. This is achieved by shifting the ROI by 128 pixels every step across the full tomogram to capture a new image. As the sandstones studied are fairly homogenous, the ROI size is tuned to capture a representative elementary volume, or the smallest volume over which the measurement is constant for sandstones as suggested by [48].

Table 3-1: Size and Resolution of the images used in this study.

Name	Size (voxels)	Resolution (µm)
Bentheimer sandstone	1600×1600×40	6.8
Berea sandstone	1200×1200×40	5.3
Gosford sandstone	1275×1275×200	2.8

3.3 Methods

The methods used to prepare images and compute the data are discussed in this section. The mathematical operations performed during training the CNN are briefly explained. A general workflow showing micro-CT imaging acquisition, the labels extraction\ computation, and CNN training\testing is provided in Figure 3-2.

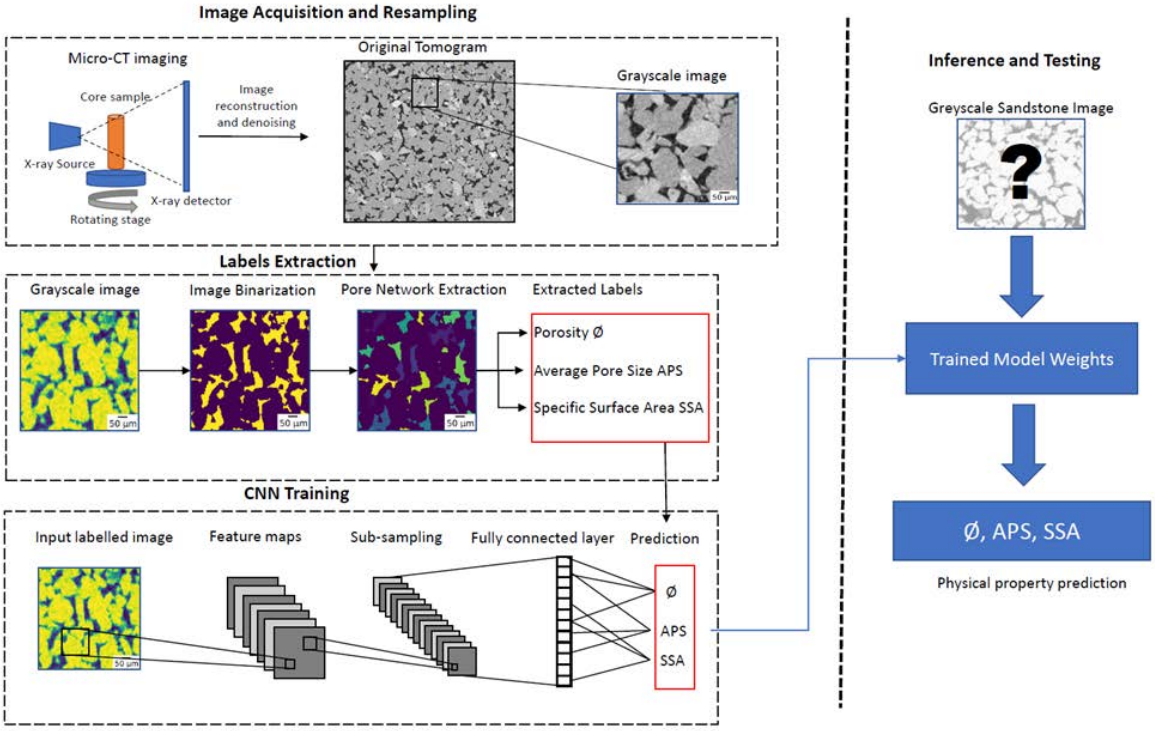

Figure 3-2: The proposed framework for predicting porous media properties using CNNs.

3.3.1 Image Resampling, Segmentation, and Pore Network Extraction

The original micro-CT images of sandstones were captured with different resolutions. Consequently, image resampling was a required step to obtain samples with a similar spatial resolution. The bicubic interpolation is a common method to resample images to different resolutions [285]. The original tomograms resolutions of sandstones are provided in Table 3-1. All images were resampled to a resolution of 4.8 µm/pixel to ensure a comparable result, i.e. average pore size of images. Following resampling,

the tomograms are subdivided into smaller ROIs of 128×128 pixels. Each sandstone type is represented by 2560 ROI. The dataset is then filtered by removing some images containing streak artifacts. Thereafter, 5626 images are chosen for training and 2000 images were preserved for testing the model.

The dataset images are segmented using Otsu thresholding [88] to distinguish/label pore space and solid grains, based on which porosity and specific surface area of each image are calculated. Otsu's method finds a threshold level where intra-class variance, the sum of foreground and background variances, will be at its minimum. Images are segmented using Otsu thresholding implementation in 'Scikit-image', an image processing library in Python. [286].

The pore space of the segmented images is portioned into pores and pore throats using a publicly available network extraction algorithm [142]. First, the algorithm locates the basins (the pores) on tomogram images by applying the watershed algorithm on the distance map of segmented images. Second, the peaks resulted from the watershed algorithm are then identified using a maximum filter. Next, the algorithm automatically eliminates the adjacent peaks which share the same distance value, through an iterative process of dilation. Finally, nearby markers are merged and segmented into pore regions. The pore partitioning parameters are set as follows: Gaussian filter sigma is set to 0.4 and the structuring element radius is set to 4. These values are similar to the settings suggested by [142]. The partitioning setting is validated by comparing the coordination number range of Berea sandstone from 2D images with the results of Rabbani, et al. [140]. A good agreement between the values range is found with a relative error of less than 10% using various 2D images of Berea

sandstone. The average pore of each image is calculated from the extracted network. Figure 3-3 shows (a) a ROI from the Gosford sandstone tomogram, (b) the ROI segmentation using Otsu thresholding, and (c) the extracted pore network.

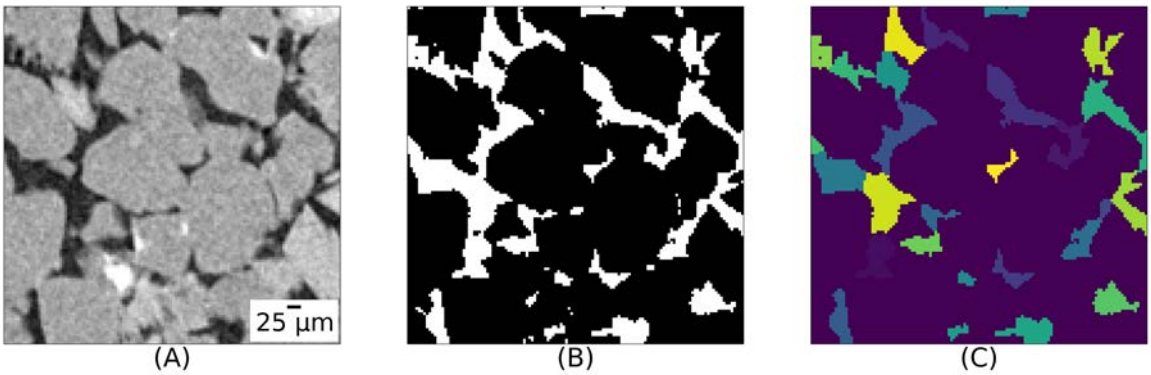

Figure 3-3: (A) greyscale image of the Gosford sandstone; (B) segmented image and (C) the partitioning of pores for pore network extraction.

Labels (or targets) refer to the actual values, commonly known as 'ground truth' in machine learning, computed directly from the binary images and the extracted pore network. Those are used as a supervising signal when training neural networks. For each image in our dataset, porosity, specific surface area, and average pore size are computed and stored for training and testing. Porosity is calculated by dividing the sum of pore pixels by the area of the image. Specific surface area is calculated by dividing the perimeter of the boundary between two phases on the binary image over the image area. The average pore size is calculated from the pore network extracted from each image.

3.3.2 The Convolutional Neural Network Architecture

The main building blocks of the proposed approach are explained in this section. The details presented outline mathematical operations implemented for training and inference with CNN. Similarly, the details of relevant hyper-parameters and network architecture choices are shown. In this work, CNNs are applied for the inference of

labels in an end-to-end manner (for greyscale images), i.e. by feeding raw images to neural networks tasked to predict quantities of interest. CNNs consist of multiple layers of non-linear transformations, that are iteratively learned such that model predictions at the last output layer are close to the expected ground truth targets. Those steps are briefly summarised below.

A. Fully Connected Layers (FC): In a FC layer, each input feature (pixel) gets assigned a separate vector of weights connecting it to all activations at the output. As a result, the FC layers do not preserve spatial structure of their inputs and are typically characterized by a larger number of trainable weights when compared to convolutional layers. The FC layer implements Equations (3-1) & (3-2):

$$\boldsymbol{z^l = W^l x + b^l \#1} \qquad \textbf{(3-1)}$$

$$\boldsymbol{h^l = f^l(z^l)} \qquad \textbf{(3-2)}$$

where W^l, b^l denote weights and biases at $l-th$ layer, x is the layer's input (either raw data or activations from the preceding $l-1th$ layer), z^l are the resulting linear activations that are further transformed in Equation(3-2) by a non-linear activation (transfer) function f^l (refer to point C for more details). Figure 3-4 shows an example of FC to an input image (x).

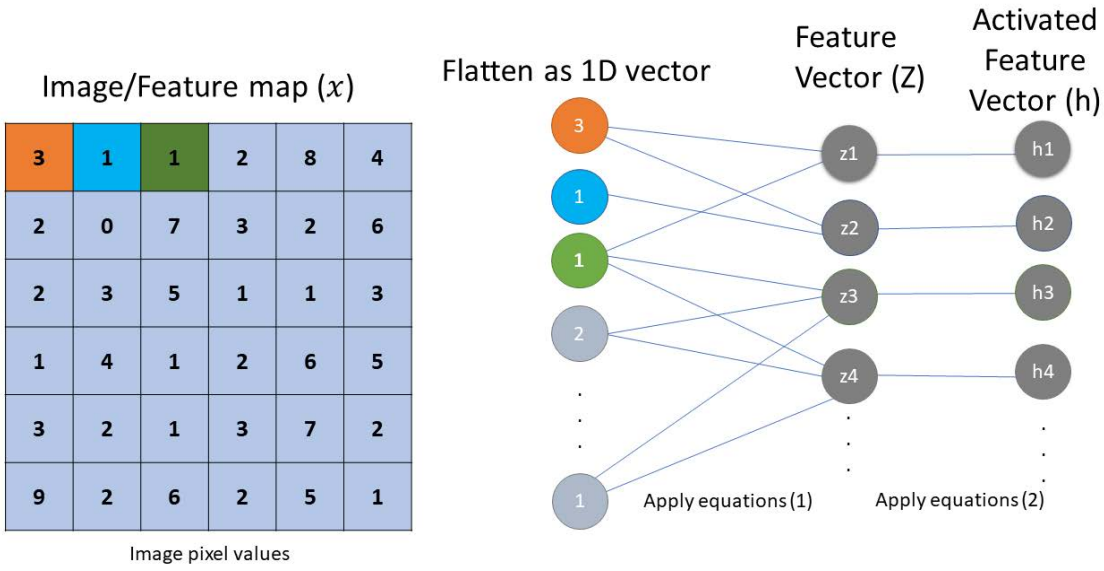

Figure 3-4: Flattening Images/Feature maps as one-dimensional vector.

B. Convolutional layers. Contrary to fully connected layers, convolutional architecture offers several desired properties. The CNN layer is built of a number of local receptors (filters) applied multiple times across the whole input space (See Figure 3-5). This preserves the spatial relationship between inputs and feature maps (i.e. the activations resulting from scanning an image with a specific filer) and enables weight sharing, which reduces the number of learnable parameters. CNNs are naturally suited to computer vision tasks, as specific detectors learned by the filters (i.e. an edge of some orientation) can be reused across several locations in the input image. The convolutional layer thus implements Equation (3-3):

$$\boldsymbol{z_p^l = K^l{}_p * x + b^l{}_p} \qquad (3\text{-}3)$$

where z_p^l denotes the linear activations in the p^{th} feature map at $l-th$ layer, x is the input image (or an output of the preceding layer), K_p^l is the p^{th} filter kernel at $l-th$ layer, b_p^l is its bias term and $*$ is the convolution operator. To obtain CNN layer activations one applies non-linear activation function as in Equation (3-3). Details on particular choices for filter numbers and sizes are reported in Table 3-2. The convolution process is illustrated in Figure 3-5. In this work batch normalization is also used [287] to improve learning convergence. Batch normalization adjusts the activations between layers (i.e. h^l in Equation (3-3)) to have zero mean and unit variance.

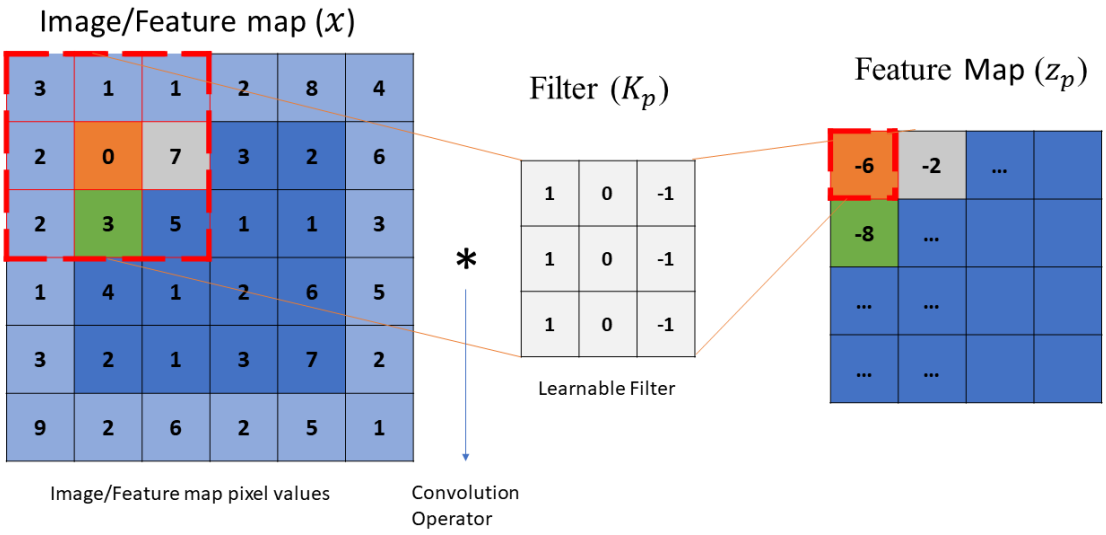

Figure 3-5: Feature maps produced from the convolution kernel.

C. Activation functions. There are many choices for activation functions, some classic choices included sigmoid or hyperbolic tangent. In the networks in this chapter, Rectified Linear Unit activation function (RLU) [288, 289], defined as $f(z) = \max(0, z)$ in Equation(3-2) Contrary to squashing sigmoidal non-linearities, ReLU

does not suffer from vanishing gradient [290] issue in deeper models, is computationally less expensive, and was proved experimentally to offer good results across a variety of tasks.

D. Sub-sampling/Pooling layers: a common practice in CNNs is to periodically subsample feature maps to reduce the spatial size, hence, reduce computational load [291]. This is achieved by applying a Max operation of (2×2 kernel) on all feature maps. This kernel moves two pixels at each step, or has a stride of 2 pixels, to find the maximum as shown in Figure 3-6:

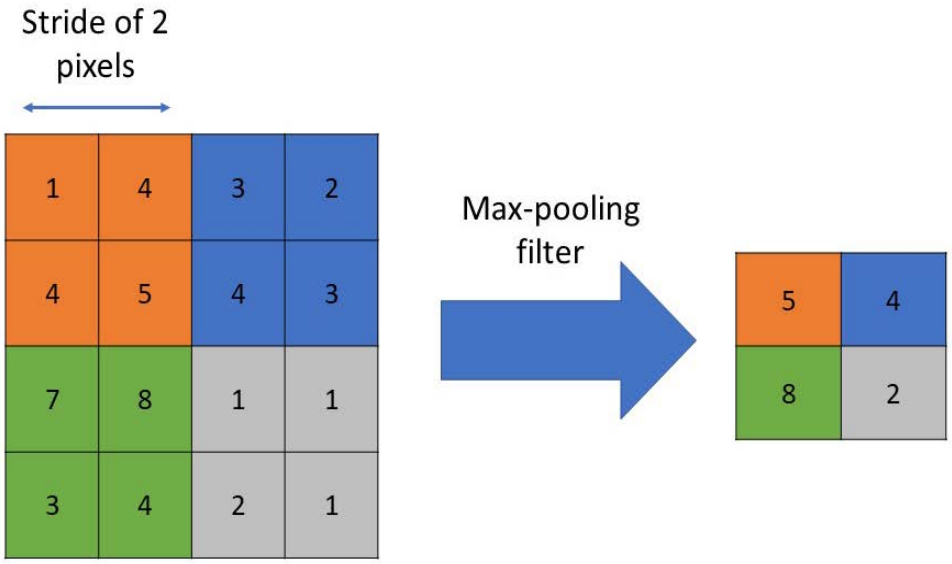

Figure 3-6: An illustration of the pooling operation in CNNs

E. Loss, Optimizer, and Regularisation: we apply a standard technique called 'dropout' [292] at the final fully connected layer to avoid overfitting. When using dropout, during training random activations are ignored in making predictions (their values are set to 0 in Equation (3-2)), thus prevent overfitting by learning spurious correlations between activations. In this work, we apply dropout to 20% of the neurons in the fully connected layer.

The model is trained to minimize the error (loss) between predictions it makes (Y) and the expected ground truth labels (L). In this chapter, the model is tasked to solve a regression task of predicting real-valued quantities, the distance in this work is defined as a Huber loss [293]:

$$L_s(a) = \begin{cases} \frac{1}{2}a^2 & for|a| \le \delta \\ \delta\left(|a| - \frac{1}{2}\delta\right), & otherwise \end{cases} \quad where\ a = Labels\ (L) - Predictions\ (Y) \qquad (3\text{-}4)$$

where δ is a scaler set to 0.5. Huber loss is one of the robust methods to define loss in regression problems and is less sensitive to noise [294].

Huber loss is a hybrid of two losses –mean absolute error and mean square error, activated depending on the threshold hyper-parameter δ (experimental validation of each are reported later). Given the loss in Equation (3-4), one computes top-level errors and back-propagates them through the network in a backward pass to compute gradients in connection with the parameters. Given the gradients, Adam [295] optimizer is used to update the network parameters (weights and biases). Adam allows to use adaptable, parameter specific, learning rates (rather than a single global rate same for all models' parameters).

Neural Networks are typically characterized by a large number of parameters (though this problem is less pronounced in CNNs due to weight sharing) and require a large number of training data points in order to learn a robust relationship between the inputs (images) and the outputs (predictions). The number of data points typically depends on several factors such as the complexity of the problem, the capacity of the model (number of parameters) as well as the

optimization algorithm, and regularising priors. As the number of images in our dataset is limited, we artificially increase the number of our training instances through simple data augmentation methods.

Several data augmentations are applied techniques to improve model performance. In particular, the input images are randomly rotated by 0°, 90°,180° , and 270° , and flip along horizontal and vertical axes are applied. Discussion on data augmentation methods can be found in [28].

The overall architecture of the network used in this work is reported in Table 3-2. 'Stride' in Table 3-2 refers to the filter's shift in pixels at each step (see Figure 3-6). 'Padding' refers to adding pixels to the border of image\feature maps to keep the output size of convolution the same. For the labels extracted directly from binary images (porosity and surface area), the same architecture but with only two convolution layers are used. This turns out to help with the network performance. As the dataset is large and cannot be fed at once, training is commenced using mini-batches of 256 images each. An epoch of training is defined as one full sweep over all images in the dataset. 'TensorFlow' [296] a machine learning library/software has been utilized as a platform for training the network.

Table 3-2: The architecture of the CNN used in this chapter.

Number of layers	Operation	Comment
5 × layers	2D Convolution	Kernel size = (3,3) Stride = (1,1) Padding= “SAME” Number of Filters in each layer [32,32,64,128,256]
	Batch Normalization	
	Rectified Linear Unit (ReLU)	Activation function
	Max Pooling 2D	Kernel size = (2,2) Stride = (2,2), Padding= “SAME”
1 × layer	Flattening	Flatten 2D tensor from the last layer into 1D tensor
	Dense layer	1024 hidden units
	Rectified Linear Unit (ReLU)	Activation function
	Dropout	Dropping out a random 20% of neurons output to prevent overfitting
1 × layer	Dense	Output (the physical property predictions)

3.4 Results and Discussion

In this section, the performance of the proposed CNN architectures is presented. Various aspects of the model, such as accuracy in predicting rock properties from binary and greyscale images, training and testing loss curves, the wall computation time for model training and inference, and error analysis are discussed.

During training, the CNN estimation accuracy increases with every elapsed epoch of training as the filters detecting features in the rock morphology are optimized. The CNN training is stopped when no further minimization of the loss function is observed, i.e., when the loss reaches a plateau for five consecutive epochs. In Figure 3-7, we show the average loss at each epoch during the training and testing of our two convolutional layers architecture. This architecture was utilized after it was noticed that a simpler model with two convolutional layers provides better accuracy for predicting properties directly extracted from binary images which are porosity and specific surface area. For properties extracted indirectly using pore network extraction and regression using greyscale images, we used a deeper model and the architecture is reported in Table 3-2.

We briefly experimented the use of different cost functions to compute the loss such as the mean squared error (L2 loss), the absolute mean error (L1 loss), and Huber loss. The results show Huber loss offers the minimal average relative error for the model prediction on the testing test. In Table 3-3, we report the final average relative error in predicting porosity from binary images using L2 loss, L1 loss, and Huber loss.

Table 3-3: A comparison between the final loss using different loss functions.

Loss Function	Huber Loss	Mean Squared Error (L2)	Absolute Mean Error (L1)
Final Absolute Error Percentage in Porosity (Ø)	2.80%	4.50%	5.4%

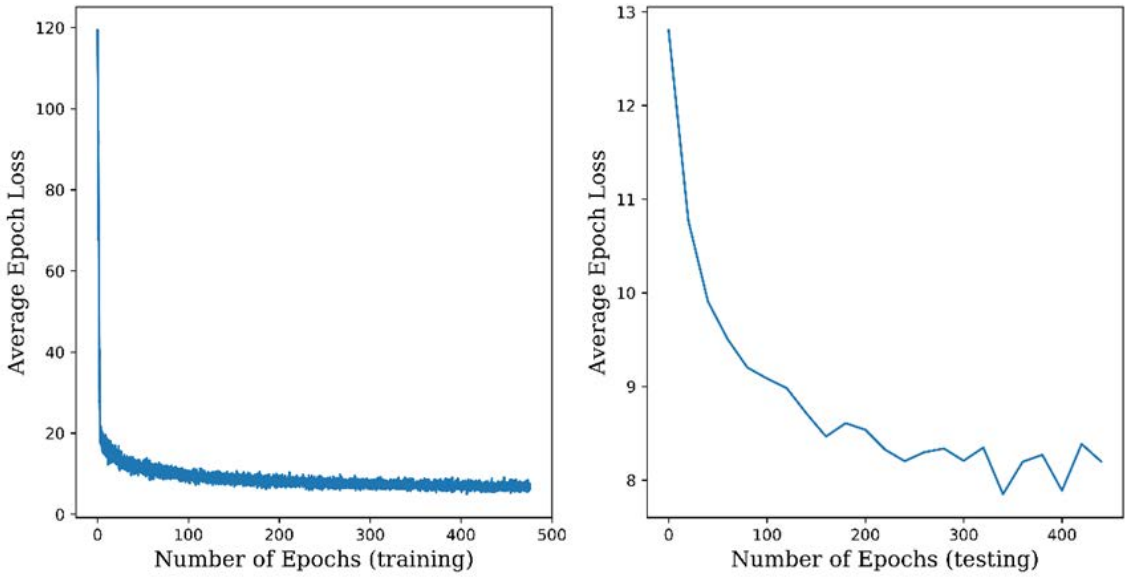

(A) (B)

Figure 3-7: Average epoch loss during training (A) and testing (B). The model is evaluated with the testing set after every 20 epochs.

In the following, the regression plots of each property versus actual ground truth labels are plotted. All the results shown are based on the testing image dataset unless otherwise stated.

3.4.1 Porosity

The idea behind predicting porosity from binary images is strictly serving as proof of concept. It is the first step to show that CNNs can be utilized as a predictive tool to estimate more computationally expensive properties from micro-CT images. CNN predictions score on the R-squared metric is 0.96, and the average relative error between labels and predictions is less than 3% for binary images. For greyscale images, prediction accuracy is lower, as expected, with an average relative error between predictions and labels of 6.3%. Figure 3-8 shows the actual porosity labels plotted against our CNN predictions. The distribution of porosity values and CNN predictions are shown as marginal histograms.

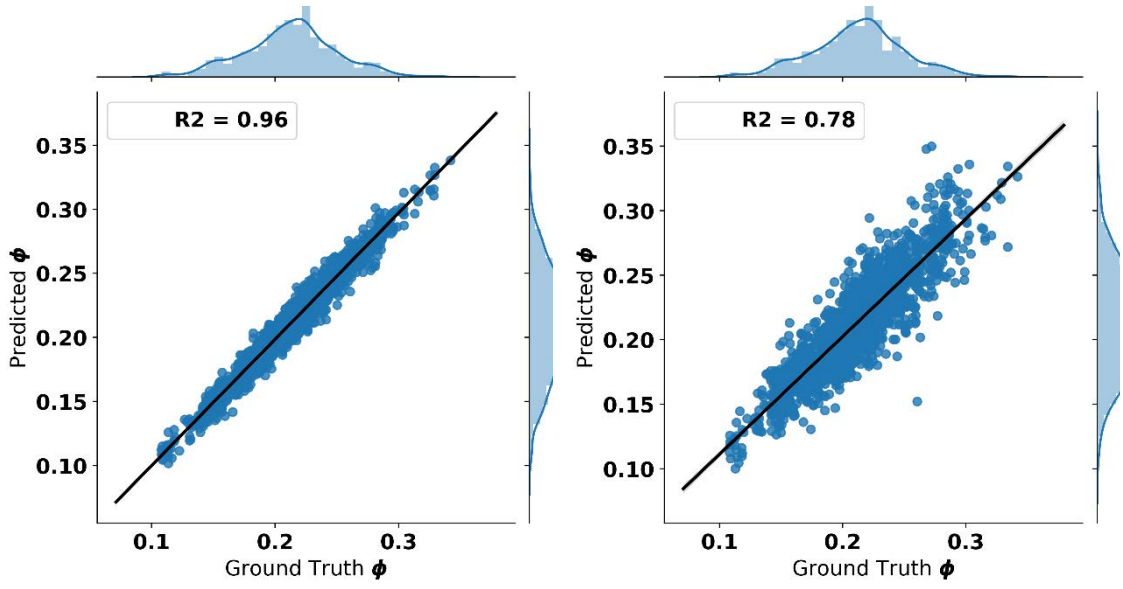

(a) (b)

Figure 3-8: The CNN predictions of porosity from (a) binary and (b) greyscale images are plotted against actual labels.

3.4.2 Specific Surface Area

Predictions of specific surface area from binary and greyscale images are plotted against the dataset labels in Figure 3-9. The average relative error percentage from binary images predictions is 3.9%, and the score of the R-squared metric is 0.92. Whereas the relative error percentage for predicting specific surface area from greyscale images is less than 5.8% with an R-squared score of 0.79.

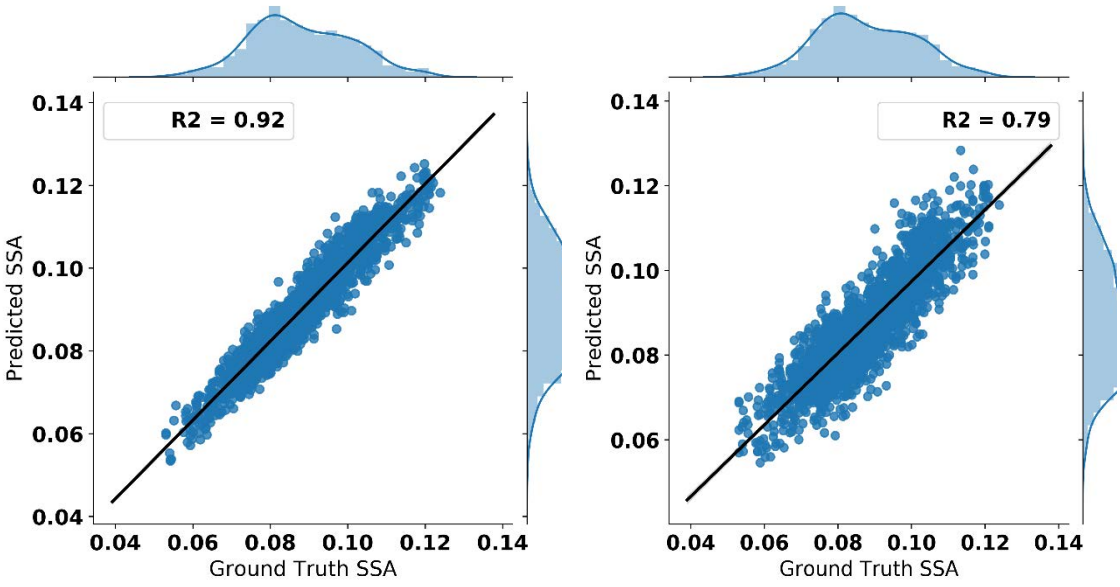

(a) (b)

Figure 3-9: The CNN predictions of specific surface area from (a) binary and (b) greyscale images are plotted against actual labels.

3.4.3 Average Pore Size

CNN estimation of average pore size is shown in Figure 3-10. The average relative error percentages for average Pore Size are 6% and 6.7% for binary and greyscale images, respectively. As the average Pore Size is computed from the pore network extraction and not directly from images, our CNN model develops an indirect intuition

to predict these numbers from binary\greyscale images with an insignificant trade-off in accuracy.

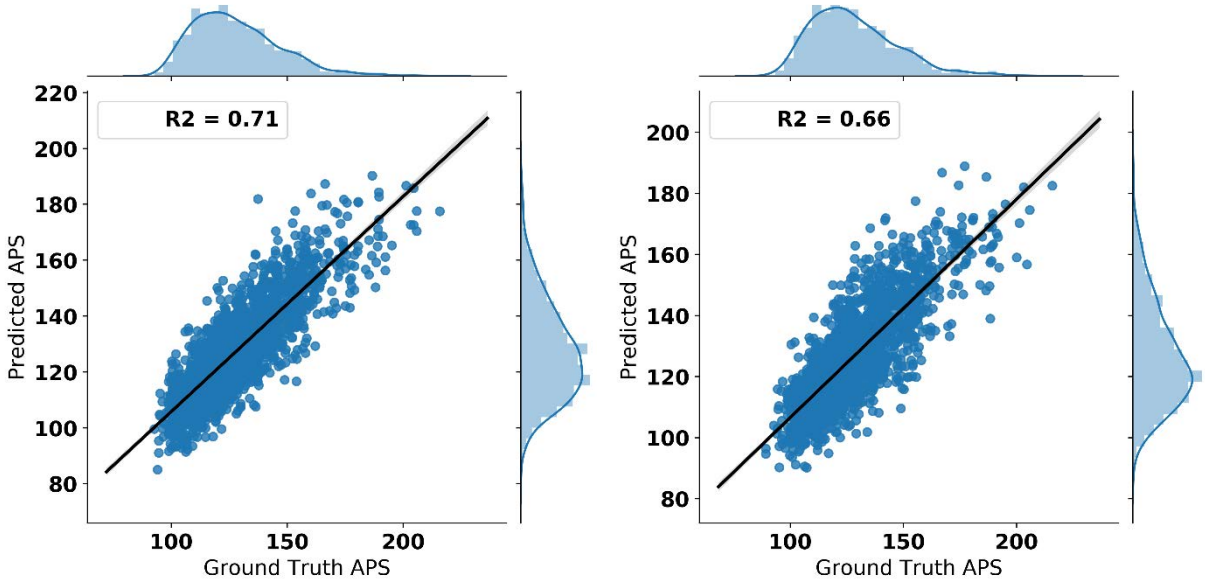

(a) (b)

Figure 3-10: The CNN predictions of average pore size area from (a) binary and (b) greyscale images

Overall, while the CNN using greyscale images can estimate the studied properties with a relative error of less than 7%, estimating the same properties using binary images yields more precise results as expected. Porosity and specific surface area had the most accurate predictions as these labels could be directly extracted from the images. For average pore size, the CNN finds features describing average pore size even though these values are indirectly obtained from the pore network extracted.

3.4.4 Error Analysis, Computation Wall-Time, and CNN Optimization

The relative error of the CNN predictions using both binary/greyscale images is shown as a histogram in Figure 3-11. The bins in the x-axis show the errors calculated from evaluating the model with the testing set. The y-axis shows the probability of

occurrence for each error range. The cumulative probability of obtaining a prediction with a given error margin is plotted. The cumulative probability shows the likelihood of a marginal error in a random prediction from the testing set. The histogram bins for the same relative error are lower for binary images compared to greyscale images across all properties showing a higher accuracy. All histograms are positively skewed showing only just a few predictions with a high margin of error.

The main motivation behind applying the same model on segmented and greyscale images is to show the applicability of CNNs to predict and characterize raw greyscale images accurately, thus implicitly eliminating the need for segmentation computation and possible user bias during segmentation. CNNs can automate this process entirely with the minimum trade-off in accuracy assuming the model's training data is based on expert segmentation annotations/high-quality images. This workflow, however, stills depends on the segmentation step, as it is required to extract ground truth labels and train the model.

The wall time required for training our model varies linearly with the number of epochs required for training and batch size. It takes 22 steps to feed the whole dataset to the model if a batch size of 256 images is used. Each step is processed in around 0.5 s using an Nvidia GPU (model GeForce GTX 1080 Ti). Thus, it takes around 1.5 h to complete the training for 500 epochs.

This chapter focused on providing evidence that machine learning can be utilized as a tool for rock characterization in an end-to-end manner. The user in this case is expected to provide only the tomographic images from which CNN can rapidly estimate several physical properties about the rock of interest. The performance of neural models is known to be sometimes sensitive to the choice of hyper-parameters.

It is possible to perform an exhaustive automatic grid search. However, we leave this as a direction for future work.

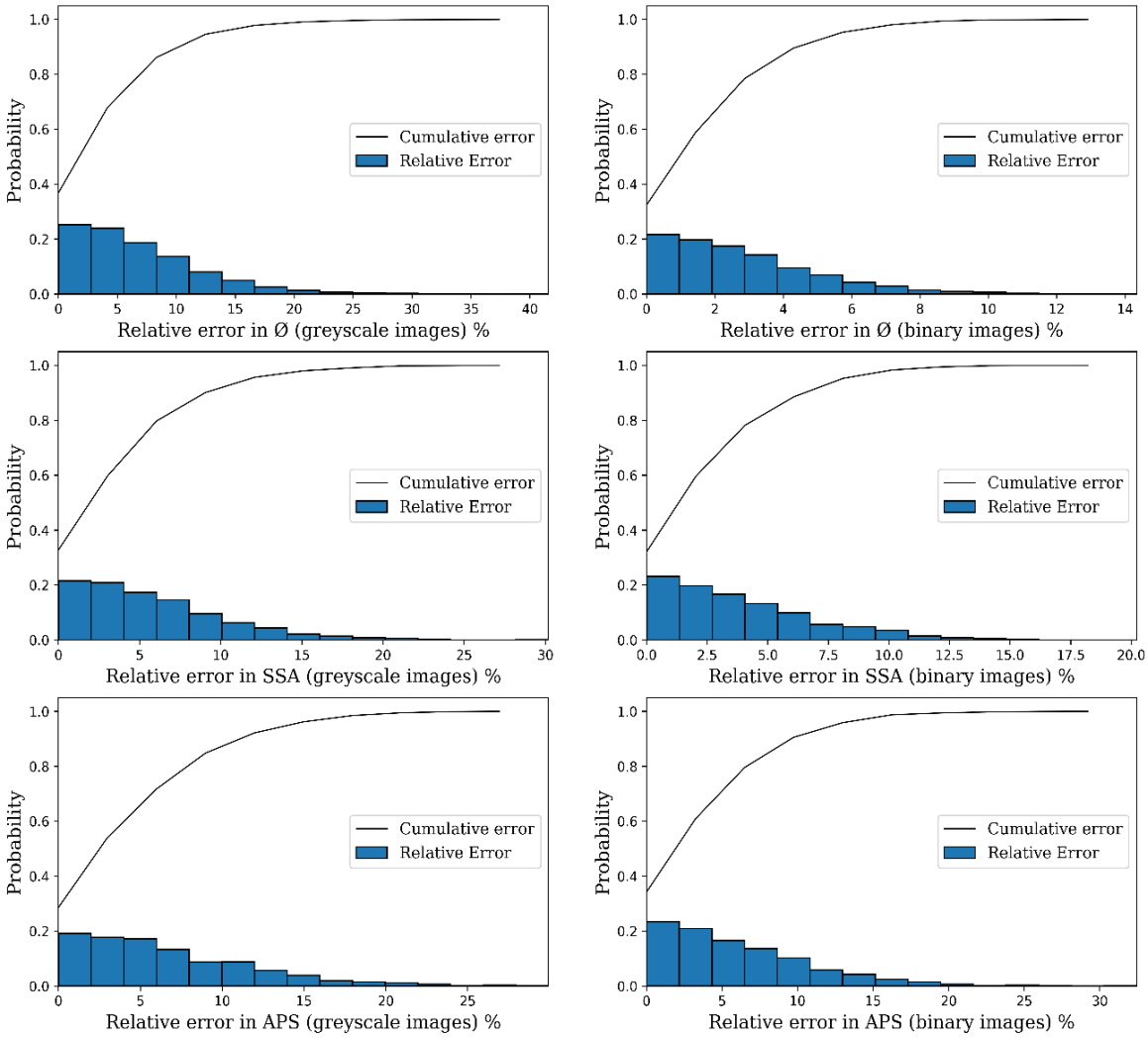

Figure 3-11: the probability of getting a relative error is shown as a histogram, and the cumulative probability of relative error for porosity (Ø), Specific Surface Area (SSA), and Average pore size (APS) and (SSA).

3.5 Conclusion

A framework based on CNNs for rapid estimation of porous media properties from raw micro-CT images is presented. An image dataset (consisting of 5262 images for training and 2000 for testing) capturing different regions of three different sandstone

tomograms is prepared. Porosity, specific surface area, and average pore size of each image are calculated. The CNN is trained using micro-CT images and their corresponding labels (computed properties) to predict physical properties. The results based on the testing images show the average relative error between the ground truth labels and CNN predictions from binary images are 2.7% for porosity, 5.8% for specific surface area, and 6% for average pore size. A lower accuracy was achieved when the model is trained with greyscale images with an average relative error of less than 6.3% for porosity, 5.8% for specific surface area, and 6.7% for average pore size. This work is a first step in designing a framework for characterizing porous media using machine learning using grey-scale images. Yet, this workflow still depends on routine processes such as the segmentation process. A further enhancement to our proposed model can be incorporated to unleash the full potential of DL methods in DRA. Future work will focus on using machine learning for segmenting and predicting several computationally expensive physical properties, especially those directly related to pore-space geometry such as permeability, from three-dimensional images.

4 Flow-Based Characterization of Digital Rock Images Using Deep Learning

Authors: Naif J. Alqahtani, Traiwit Chung, Ying Da Wang, Ryan T. Armstrong, Pawel Swietojanski & Peyman Mostaghimi

School of Minerals and Energy Resources Engineering, The University of New South Wales, Sydney, Australia

The contents of this chapter are from a research paper titled "Flow-Based Characterization of Digital Rock Images Using Deep Learning" published in the Society of Petroleum Engineers Journal (2021). This chapter answers the third and fourth questions of the thesis: What accuracy margins are expected when applying 3D residual network architectures for estimating permeability directly from volumetric images of sandstones and carbonates rocks? Can pore space representation or network architecture improve DL models' performance and regression accuracy?

This chapter expands on this previous work by demonstrating how DL techniques can characterize more complex physical properties such as the intrinsic permeability in 3D space. Advanced residual networks are used as regression tools for achieving this task. The analysis is performed using a diverse dataset consisting of 7 sandstone rocks and 2 carbonate rocks using 3D X-ray images as input as opposed to 2D sandstone used in Chapter 3. The objective of the chapter is to illustrate the scalability, automation, and potential of Deep Learning methods (DL) in predictive modeling of geometry-dependent properties.

Abstract

X-ray imaging of porous media has revolutionized the interpretation of various microscale phenomena in subsurface systems. The volumetric images acquired from this technology, known as digital rocks (DR), make a suitable candidate for machine learning and computer vision applications. The current routine DR frameworks involving image processing and modeling are susceptible to user bias and expensive computation requirements, especially for large domains. In comparison, the inference with trained machine learning models can be significantly cheaper and computationally faster. Here we apply two popular convolutional neural networks (CNNs) architectures [residual networks (ResNet and ResNext)] to learn the geometry of the pore space in 3D porous media images in a supervised learning scheme for flow-based characterization. The virtual permeability of the images to train the models is computed through a numerical simulation solver. Multiple residual network variants are then trained to predict the continuous permeability value (regression). Our findings demonstrate the suitability of such networks to characterize volume images without having to resort to further ad-hoc and complex model adjustments. We show that training with a richer representation of pore space improves the overall performance. We also compare the performance of the models statistically based on multiple metrics to assess the accuracy of the regression. The model inference of permeability from an unseen sandstone sample is executed on a standard workstation in less than 120 ms/sample and shows a score of 0.87 using explained variance score (EVS) metric, a mean absolute error (MAE) of 0.040 darcies, and 18.9% relative error in predicting the value of permeability compared to values acquired through simulation. Similar metrics are obtained when training with carbonate rock images. The training wall-time and hyperparameters setting of the model are

discussed. The findings of this study demonstrate the significant potential of machine learning for accurate DRA and rock typing while leveraging automation and scalability.

Keywords: digital rock, porous media, deep learning, permeability, neural network

4.1 Introduction

Determination of permeability of porous media is one of the key practical interests in assessing subsurface reservoirs. The quantification of geomaterials permeability mathematically is not straightforward because permeability depends on the heterogeneity and complexity of such material's microstructure [297]. Many studies showed that absolute permeability is related to other petrophysical properties such as porosity, pore geometry, connectivity, and tortuosity [119, 297-299]. However, there is no direct correlation for estimating the permeability of porous media accurately without solving for flow at the microscale [48, 126, 300]. With the emergence of high-resolution 3D imaging, an accurate geometry of microscale pores in earth materials, also known as Digital Rocks (DR), can be reliably obtained at a few micrometers or even submicrometer resolution [1, 301]. Such detailed data gives unparalleled knowledge for predicting macroscopic physical properties from the microstructural morphology of the rock using numerical simulations [302].

Modeling flow and transport at the pore scale involve solving governing fluid flow equations such as conservation of mass and momentum [212]. The past two decades showed extraordinary advancement in numerical modeling methods of fluid flow in porous media. These methods can be classified into direct modeling methods and pore network modeling methods. Lattice Boltzmann methods are well-known to be one the widely used methods for computing flow directly on reconstructed pore-scale images [126, 148, 255, 303, 304]. Other direct modeling methods involve medium discretization to solve the Naiver-Stokes equation or Stokes equation for creeping flow [48, 305], or to solve elliptic flow equations [150]. Still, there are several potential drawbacks to direct

modeling methods. Solving numerical simulation directly is often time-consuming and requires high computational capacity and extensive memory allocation [145]. Pore network modeling has been considered as an appealing alternative for direct numerical simulation [138, 306]. The reason is that pore network modeling requires less computing capacity due to the simplified pore-space representation during reconstruction. An accurate simulation of fluid flow using pore network models requires a suitable representation that captures the essential morphological details of the pore space. However, most of the current models rely on assumptions that simplify the geometry of the rock and might be vague when defining what is considered pores or pore throat.

Following many breakthroughs in a variety of computer vision tasks in recent years, Deep Learning (DL) has become a popular research area. DL architectures have overwhelmingly surpassed the performance of the classic state-of-the-art models in computer vision including but not limited to: image classification [307, 308], object detection [309, 310], and semantic segmentation [311, 312]. Subsequently, there has been a general interest in deploying DL on various digital inputs representing porous media. In particular, deep neural network architectures have been applied for DR image pre-processing and modeling; such applications include image resolution enhancement (Super Resolution) [199, 228, 229], image segmentation [23, 25, 313, 314], generating porous media [203] and predictive modeling of physical properties [206, 315-317].

Convolutional Neural Networks (CNNs) [185] make the backbone of typical DL models. Such a model consists of a sequence of non-linear transformations implemented as convolutional layers (i.e., layers with an efficient weight sharing mechanism that allows reusing the same features across various spatial locations in an image). Depending on

the task, the output of a CNN can model a categorical distribution over a set of mutually exclusive classes (classification) or estimate some continuous values (regression) [318, 319]. The model parameters are optimized such it minimizes some loss functions, which for regression problems is often defined as Least Square Error (L2), i.e., the measure of the difference between current model predictions and desired ground truth target predictions. A brief introduction for predicting several porous media properties using CNNs is given in [315]. For further details about DL in general, we refer readers to [21, 28]. With the advancement in computational capabilities and a better understanding of learning dynamics behind such models, the architecture of CNNs became deeper, allowing to discover more abstract features. Many architecture adjustments for boosting the performance of deeper learning models made significant improvements to ordinary CNNs performance including Inception by [320], VGG-16 by [308], and Residual Networks by [321]. CNNs can work with arbitrary spatial dimensions, including volumetric 3D images by using 3D kernels [188].

During the last few years, there have been efforts directed toward deploying machine learning as regression models for predicting porous media physical properties. Many of these efforts showed CNN among the best-performing models. Some of the previous efforts are listed in Table 4-1. While many of these studies introduced new ideas, frameworks, and important findings, there is still a general lack of understanding of how accurate and reliable the predictions can become. The performance of DL models is mainly subjective to the complexity of data (morphology, heterogeneity, etc.), the size of the dataset available for training, and the architecture. We find that the majority of studies in Table 4-1 have been trained or tested on one or two samples if not

synthetically generated images are used. This may not reflect performance on more heterogeneous rocks. Also, the architectures of all models in Table 4-1 are relatively shallow (typically one to eight convolutional layers) which might not unlock the full potential of DL models if recent advancements of deeper state-of-the-art architecture are considered.

In our study, our main contribution focuses on applying full-scale experimentation through training and testing deeper architectures (compared to previous efforts) for estimating permeability on a diverse dataset consisting of (7 sandstone rocks and 2 carbonate rocks). The range of permeabilities studied in the datasets extends over more than 3 orders of magnitude. To the best of our knowledge, this is the largest dataset (with >29K 3D geometry) presented for training DL models in the digital rock technology literature. The training experiments utilize 3D versions of Residual Networks (ResNet) [321] and ResNext [322] to estimate the geometry of porous media for flow-based characterization. The target permeability of three-dimensional porous media is computed through a geometrical finite volume solver [150]. We tested several variants of ResNet and ResNext with different depths to study the performance gains from deeper networks. We also used conductivity maps instead of binary images as an input to represent the pore space for training where we anticipate performance gains. We statically compare the obtained result through four different regression metrics, including mean relative error. We test the performance of the trained models with an unseen testing sandstone, in which the results are shown to generalize well overall. Finally, we train the best-performing model on a carbonate data set, in which the results are shown to be in a similar ballpark to the sandstone data set.

Table 4-1: A summary of previous efforts on estimating porous media physical properties using Convolutional Neural Networks

Research Paper	Type of Data	Training image size \ size of the dataset	Training and Testing Split	CNN Architecture	Accuracy Metrics	Summary of reported accuracy metrics on the testing dataset	Main Findings\Remarks
(Hong and Liu, 2020) [323]	Training: Coconino sandstone Testing: Bentheim sandstone	100^3 \ 3,215 samples	98% to 2%	3D CNN 3 Conv. layers	R^2 –coefficient of determination RMSE– root mean squared error standard deviation	Testing: mean R^2: 0.866 - mean RMSE: 832 mD External sample Benthim sandstone: mean R^2: 0.694 - mean RMSE: 2673 mD	3D CNNs show a relatively good fit for subvolumes obtained from same rock. Accuracy on external samples is not optimal
(Kamrava et al., 2020) [324]	Training: Berea sandstone Testing: Fontainebleau sandstone	200^3 \ 510 sandstone samples + 400 synthetically generated samples	Not mentioned	3D CNN number of layers is not mentioned	R^2 -Coefficient of determination	Berea: R^2 -0.91 Fontainebleau: R2 -0.90	3D CNNs can learn morphology and link it to permeability
(Sudakov et al., 2019) [325]	One Berea sandstone	100^3 \ 9261 samples	90% to 10%	Different ML Methods 2D CNN - 10 Conv. Layers 3D CNN - 4 Conv. Layers	Average Absolute error normalize by the spread of 1st and 99th percentile of permeability values	3D CNN: average absolute error of 3.37%	3D CNNs are superior to other ML methods Accuracy metrics do not include CNN prediction outliers
(Tembely et al., 2020) [326]	Training: one sandstone and one carbonate	Sandstone:(152×152×175) 400 samples Carbonate: (100×100×160) 759 samples	70% to 30%	Different ML methods 3D CNN - 2 Conv. Layers	R^2 -Coefficient of determination	3D CNN: R^2 -0.85 Physics-informed CNN: R^2 -0.91 (adding porosity and formation factor to the fully connected layer)	Different ML methods are tested CNN has lower accuracy compared to other algorithms perhaps due to training dataset size
(Tian et al., 2020a) [327]	3D synthetically generated images	4500 samples	80% to 20%	3D Conv. network: Three networks are tested: 2-4 Conv. Layers	R^2 -Coefficient of determination RMSE MAE	R^2 >0.996 MAE: 0.017 Darcy RMSE: 0.03 Darcy	Near perfect accuracy obtained on synthetic 3D geometries
(Tian et al., 2020b) [328]	3D synthetically generated images	1000 samples	70% to 30%	Genetic Algorithm and Artificial Neural Network	R^2 -Coefficient of determination	R^2>0.99 for all different configurations tested	Near perfect accuracy obtained using synthetic 3D geometries
(Wu et al., 2018) [329]	2D synthetically generated images	Three cases: 980 samples, 1960 samples, 490 samples	3 cases: (98% to 2%) (99% to 1%) (91% to 9%)	2D CNN: 2 Conv. Layers	R^2 -Coefficient of determination MSE	R^2-0.86 , 0.87, -0.714 MSE-0.0008,0.001076,0.001553	Adding porosity and surface area to fully connected layer increase performance

4.2 Materials and Image Processing

Two datasets for training are used. The sandstone dataset comprises of six different sandstone images. The details of all images are shown in Table 4-2. A slightly smaller dataset is created for estimation of permeability of carbonates shown in Table 4-3.

DL models trained using 3D images are constrained by the RAM of the graphics processing unit (GPU) available for training which is mainly dictated by the model size (how many parameters) and the input image size. The computational and memory requirement of 3D network architectures grows cubically with input resolution\domain size [330]. For example, training with domain sizes of 64^3,$128^{3,}$ and 256^3 would theoretically require 5,18 and 80 Gigabytes of RAM for a given model size. Thus, training considerably deep networks with volumes bigger than 100^3 exceed most of current GPU memory specifications. Volumetric image sizes less than 100^3 have been reported in porous media literature to train 3D deep networks [200, 206, 209].

To overcome limitations imposed by the GPU memory and maximize the field of view for the input images, we downsample our images so they can fit in the GPU memory. All input images are downsampled by a factor (N) in a tolerant way that has a minimal effect on the computed permeability and the geometry of the image. In Figure 4-1, a 2D image of Berea sandstone before and after downsampling is shown. This downsampling factor is determined based on the number of pore voxels representing local pore space. So, the pore size distribution of original images is computed based on the local pore diameter (Figure 4-2). The downsampling replaces resolved pore space greater than (N) by at least one voxel in the downsampled image. We choose N to preserve at least 95% of the pore space (the area under the curve shown in Figure 4-2).

Table 4-2: Sandstone samples used in the dataset.

Name	Resolution (μm)	Porosity	Size*	Downsampling factor	Number of subvolumes	References\ imaging facility
Bentheimer sandstone	4.9	0.24	891×891×1440	2x	3240	[331]
Berea sandstone	4.6	0.18	925×925×1200	2x	2160	
Leopard sandstone	3.5	0.14	1265×1265×1800	3x	1836	
Navajo sandstone	1.7	0.14	1265×1265×1800	3x	4800	Argonne National Laboratory
Brown sandstone	1.7	0.13	891×891×2000	3x	3648	
Glidehauser sandstone	4.4	0.20	893×897×566	3x	240	
Doddington sandstone**	2.7	0.20	1000×1000×1000	5x	124	Imperial College London
Total					16048	

**The size of the sandstone images shown is before cropping and downsampling in the x, y, and z dimensions.*

***Doddington sandstone is only used for testing the models.*

The images are downsampled by a factor of (N) by subdividing the original image of grid size (X, Y, Z) into image size $(\frac{X}{N}, \frac{Y}{N}, \frac{Z}{N})$ by assigning the coarser grid cells the statistical 'mode' of the occupying phases in each grid cell size (N^3). To ensure the downsampling has minimal effect on permeability values, the permeability before and after downsampling is measured for all samples and the difference is found to be less than 2%. After downsampling, all the models are trained with intersecting subvolumes of size 64^3 voxels with a shift of 32 voxels as the striding distance.

Table 4-3: Carbonate samples used to create the carbonate dataset.

Name	Resolution (μm)	Porosity	Size*	Downsampling factor	Number of subvolumes	References\ imaging facility
Indiana limestone	5.3	0.10	650x650x1480	2x	7995	University of New South Wales -Tyree X-ray
Middle Eastern carbonate	5.3	0.23	1212x1212x1800	2x	5762	
Total					13721	

**The size of the carbonate images shown is before cropping and downsampling in the x, y, and z dimensions.*

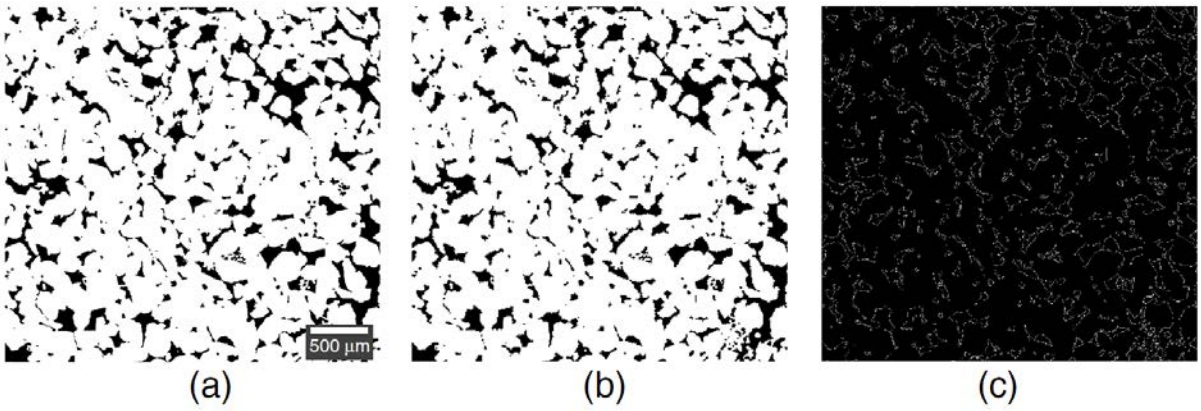

Figure 4-1: Slices of the Berea sandstone (A) before downsampling of size (634,634) and (B) after downsampling of size (317,317) downsampled by a factor of 2. Grains are in white and the pore space is in black. (C) Difference image between A & B, showing slight differences at the solid-pore boundaries with no major connectivity loss (B is resampled to the original size of A for this comparison).

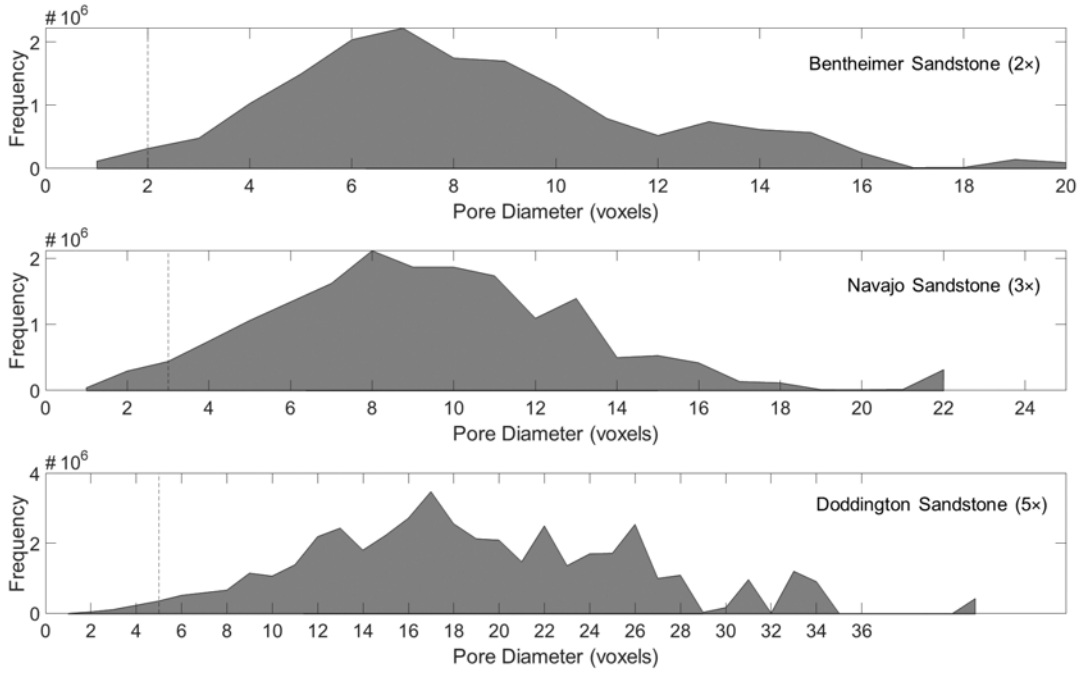

Figure 4-2: The local pore size diameter (voxels) is computed to decide a downsampling factor that has a minimum effect on the resampled image. The downsampled image must have more than (>95%) of the original pore space preserved.

4.3 Methods

4.3.1 Permeability Computation

The permeability of all samples is computed using the pore-scale finite volume solver (PFVS) [150]. This method relates pore voxels' conductivity to the permeability computed from an image. A conductivity value is assigned to each pore voxel based on the distance of the pore voxel from the wall and the size of the local flow channel to which the pore voxel belongs to. An illustration of a conductivity map (represented as a $d_{\max}$ domain using Equation (4-1)) computed for a subvolume of Doddington sandstone is shown in Figure 4-3.

The conductivity is computed in Equation (4-1) using a weighting function that represents the conductivity of the pore voxel based on its distance from the solid wall and the size of a local flow channel to which the pore voxel belongs [49, 150, 151]:

$$\boldsymbol{w = \frac{R^2}{8u}(2d_{max}d - d^2)} \qquad \textbf{(4-1)}$$

where R is the resolution of the image per voxel size (m), u fluid viscosity (Pa. s), d denotes the digital equivalent of radial distance from the inner wall (voxel) and d_{max} is the digital equivalent of the maximum inscribed radius of the local channel (voxel). To obtain the local conductivity of the pore voxels, the Euclidean distance transform of the segmented image is portioned based on the maximum radius of the local flow channel. The algorithm for computing $d\ and\ d_{max}$ is described in detail in [150].

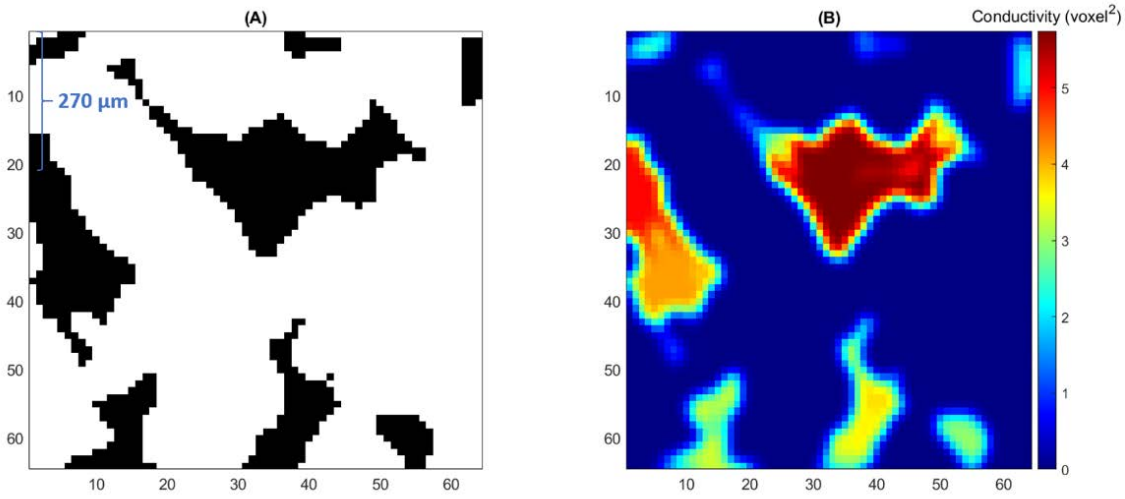

Figure 4-3: (a) Slice of a binary subvolume of Doddington sandstone of size 64^3 and (b) the d_{max} domain (see Equation (4-1)) of the same image. Warmer regions of d_{max} correlate with higher voxel conductivity. Both subvolumes are used for training the models in separate experiments. Image axes show the number of voxels.

PFVS has been tested against the Stokes solver in various rock samples. The permeabilities estimated are within 11% compared to the permeability obtained using the Stokes solver [150]. However, PFVS is chosen over classic simulation methods because of its computational efficiency as a large number of simulations are required to train CNNs [49]. The PFVS computation time that scales with the domain size can be described by a power-law relationship with an exponent of 1.16 (or 80% lower compared to Stokes solver).

For permeability computations, we assume a unified voxel resolution of 4 micrometers for all geometries. The permeability can be rescaled/computed with the desired resolution if the spatial resolution for a given geometry of porous media is known using Equation (4-2):

$$\boldsymbol{K_{Actual}} = \left(\frac{\boldsymbol{R^2_{Actual}}}{\boldsymbol{R^2_{Network}}}\right) \times \boldsymbol{K_{Network}} \qquad (4\text{-}2)$$

where K_{Actual} and $K_{Network}$ are the actual and network estimation permeabilities. R_{Actual} and $R_{Network}$ are the actual image resolution and the assumed imaged resolution. During simulations, we obtain both the permeability value and the conductivity of pore voxels as a 3D map of each subvolume. We train the models separately using the binary images and the conductivity maps shown in Figure 4-3. Based on the preliminary training experiments, we find the minimal preprocessing step of removing all unconnected pore voxels not contributing to the flow before training improves network convergence and accelerates the learning process. We augment our dataset by computing the permeability in the X, Y, and Z directions, which increases the dataset size by a factor of 3.

4.3.2 Networks Architecture

In this study, a special architecture of CNNs called Deep Residual Networks, proposed by [321] is trained for permeability estimation. Residual Network (ResNet) and its variants have been used for various images related problems such as image segmentation and classification, and object detection to mention a few [332, 333]. They have been the core architectures for the best-performing models on large datasets such as ImageNet (www.image-net.org) because of their powerful feature representation ability. ResNets incorporate blocks of skip (or residual) connections between some nonsucceeding layers (compare with Figure 4-4). This copies the signal at the arbitrary layer and passes it "as is" toward the following block. Residual blocks improve training dynamics in the model and allow to efficiently estimate very deep models (i.e., dozens of layers).

The network architectures used in this study are similar to the ones described in [334] for action recognition in videos, except we modify it to use with volumetric images as inputs. In this work, we are also concerned with regression tasks, thus using the linear output layer. The configuration of the residual blocks for the architectures used in this work is shown in Figure 4-4. In Table 4-4, we show the full network architectures for regression. We opt to experiment the performance of different architectures and depths as the literature on regression networks is not vast compared to other tasks such as classification. Hence, the accuracy gains of using a deeper network can be quantified.

The basic ResNet block contains two convolutional layers each followed by batch normalization and a Rectified Linear Unit (ReLU). The signature skip connections of Residual networks connect the top of the basic block to just before the ReLU. Skip

connections of Type (A) described in [321] are used in Basic blocks. The bottleneck block design has three convolutional layers followed by batch normalization and ReLU. Identity connections in bottleneck architecture are all of type (A) except where the dimensions of the tensors are changed (see Table 4-4) we use Type (B) skip connections [321]. The main difference between the two-block designs is the efficiency of computation. The bottleneck design is more economical when building deeper networks as reported when these designs were trained using different datasets [321].

Table 4-4: Network Architectures. (F) corresponds to the number of feature maps in the residual block as shown in Figure 4-4. (N) is the number of blocks for a given layer. Max-pooling with a kernel size of 3×3×3 and stride of 2 before Conv2 is applied for downsampling. Every layer (Conv_x) is followed by batch normalization [287] and rectified linear unit activation [288]. Spatial downsampling is applied at layers (Conv3, Conv4, and Conv5) with a stride of 2.

Model		**ResNet-34**	**ResNet- [50,101,152]**	**ResNeXt-50**
Block type		Basic	Bottleneck	ResNext
Conv_1		conv, k=7×7×7, F=64, stride=1		
Conv_2	F	64	64	64
	N	3	3	3
Conv_3	F	128	128	128
	N	4	[4,4,8]	4
Conv_4	F	256	256	256
	N	6	[6,23,36]	6
Conv_5	F	512	512	512
	N	3	3	3
Average Pooling	global average pooling			
Top Layers	FC layer-1 (1024), FC layer-2 (1)			

4.3.3 Training Settings, System Specification, Hyperparameters, and Metrics

This section describes the training and evaluation protocol, experimental settings, the choice of hyperparameters for training the networks, and the metrics used to evaluate the models. Table 4-5 reports the hyperparameters used to train each network variant.

We train all the models using a DL Pytorch [335] toolkit using a single RTX 2080 Nvidia GPU. This GPU has eight Gigabytes of RAM, installed on a PC with an Intel i7-8700 (a 3.20 GHz with six cores) CPU processor and 64 Gigabytes DDR4 RAM.

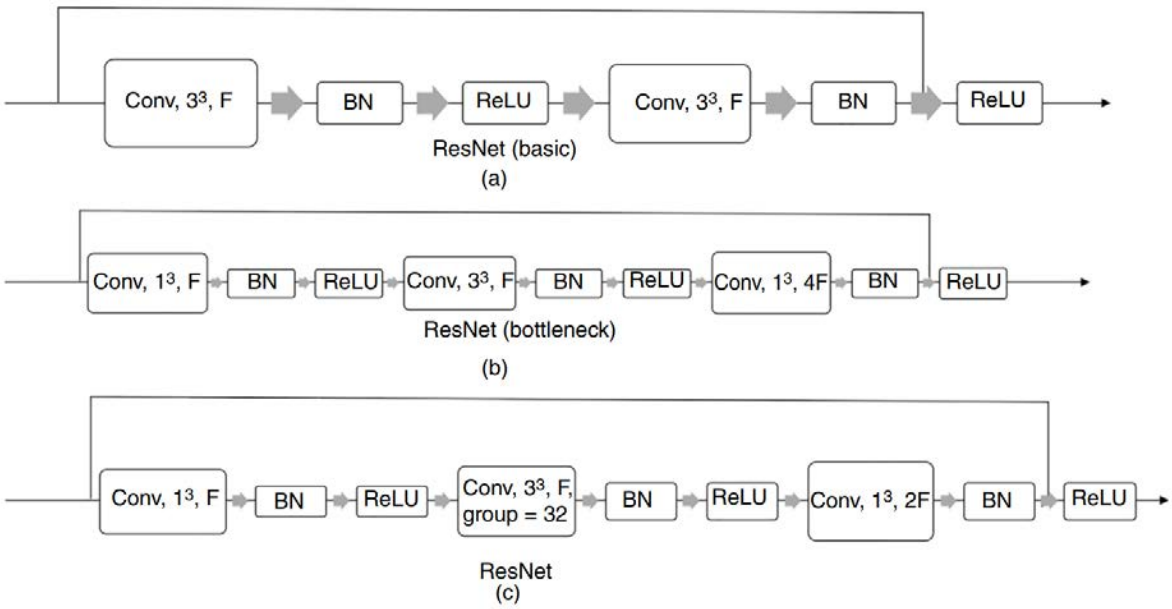

Figure 4-4: Residual blocks of architectures (a) ResNet (basic), (b) ResNet(bottleneck) and (c) ResNext. (Conv, k^3, F) refers to the kernel size (k) and the number of feature maps (F) of the convolution operation (group) refers to the number of groups of in convolutions or (cardinality) as described in the original paper [322]. BN refers to batch normalization [287] and ReLU refers to the rectified linear unit activation [288].

Early stopping of training with a patience of 15 epochs (when the validation error does not improve for 15 epochs) is applied to avoid overfitting [336]. The weights of the models are saved whenever the validation error decreases. Our

training/validation/testing splits of the datasets are 70% /15% / 15%, respectively, not including the Doddington sandstone samples. The validation dataset is utilized as a separate subset to assess the network performance while training for tuning hyperparameters (e.g. learning rate and weight decay).

Table 4-5: Hyperparameters settings for training the models.

Hyperparameter	Resnet [34,50,101,152]	ResNext-50
Batch Size	[8,8,6,4]	8
Optimizer	Adam [295]	
Learning rate	1×10^{-5}	
Weight Decay	1×10^{-4}	
Loss Function	Mean Absolute Error (MAE)	

During training, we monitor four metrics to assess the model accuracy: Explained Variance Score (EVS), Mean Absolute Error (MAE), Mean Squared Error (MSE), and Mean Absolute Relative Error (MARE). MAE and MSE are very common criteria for regression problem monitoring and detecting outliers [337]. EVS is a statistical measure that estimates the proportion of which a model accounts for the variation of a given dataset. The highest possible score for EVS is 1.0, lower values correspond to worse performance. Mean relative error estimates the average relative error to the ground truth values for all samples. In Table 4-6, we show the mathematical formula for computing each metric. We use A_j for the actual value of the j-th sample, P for the predicted value, Var for the variance and n for the number of samples in each dataset.

Table 4-6: Metrics for assessing the accuracy of regression.

Metric	Metric Formula
EVS - Explained Variance Score	$1 - \frac{Var\ (A_j - P_j)}{Var\ (A_j)}$
MAE – Mean Absolute Error	$\frac{1}{n}\sum_{j=1}^{n}\left\|(A_j - P_j)\right\|$
MSE – Mean Squared Error	$\frac{1}{n}\sum_{j=1}^{n}(A_j - P_j)^2$
MARE - Mean Absolute Relative Error	$\frac{1}{n}\sum_{j=1}^{n}\frac{\left\|(A_j - P_j)\right\|}{A_j}$

4.4 Results and Discussion

4.4.1 Binary Images and Conductivity Maps Comparison

We compare the use of binary/segmented images as an input for training against the use of conductivity maps. It is noticed that training with conductivity maps generally yields better performance when benchmarking against two ResNet architectures: ResNet-34 and ResNet-50. The aforementioned evaluation metrics are monitored on a separate validation set during the training experiments and are shown in Figure 4-5. This behavior is expected because the conductivity maps contain a richer representation of

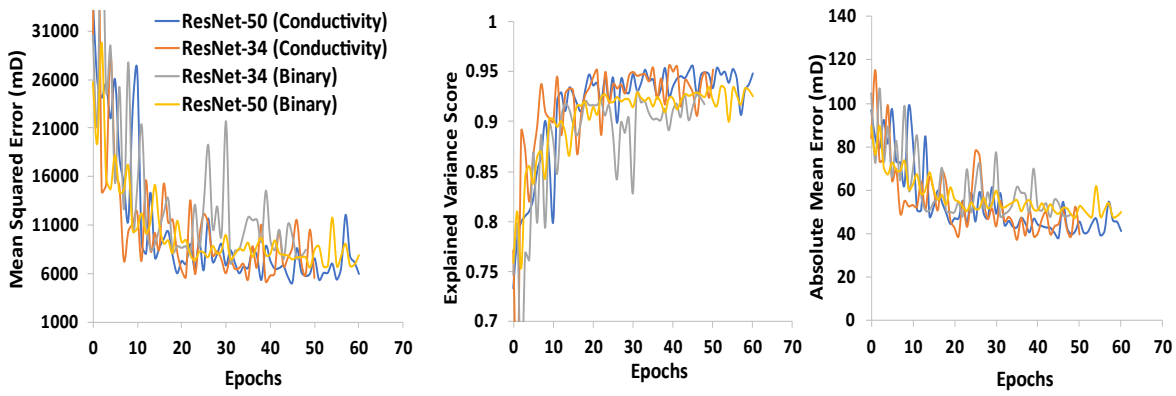

Figure 4-5: Comparison of the performance of ResNet-34 & ResNet-50 when using binary images against conductivity maps

what determines permeability, where not only the morphology is defined, but also the pore voxels connectivity is cast for better permeability estimation. We base all further model experiments in the remainder of the study on the conductivity maps as the input images for training.

4.4.2 Regression Experiments using Residual Networks Variants

In this section, we test several residual network variants for flow estimation. The training settings for all the experiments are shared and reported in Table 4-4 and Table 4-5. Only the model architecture is changed for each run. The regression evaluation metrics for the best model performance using the testing set are reported in Table 4-7. The models achieve very similar performances overall. There are slight gains in accuracy when increasing the depth of the network; however, this is at the expected cost of higher computation requirements (longer training time). In Figure 4-6, the training loss is plotted against the number of epochs. The figure shows the convergence in deeper networks is slower, requiring training for more epochs.

Table 4-7: Residual Network performance on the testing set. Bold results show the best values of each metric obtained during training.

Model	MSE (mD)	EVS	MAE (mD)	MARE	Training Duration (hours)
ResNet-34	5012.9	0.953	25.94	34%	**11**
ResNet-50	**4765.62**	0.961	28.82	28%	17
ResNet-101	4811.55	0.963	28.23	28%	36
ResNet-152	4792.23	**0.964**	**25.88**	**25%**	86
ResNext-50	6992.23	0.943	34.27	34%	26

The actual permeabilities as obtained with numerical simulation are plotted against the ResNet-50 estimation in Figure 4-7. The datasets considered in this study are not equally distributed across the full range of permeabilities but rather skewed to values closer to zero. The existence of a few prediction outliers with relative error exceeding 50% is apparent in some samples. The anticipation of outliers in neural networks regression has been reported in the literature for different regression problems such as age estimation [338, 339] and several methods have been suggested to mitigate it such as the use of robust regression methods [318, 338]. Yet, applying such methods lies beyond the scope of this study. The mean relative error of the best performing model is 25%, in which the highest 10th percentile of relative errors is for samples less than 100 mD of permeability. These errors possibly arise from the complex geometries with narrow pathways that the network mispredict. Also, this is a side effect of using L1 loss which might not be sensitive to relative error considering the backpropagation through which the network weights are updated.

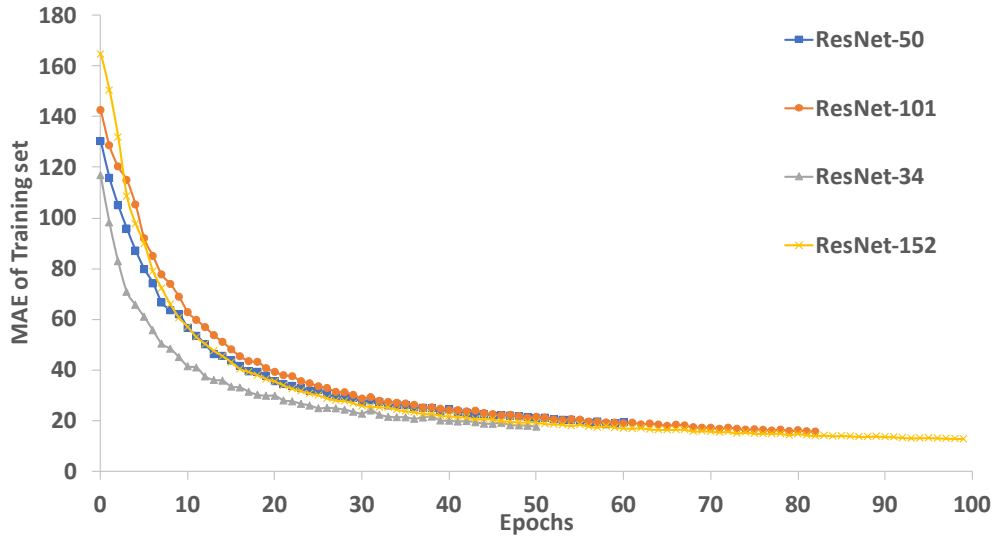

Figure 4-6: Training loss (MAE) plotted against the number of training epochs.

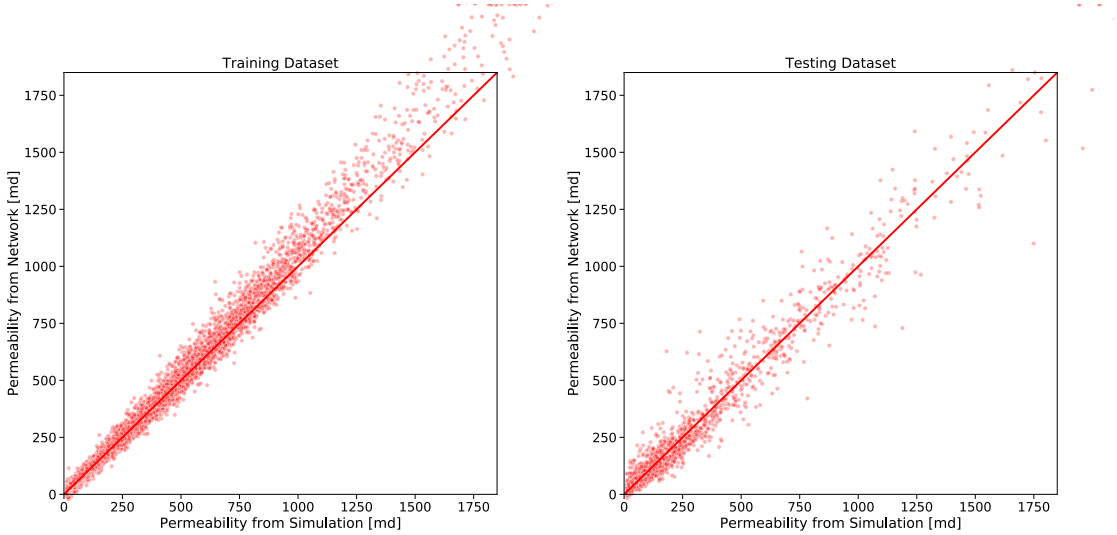

Figure 4-7: Permeability values from the simulation are plotted against the permeability using the network estimation. The determination coefficient (R^2) of the training dataset (left) is 0.984 and the testing dataset (right) is 0.956. The red line is showing the line equation y=x.

4.4.3 Testing with Unseen Sandstone Samples

All testing subvolumes in the previous sections are unseen and have not been used in training but part of the samples was used in training. In this section, the models were tested using a holdout Doddington sandstone that has not been included in the training dataset. In total, 124 subvolumes were tested using the best models' weights (according to validation performance) as obtained during training. Table 8 shows the performance metrics of each model. The models' performances are in a similar ballpark as the results reported on the in-domain testing set with ResNet-152 characterized by the best performance. Figure 4-8 shows the permeability from the simulation plotted against ResNet-152 predictions. The EVS is 0.87, slightly lower (less than 10%) than the average of the testing set. However, the computed prediction errors using MAE and MSE metrics are 18.92 mD and 3072 mD, respectively, which are lower compared to the experiments ran on the testing set by 30%. The MARE for the best model, ResNet-152, is 18.9%. This

relative error reported is not high if compared to indirect pore-scale modeling techniques to compute permeability such as pore network modeling or Laplace solvers [137, 143, 340]. The reported errors in these studies are generally higher than 20%. Also, the inconsistencies between various numerical solvers (such as finite volume method) compared to Lattice Boltzmann methods and Stokes solvers have similar relative errors [174, 341]. The inference time of deep models per sample is four times less than that required to run the simulation used for the same domain size. So, the error trade-off

Table 4-8: models performance tested using an external sandstone.

Model	MSE (mD)	EVS	MAE (mD)	MARE (%)	Inference time per sample (ms)
ResNet-34	3244	0.87	44.3	21.3	61
ResNet-50	3206	0.87	41.8	21.8	70
ResNet-101	3638	0.86	42.5	22	88
ResNet-152	**3072**	**0.87**	**39.10**	**18.9**	105
ResNext-50	4172	0.83	51.02	25.4	**56**

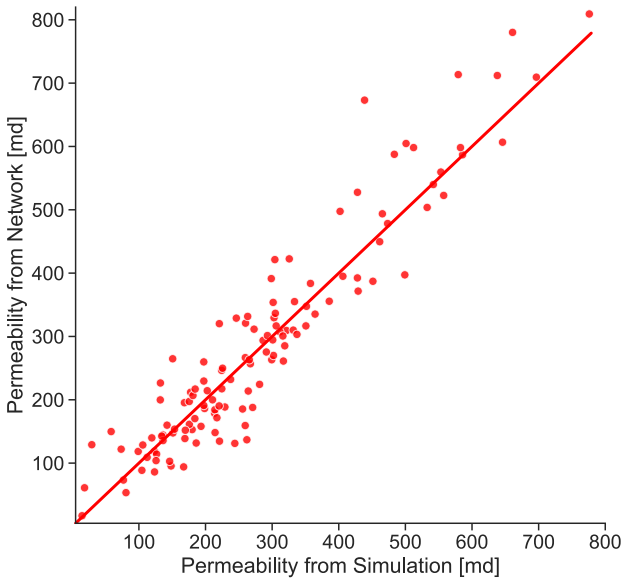

Figure 4-8: Permeability of subvolumes of an unseen sandstone plotted against the ResNet-152 predictions. The determination coefficient (R^2) is 0.86. The red line is the line equation y=x.

4.4.4 Training and Testing on Carbonate Samples

The regression experiment using model Resnet-152 are repeated using the carbonate dataset in which carbonate images are used for training. The results are shown in Figure 4-9. Table 4-9 shows the performance metrics on the testing set where the metrics overall show a similar trend to the results obtained when training using sandstone. However, it was noticed again that the highest top 10^{th} percentile of relative error is from samples with relatively low permeability (<500 mD). The reason is perhaps the complexity of the pore space geometry and the limited connectivity between pore bodies where the network misestimates such bottlenecks. Model regularization and incorporating robust regression techniques for outliers detection should have a significant improvement on such models which is an active research area [338, 342].

The results and error margins when training with more complex geometries of carbonates are comparable with the previous experiments on sandstones. This shows

the capacity of residual networks as models, and their ability to learn complex features considering the different porosity ranges and geometrical features of carbonates. This is another significant advantage over indirect pore-scale modeling in which the performance in general declines with the geometry complexity [137, 340].

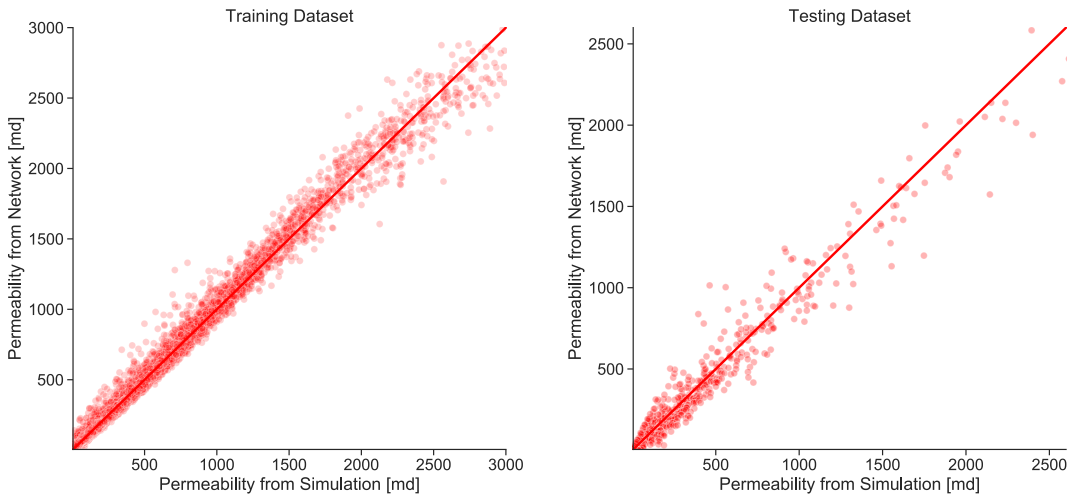

Figure 4-9: Permeability of carbonate subvolumes plotted against ResNet-152 predictions. Determination coefficients (R2) are 0.98 for training and 0.95 for testing. The red line is the line equation y=x.

As the introduction of GPUs facilitated training deeper networks such as the ones presented in this study, computational efficiency remains an important aspect for achieving optimal accuracy. The gains in accuracy through training deeper neural networks may not be significant, considering the training time. ResNet-50 and ResNet-152 achieve very close margins of accuracy with considerably longer training time for the latter. However, considering the inference time for all models taking less than a second and the fact that training is only done once, the gain in accuracy with respect to training time can be justified. The rapid growth of computational resources i.e., GPU computational capacity and using multiple GPUs for training should boost the robustness and generalization of DL models. larger dataset, domain sizes and deeper

models boosting the robustness and the generalization capacity of deep regression models.

Table 4-9: Performance metrics obtained from the testing set when training model ResNet-152 on the carbonate dataset.

Model	MSE (mD)	EVS	MAE (mD)	MARE (%)
ResNet-152	10693	0.95	66.5	26.8

4.5 Conclusion

Applying deep neural networks for estimation of permeability based on 3D images of rocks as an input has shown to produce a comparable result to the values obtained via numerical simulations. Several 3D variants of deep residual networks (ResNet) are trained to estimate the permeability of subvolumes of size 64^3 voxels extracted from larger downsampled volumes. Two datasets are generated from sandstone and carbonate images with a total number of images exceeding 29,000 subvolumes for training and testing. The training experiments are conducted using two forms of inputs: binary images and conductivity maps (where pore voxels are assigned a conductivity value based on Euclidean distance from the closest grain boundaries). Several conclusions have been made from the training experiments. First, training with a richer representation of pore space yields considerably better estimation results. Conductivity maps boost the network performance in estimating the permeability compared to binary images, decreasing the MAE metric by 37.5%. Second, network depth can improve regression accuracy considerably. When the residual network variants are compared, deeper networks performed better compared to shallower ones, at the cost of higher computational cost, e.g., ResNet-152 decreases the MAE metric by 10%

compared to ResNet-50. The evaluation metrics of the best performing model, ResNet-152, are MAE of 25.88 mD, EVS of 0.964 and MARE of 25%. The most promising model was also tested using an unseen Doddington sandstone. The evaluation metrics show a similar trend to results obtained from the original testing set with MAE of 18.92 mD, EVS of 0.87, and MARE of 18.9% for ResNet-152. Finally, the results obtained when training Resnet-152 on more heterogeneous and complex geometries of carbonate images are very similar with MARE of 26.8% and MAE of 66.8 mD. This shows the capacity of DL models to learn more complex geometries without an obvious implication on the estimation accuracy if compared with more classical methods of estimating permeability.

This study serves as a first step toward obtaining a fully automated framework for estimating physical properties from the pore space geometry for which we consider 64^3 subvolumes of various DRs for training. The advancement of computational technology (especially GPUs) will enable training with larger domains and datasets sizes. The focus of future studies will include training with more complex geometries of porous media including fractured media. We also look forward to enhancing the generalization ability of models through combining robust regression methods alongside neural networks and employing ensemble learning.

5 Conclusions and Future Work

This chapter summarizes the main contribution and conclusion of this research and recommends directions for future work.

5.1 Conclusions

This thesis presented frameworks for developing, validating, and integrating DL capabilities to address several limitations in Digital Rock Analysis (DRA) workflows, such as bottlenecks in imaging hardware, processing, and modeling schemes. DRA is a key step in rock and porous media characterization studies, whose applications include estimating hydrocarbon reserves, geomechanics, and CO_2 sequestration. Several implementations of DRA are intended to provide swift and reproducible reservoir rock characterization, including the estimation of permeability and porosity. Yet, they contain shortcomings due to (1) user bias and experience in choosing parameters in processing and modeling, (2) constraints imposed by imaging hardware, such as the tradeoff between resolution and field of view, and (3) high computational cost of traditional image processing and numerical simulation. Our methods overcame these limitations by adopting DL methods to automate the processing and modeling of these rock image analyses. These methods' advantages include reduced human involvement so as to minimize human error (achieved by using end-to-end models), the rapid characterization of porous media through predictive modeling, and adding capabilities to the analysis that cannot be achieved otherwise using traditional imaging hardware.

To achieve our objective and demonstrate the capability of DL methods in rock analysis, the questions stated in the objectives section have been addressed in discrete stages. First, the potential of DL in processing and segmenting carbonate rocks using Convolutional Neural Network (CNN) architecture for super-resolution and multiphase segmentation was explored.

Second, an automated characterization method from 2D X-ray images of sandstone rocks was proposed. Third, another framework was designed to extend the DL capability for 3D flow-based characterization in both sandstone and carbonate rocks. The questions listed in the objectives are addressed as follows:

I. **Is it possible to develop end-to-end DL schemes that can minimize user bias and process low-resolution images to reliably produce high-quality segmented data? If so, how is this improvement reflected in the computed physical properties of the processed medium?**

To alleviate the issues of user bias and imaging hardware constraints, Chapter 2 presented how to obtain super-resolved segmentation of complex carbonate rocks to illustrate the capability of DL in image processing and segmentation. For this purpose, a unique High-Resolution (HR) and Low-Resolution (LR) micro-CT scanned dataset of carbonate rock images was prepared. Using these datasets, two DL frameworks were trained to super-resolved and segment LR images, namely (1) U-Net and U-Resnet in an end-to-end scheme in one network, and (2) obtaining super-resolution and segmentation in two separate networks (EDSR-U-Resent). The segmentation accuracy of the two frameworks was compared with that of classical segmentation methods. The comparison metrics included voxel-wise accuracy, morphological measurements, and flow characteristics. Overall, the results showed improved identification of micro-porosity in carbonate rocks, despite imaging artifacts such as partial volume effects. The results of the segmentation of the network show consistent voxel-wise accuracy and are commensurate with the ground truth segmentation. In addition, and from a morphological perspective, our volume fractions of network segmentation showed better accuracy than does using only LR segmentation from classical methods (e.g., Otsu and watershed segmentation). Furthermore, and to compare the flow characteristics of network segmentation, the DL frameworks showed promising pore network results with better connectivity, pores, and pore-

throat sizes for CNN segmentation than do ground truth methods. Additionally, single- and multi-phase flow simulations of the network show a relatively good match compared to ground truth simulations (see Table 2-4 and Table 2-5). The encouraging results owing to the automated processing and segmentation demonstrated by these DL techniques lead to minimizing user input and bias to the analysis. The results of the DL techniques also show their ability to overcome hardware constraints by allowing for a flexible image domain size selection. For instance, LR images having a large field of view can be obtained and translated via super-resolution to capture the finer details of pore geometry. In this application, we demonstrated how automation using a fit-for-purpose DL techniques is useful in image pre-processing, which is a vital step before characterizing the rock images. However, it should be noted that the use of more advanced CNN structures (e.g., HRNet [343], HRNet-OCR [258], and EfficientNet [259]) and training strategies that use multi-scale context methods [258] should improve the outcome segmentation, resolution, and performance. The use of more accurate methods is further discussed in the recommendation for future work (section 5.2.2).

II. Can CNNs be used as regression tools for predicting the physical properties of porous media directly from 2D segmented micro-CT images? Can raw greyscale images be used?

To characterize the rock images, Chapter 3 described the second stage of integrating DL techniques in rock analysis: a rapid and automated characterization method from 2D X-ray images of sandstone rocks. It served as a proof of concept that DL methods such as CNN can be used to predict geometry-based reservoir properties based on images as input. Traditionally, DRA computes physical rock properties using time-consuming ad-hoc processes (e.g., filtering segmentation, pore network extraction, and flow simulations). These processes often require iteration to pre-process the image, extract the pore network or model flow before computing the properties, which increases the computational and man-hour time to conduct petroleum

studies. To reduce the analysis time, the main objective of this chapter was to show that CNN-based frameworks do not merely segment the rocks, but predict key physical properties using binary and greyscale micro-CT X-ray images as input. By doing so, CNN can reduce the analysis time because of the automation of DL techniques. A dataset consisting of more than 5,000 training and 2,000 testing 2D images was used to conduct the investigation. The predicted properties of the model were the porosity, specific surface area, and average pore size of each image. The model showed promising results, where the relative error to determine these three physical properties was no more than 6% when using binary images and at most 7% when greyscale images were used. This chapter focused on 2D regression analysis on sandstone images only, to predict simple physical properties linked to the pore space geometry.

III. **What accuracy margins are expected when applying 3D residual network architectures for estimating permeability directly from volumetric images of sandstones and carbonates rocks?**

IV. **Can pore space representation or network architecture improve DL models' performance and regression accuracy?**

To expand the previous investigation on other types of rocks and characterize more complex physical properties, Chapter 4 illustrated the third stage, which used residual networks for both sandstone and carbonate rocks using binary 3D images or conductivity maps as input. Historically, fluid flow simulation has been modeled on pore space using computationally demanding techniques to estimate permeability. Similar to DRA ad hoc processes highlighted in Chapter 3, this also adds to the analysis time of rock characterization. Once training is completed, the permeability estimation can be significantly computationally faster. For this purpose, only the CNN feed-forward cycle was used to estimate permeability, leading to less reduced wall-time than those of other flow simulation methods. The best model results showed that permeability can be inferred from an unseen sandstone sample in less than 120 ms, with a

relative error of 18.9%. Similar results were obtained when carbonate rock images were used for training. We also showed that the accuracy of permeability estimation was superior when the input was conductivity maps rather than binary images. In addition, we found that a slight performance gain can be achieved when using deeper networks for the analysis.

Overall, the DL methods we presented demonstrated great potential for accurate digital rock analysis by leveraging automation and scalability on 2D and 3D carbonate and sandstone micro-CT images. Although DL techniques have been previously used to process digital rock images and predict properties from them, they did not attempt to utilize DL for end-to-end processing. They also lacked a comprehensive detailed analysis of regression accuracy or showcasing the generalization capabilities on various rock types (as shown in the introduction of Chapter 4, for example). This thesis advances the current stage of knowledge with the following main contributions: (1) the demonstration of DL techniques in end-to-end image processing by translating LR greyscale images to HR labeled images; (2) the proposal of a scheme to estimate several physical properties from 2D images, including detailed regression and error analysis; and (3) the analysis of a more inclusive dataset suitable to estimate permeability in both sandstone and carbonate rock types using state-of-the-art deep residual networks.

The set of DL techniques presented in this thesis is useful for preliminary estimation of rock properties, especially for immense core analysis projects required at the early planning stages of field development. The prospect of ever-increasing computing power promises even more future improvement in estimation and processing accuracy, which opens the door for a wider deployment of machine learning in digital rock analysis. The technology has the potential not only to reduce the computational time required for the analysis, but to minimize the required manpower to complete routine rock analysis. However, the DL techniques that achieved these results are still in their infancy, and further work is required to improve their applications, particularly for digital rock analysis. Challenges such as inadequate dataset representation, lack

of field and laboratory data, and accuracy loss from soft computing remain and must be considered when using artificial intelligence techniques. Furthermore, other key areas of future work are required to improve the results of this thesis which are discussed in the next section.

Lastly, this thesis presented DL methods for image processing and physical properties regression in chapters 2 and 4, respectively, on 3D digital rock images. Learning from 3D images has many advantages over learning from 2D images, especially for tasks requiring the assessment of connectivity such as permeability estimation. The methods presented applied 3D convolution on voxel grids to extract features relevant to the network's task from the geometry of interest. While this approach showed promising results, other data structures such as graph representation learning [187], and point-cloud methods [344] have been suggested to improve the performance for learning from 3D geometries. Further discussion on this topic is presented in section 5.2.2.

5.2 Recommendations for Future Work

Although the results of this work show promising potential of DL techniques in DRA, key areas of future research would enhance our research output, expand its application, and improve its accuracy. In this thesis, three key specific areas are recommended for future studies including: (1) using laboratory data to benchmark and train the DL models; (2) investigating the use of other DL methods to enhance the accuracy of prediction and improve performance; and (3) extending the use of DL techniques in complex and challenging rock types such as unconventional shale gas or tight sand. These areas are discussed in more detail below.

5.2.1 Using Laboratory Data for Benchmarking and Training DL Models

Unlike most computational paradigms, DL has the ability to learn. In many scientific fields, DL has been shown capable of resolving complex applied problems. For example, DL models have shown great success in detecting early signs of cancer in medical imaging. However, these models were trained on an enormous number of real-life cases and high-quality data. Data

augmentation can help mitigate the lack of data by generating extra instances for DL models to learn from. However, this might not be sufficient for scalable generalization. In fact, many service companies have the sole business objective of image labeling and annotation for machine learning projects.

As for DRA, since the main reference for validating DRA is mainly through laboratory experiments, it is worthwhile creating large laboratory-based datasets for the characterization of porous media and DL training. Although this is partially fulfilled in Chapter 2, where Mercury Intrusion Capillary Pressure was used to calibrate the segmentation of ground truth segmentation, the other chapters used image-based results and numerical simulation as ground truth. For example, Chapter 4 showed that the permeability of various porous media can be estimated using DL with a relative error of 18.9% as compared to numerical simulation. However, the inherited error from the preprocessing or simulation is not fully quantified. Creating datasets where the ground truth of physical properties is obtained through laboratory experiments would increase the value of DL models as characterization tools. Raw micro-CT images can be used as-is for predictive modeling of macroscopic physical properties.

5.2.2 Exploring Other Learning Methods for Accurate Predictive Modeling

The science of DL is still at the early stages of research and implementation in DRA. The first paper that attempted applying a DL application on DRA was published in 2016. Over the past few years, novel DL techniques have been introduced to improve the accuracy of prediction and improve training and testing performance. For instance, Multi-Task Learning (MTL) [345] has recently gained increasing popularity in various applications such as speech recognition [346] and drug discovery. In single learning tasks, one loss function is optimized, such as the absolute error in permeability regression presented in Chapter 4. This focus on one task can lead to overlooking information that helps improve performance. In contrast, in MTL, features extracted

and shared representations across the network to perform tasks have been shown to improve the DL model's ability to generalize on the essential task. In essence, several losses are computed for multiple tasks and are used to optimize the shared layers' parameters, as shown in Figure 5-1. In July 2021, Cao, et al. [347] presented the first effort for applying such methods on DRA. The model architecture proposed is composed of a segmentation network, a feature extraction network, and a physical properties regression network. The model uses parameter sharing, which improves the performance of the network overall. However, this work applies the model on 2D slices of sandstone for the regression of properties, similar to the one presented in Chapter 3. It would be beneficial to apply similar models for estimating physical properties dependent on 3D geometries, such as single and relative permeabilities, which often require numerical simulation to obtain.

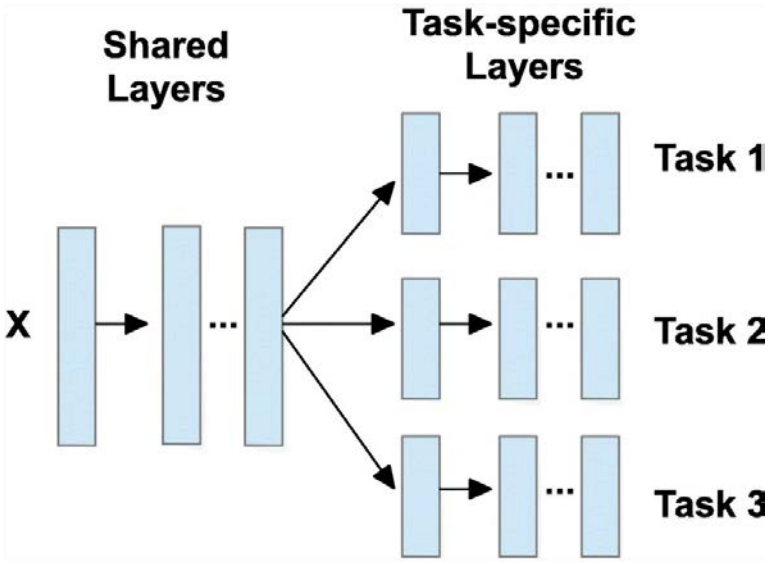

Figure 5-1: A Multi-Task Learning model architecture. Retrieved from Thung and Wee [345].

DL models can be trained with multiple tasks such as segmenting greyscale image input, estimating image-based properties (e.g., porosity and saturation) from the segmented images, and predicting velocity field or tortuosity, which might traditionally require numerical simulation to obtain.

DL models can also be improved by mitigating the memory limitation of modern GPUs when training. The review of DL in DRA presented by Wang, et al. [20] showed that most of the models are trained using mini-batches of subvolumes of around 100^3 voxels in size. This limits the field of view when processing images or predicting petrophysical properties from these batches. However, there are other unexplored DL methods for learning from 3D spaces, that utilize memory-efficient algorithms such as point-cloud learning [344] and octree data structures (3D grid agglomeration) [330, 348]. Both of these methods enable investigating larger volumes and can be used to represent pore space geometry and predict geometry-based properties.

5.2.1 Investigating the Potential of DL Techniques in Unconventional Resources

In recent years, increasing attention has been directed toward unconventional reservoirs such as shales or coalbeds, for their potentially large untapped reserves and the availability of technological means to extract the hydrocarbons from such reserves. Yet, these reservoirs are characterized by tight porosity ranges (often <8%) and ultra-tight permeability in the range of nano- to milli-Darcy because of their complex pore structure [74, 349]. They exhibit various types of pore space interconnectivity, complex pore size distributions, and heterogeneity [74, 350]. Although our datasets encompassed both sandstone and carbonate rocks so as to be more generalized than those in previous literature, unconventional resources were outside our scope. Many researchers attempted to study the petrophysical and geomechanical properties of unconventional resources digitally using a suite of multiple imaging techniques [351, 352]. Using the DRA framework is anticipated to be more difficult in unconventional resources because micro-CT scanning can only partially resolve the pore space in such material. Therefore, it would be beneficial to extend the applications of our DL frameworks, specifically the super-resolution and segmentation, to evaluate their accuracy in these special hydrocarbon resources and compare them with the accuracy achieved in conventional resources.

References

1. Blunt, M.J., et al., *Pore-scale imaging and modelling.* Advances in Water Resources, 2013. **51**: p. 197-216.
2. Wildenschild, D. and A.P. Sheppard, *X-ray imaging and analysis techniques for quantifying pore-scale structure and processes in subsurface porous medium systems.* Advances in Water Resources, 2013. **51**: p. 217-246.
3. Andrä, H., et al., *Digital rock physics benchmarks—Part I: Imaging and segmentation.* Computers & Geosciences, 2013. **50**: p. 25-32.
4. Bultreys, T., W. De Boever, and V. Cnudde, *Imaging and image-based fluid transport modeling at the pore scale in geological materials: A practical introduction to the current state-of-the-art.* Earth-Science Reviews, 2016. **155**: p. 93-128.
5. Armstrong, R.T., M.L. Porter, and D. Wildenschild, *Linking pore-scale interfacial curvature to column-scale capillary pressure.* Advances in Water Resources, 2012. **46**: p. 55-62.
6. Dann, R., et al., *Multi-scale characterisation of coastal sand aquifer media for contaminant transport using X-ray computed tomography.* Environmental Earth Sciences, 2011. **63**(5): p. 1125-1137.
7. Liu, M., M. Shabaninejad, and P. Mostaghimi, *Impact of mineralogical heterogeneity on reactive transport modelling.* Computers & Geosciences, 2017. **104**: p. 12-19.
8. Werth, C.J., et al., *A review of non-invasive imaging methods and applications in contaminant hydrogeology research.* Journal of Contaminant Hydrology, 2010. **113**(1): p. 1-24.
9. Han, J., et al., *Application of digital rock physics using X-ray CT for study on alteration of macropore properties by CO2 EOR in a carbonate oil reservoir.* Journal of Petroleum Science and Engineering, 2020. **189**: p. 107009.
10. Al-Khulaifi, Y., et al., *Reservoir-condition pore-scale imaging of dolomite reaction with supercritical CO2 acidified brine: Effect of pore-structure on reaction rate using velocity distribution analysis.* International Journal of Greenhouse Gas Control, 2018. **68**: p. 99-111.
11. Al-Menhali, A.S., et al., *Pore Scale Observations of Trapped CO2 in Mixed-Wet Carbonate Rock: Applications to Storage in Oil Fields.* Environmental Science & Technology, 2016. **50**(18): p. 10282-10290.
12. Silin, D., et al., *Microtomography and Pore-Scale Modeling of Two-Phase Fluid Distribution.* Transport in Porous Media, 2011. **86**(2): p. 495-515.
13. Iglauer, S., et al., *Residual CO2 imaged with X-ray micro-tomography.* Geophysical Research Letters, 2011. **38**(21).
14. Yang, Y., et al., *Dynamic Pore-Scale Dissolution by CO2-Saturated Brine in Carbonates: Impact of Homogeneous Versus Fractured Versus Vuggy Pore Structure.* Water Resources Research, 2020. **56**(4): p. e2019WR026112.
15. Arns, C.H., et al., *Computation of linear elastic properties from microtomographic images: Methodology and agreement between theory and experiment.* GEOPHYSICS, 2002. **67**(5): p. 1396-1405.
16. Andrä, H., et al., *Digital rock physics benchmarks—part II: Computing effective properties.* Computers & Geosciences, 2013. **50**: p. 33-43.
17. Wang, Y., et al., *Pore scale investigation on scaling-up micro-macro capillary number and wettability on trapping and mobilization of residual fluid.* Journal of Contaminant Hydrology, 2019. **225**: p. 103499.
18. Lebedeva, E.V. and A. Fogden, *Micro-CT and Wettability Analysis of Oil Recovery from Sand Packs and the Effect of Waterflood Salinity and Kaolinite.* Energy & Fuels, 2011. **25**(12): p. 5683-5694.

19. Alzahid, Y.A., et al., *Real-time synchrotron-based X-ray computed microtomography during in situ emulsification.* Journal of Petroleum Science and Engineering, 2020. **195**: p. 107885.
20. Wang, Y.D., et al., *Deep learning in pore scale imaging and modeling.* Earth-Science Reviews, 2021. **215**: p. 103555.
21. Tahmasebi, P., et al., *Machine learning in geo- and environmental sciences: From small to large scale.* Advances in Water Resources, 2020. **142**: p. 103619.
22. Singh, A., et al., *Computer vision and unsupervised machine learning for pore-scale structural analysis of fractured porous media.* Advances in Water Resources, 2021. **147**: p. 103801.
23. Karimpouli, S. and P. Tahmasebi, *Segmentation of digital rock images using deep convolutional autoencoder networks.* Computers & Geosciences, 2019. **126**: p. 142-150.
24. Karimpouli, S. and P. Tahmasebi, *Image-based velocity estimation of rock using Convolutional Neural Networks.* Neural Networks, 2019. **111**: p. 89-97.
25. Niu, Y., et al., *Digital Rock Segmentation for Petrophysical Analysis With Reduced User Bias Using Convolutional Neural Networks.* Water Resources Research, 2020. **56**(2): p. e2019WR026597.
26. Rabbani, A., et al., *DeePore: A deep learning workflow for rapid and comprehensive characterization of porous materials.* Advances in Water Resources, 2020. **146**: p. 103787.
27. Erofeev, A., et al., *Prediction of Porosity and Permeability Alteration Based on Machine Learning Algorithms.* Transport in Porous Media, 2019. **128**(2): p. 677-700.
28. Goodfellow, I., Y. Bengio, and A. Courville, *Deep Learning*. 2016: MIT Press.
29. Greenspan, H., B.v. Ginneken, and R.M. Summers, *Guest Editorial Deep Learning in Medical Imaging: Overview and Future Promise of an Exciting New Technique.* IEEE Transactions on Medical Imaging, 2016. **35**(5): p. 1153-1159.
30. Suzuki, K., *Overview of deep learning in medical imaging.* Radiological Physics and Technology, 2017. **10**(3): p. 257-273.
31. Ma, L., et al., *Deep learning in remote sensing applications: A meta-analysis and review.* ISPRS Journal of Photogrammetry and Remote Sensing, 2019. **152**: p. 166-177.
32. Nielsen, M.A., *Neural networks and deep learning*. Vol. 25. 2015: Determination press USA.
33. Xu, C., et al. *When Petrophysics Meets Big Data: What can Machine Do?* in *SPE Middle East Oil and Gas Show and Conference*. 2019.
34. Saxena, N., et al., *Effect of image segmentation & voxel size on micro-CT computed effective transport & elastic properties.* Marine and Petroleum Geology, 2017. **86**: p. 972-990.
35. Berg, S., et al., *Determination of critical gas saturation by micro-CT.* Petrophysics, 2020. **61**(2): p. 133-150.
36. Suhrer, M., et al. *Upscaling method for obtaining primary drainage capillary pressure and resistivity index with digital rock physics*. in *International Petroleum Technology Conference 2020, IPTC 2020*. 2020.
37. Dernaika, M., et al., *Digital and conventional techniques to study permeability heterogeneity in complex carbonate rocks.* Petrophysics, 2018. **59**(3): p. 373-396.
38. Koroteev, D., et al. *Application of digital rock technology for chemical EOR screening*. in *Society of Petroleum Engineers - SPE Enhanced Oil Recovery Conference, EORC 2013: Delivering the Promise NOW!* 2013.
39. Deshenenkov, I. and C. Polo, *The digital rock analysis of biogenically induced reservoir heterogeneities in Cretaceous reservoirs of Saudi Arabia.* E3S Web Conf., 2020. **146**: p. 01004.

40. Fredrich, J.T., et al. *Digital Rocks: Developing an Emerging Technology Through to a Proven Capability Deployed in the Business*. in *SPE Annual Technical Conference and Exhibition*. 2014.
41. Andersen, M., B. Duncan, and R. McLin. *Core Truth in Formation Evaluation*. 2013.
42. McPhee, C., J. Reed, and I. Zubizarreta, *Core Analysis: A Best Practice Guide*. 2015: Elsevier Science.
43. Al-Muthana, A.S., S.M. Ma, and T. Okasha. *Best Practices in Conventional Core Analysis - A Laboratory Investigation*. in *SPE Saudi Arabia Section Technical Symposium*. 2008.
44. Siddiqui, S., et al., *Improvements in the selection criteria for the representative special core analysis samples.* SPE Reservoir Evaluation & Engineering, 2006. **9**(06): p. 647-653.
45. Stiles Jr, J. and J. Hutfilz, *The use of routine and special core analysis in characterizing Brent Group reservoirs, UK North Sea.* Journal of Petroleum Technology, 1992. **44**(06): p. 704-713.
46. Berg, C.F., O. Lopez, and H. Berland, *Industrial applications of digital rock technology.* Journal of Petroleum Science and Engineering, 2017. **157**: p. 131-147.
47. Klemin, D., et al. *Digital Rock Technology Accelerates Carbonate Rock Laboratory Analysis*. in *SPE Gas & Oil Technology Showcase and Conference*. 2019.
48. Mostaghimi, P., M.J. Blunt, and B. Bijeljic, *Computations of Absolute Permeability on Micro-CT Images.* Mathematical Geosciences, 2013. **45**(1): p. 103-125.
49. Wang, Y.D., et al., *Computations of permeability of large rock images by dual grid domain decomposition.* Advances in Water Resources, 2019. **126**: p. 1-14.
50. Cnudde, V. and M.N. Boone, *High-resolution X-ray computed tomography in geosciences: A review of the current technology and applications.* Earth-Science Reviews, 2013. **123**: p. 1-17.
51. CALVERT, S.E. and J.J. VEEVERS, *MINOR STRUCTURES OF UNCONSOLIDATED MARINE SEDIMENTS REVEALED BY X-RADIOGRAPHY1.* Sedimentology, 1962. **1**(4): p. 287-295.
52. Baker, S.R. and G.M. Friedman, *A non-destructive core analysis technique using X-rays.* Journal of Sedimentary Research, 1969. **39**(4): p. 1371-1383.
53. Ommaya, A., et al., *Computerized axial tomography: estimation of spatial and density resolution capability.* The British journal of radiology, 1976. **49**(583): p. 604-611.
54. Grangeat, P. *Mathematical framework of cone beam 3D reconstruction via the first derivative of the radon transform*. in *Mathematical Methods in Tomography*. 1991. Berlin, Heidelberg: Springer Berlin Heidelberg.
55. Varslot, T., et al., *High-resolution helical cone-beam micro-CT with theoretically-exact reconstruction from experimental data.* Medical Physics, 2011. **38**(10): p. 5459-5476.
56. Herman, G.T., *Fundamentals of computerized tomography: image reconstruction from projections*. 2009: Springer Science & Business Media.
57. Kak, A.C., M. Slaney, and G. Wang, *Principles of computerized tomographic imaging*. 2002, Wiley Online Library.
58. Goldman, L.W., *Principles of CT and CT technology.* Journal of nuclear medicine technology, 2007. **35**(3): p. 115-128.
59. Sato, T., et al., *X-ray tomography for microstructural objects.* Applied optics, 1981. **20**(22): p. 3880-3883.
60. Elliott, J.C. and S. Dover, *X-ray microtomography.* Journal of microscopy, 1982. **126**(2): p. 211-213.
61. Flannery, B.P., et al., *Three-dimensional X-ray microtomography.* Science, 1987. **237**(4821): p. 1439-1444.
62. Baruchel, J., et al., *Advances in synchrotron radiation microtomography.* Scripta Materialia, 2006. **55**(1): p. 41-46.

63. Dyck, V., *Desktop X-ray microscopy and microtomography.* Journal of Microscopy, 1998. **191**(2): p. 151-158.
64. Masschaele, B.C., et al., *UGCT: New X-ray radiography and tomography facility.* Nuclear Instruments and Methods in Physics Research Section A: Accelerators, Spectrometers, Detectors and Associated Equipment, 2007. **580**(1): p. 266-269.
65. Jakubek, J., et al., *Experimental system for high resolution X-ray transmission radiography.* Nuclear Instruments and Methods in Physics Research Section A: Accelerators, Spectrometers, Detectors and Associated Equipment, 2006. **563**(1): p. 278-281.
66. Sheppard, A.P., R.M. Sok, and H. Averdunk, *Techniques for image enhancement and segmentation of tomographic images of porous materials.* Physica A: Statistical Mechanics and its Applications, 2004. **339**(1): p. 145-151.
67. Gürsoy, D., et al., *TomoPy: a framework for the analysis of synchrotron tomographic data.* Journal of synchrotron radiation, 2014. **21**(5): p. 1188-1193.
68. Vo, N.T., R.C. Atwood, and M. Drakopoulos, *Superior techniques for eliminating ring artifacts in X-ray micro-tomography.* Optics Express, 2018. **26**(22): p. 28396-28412.
69. Vo, N., R. Atwood, and M. Drakopoulos, *Preprocessing techniques for removing artifacts in synchrotron-based tomographic images*. SPIE Optical Engineering + Applications. Vol. 11113. 2019: SPIE.
70. Shah, S.M., et al., *Micro-computed tomography pore-scale study of flow in porous media: Effect of voxel resolution.* Advances in Water Resources, 2016. **95**: p. 276-287.
71. Christe, P., et al., *An X-ray computed tomography-based index to characterize the quality of cataclastic carbonate rock samples.* Engineering Geology, 2011. **117**(3): p. 180-188.
72. Arns, C.H., et al., *Pore Scale Characterization of Carbonates Using X-Ray Microtomography.* SPE Journal, 2005. **10**(04): p. 475-484.
73. Ramandi, H.L., P. Mostaghimi, and R.T. Armstrong, *Digital rock analysis for accurate prediction of fractured media permeability.* Journal of Hydrology, 2017. **554**: p. 817-826.
74. Algazlan, M., et al., *Petrophysical assessment of Australian organic-rich shales: Beetaloo, Cooper and Perth basins.* Journal of Natural Gas Science and Engineering, 2019. **70**: p. 102952.
75. Semnani, S.J. and R.I. Borja, *Quantifying the heterogeneity of shale through statistical combination of imaging across scales.* Acta Geotechnica, 2017. **12**(6): p. 1193-1205.
76. Roslin, A., D. Pokrajac, and Y. Zhou, *Cleat structure analysis and permeability simulation of coal samples based on micro-computed tomography (micro-CT) and scan electron microscopy (SEM) technology.* Fuel, 2019. **254**: p. 115579.
77. Man, B.D., et al. *Metal streak artifacts in X-ray computed tomography: a simulation study*. in *1998 IEEE Nuclear Science Symposium Conference Record. 1998 IEEE Nuclear Science Symposium and Medical Imaging Conference (Cat. No.98CH36255)*. 1998.
78. Turbell, H., *Cone-beam reconstruction using filtered backprojection*. 2001, Linköping University Electronic Press.
79. Boone, M.N., et al., *Secondary radiation in transmission-type X-ray tubes: Simulation, practical issues and solution in the context of X-ray microtomography.* Nuclear Instruments and Methods in Physics Research Section A: Accelerators, Spectrometers, Detectors and Associated Equipment, 2012. **661**(1): p. 7-12.
80. Holt, J., et al., *Correction of beam hardening artefacts in microtomography for samples imaged in containers*. SPIE Optical Engineering + Applications. Vol. 9212. 2014: SPIE.
81. Sun, H., et al., *Rock properties evaluation for carbonate reservoir characterization with multi-scale digital rock images.* Journal of Petroleum Science and Engineering, 2019. **175**: p. 654-664.

82. Sok, R.M., et al., *Pore scale characterization of carbonates at multiple scales: Integration of Micro-CT, BSEM, and FIBSEM.* Petrophysics-The SPWLA Journal of Formation Evaluation and Reservoir Description, 2010. **51**(06).
83. Grader, A.S., et al. *Multi-scale imaging process for computations of porosity and permeability from carbonate rocks*. in *Adapted from oral presentation at AAPG Convention, New Orleans, Louisiana*. 2010.
84. Louis, L. *Integration of Rock Images and Laboratory Data Through the Lens of a New Discipline*. in *52nd U.S. Rock Mechanics/Geomechanics Symposium*. 2018.
85. Liu, M., M. Shabaninejad, and P. Mostaghimi, *Predictions of permeability, surface area and average dissolution rate during reactive transport in multi-mineral rocks.* Journal of Petroleum Science and Engineering, 2018. **170**: p. 130-138.
86. Akai, T., et al., *Modeling Oil Recovery in Mixed-Wet Rocks: Pore-Scale Comparison Between Experiment and Simulation.* Transport in Porous Media, 2019. **127**(2): p. 393-414.
87. Iassonov, P., T. Gebrenegus, and M. Tuller, *Segmentation of X-ray computed tomography images of porous materials: A crucial step for characterization and quantitative analysis of pore structures.* Water Resources Research, 2009. **45**(9): p. n/a-n/a.
88. Otsu, N., *A threshold selection method from gray-level histograms.* IEEE transactions on systems, man, and cybernetics, 1979. **9**(1): p. 62-66.
89. Arthur, D. and S. Vassilvitskii, *k-means++: The advantages of careful seeding*. 2006, Stanford.
90. Ridler, T. and S. Calvard, *Picture thresholding using an iterative selection method.* IEEE trans syst Man Cybern, 1978. **8**(8): p. 630-632.
91. Singh, A., et al., *Rock Characterization Using Gray-Level Co-Occurrence Matrix: An Objective Perspective of Digital Rock Statistics.* Water Resources Research, 2019. **55**(3): p. 1912-1927.
92. Wonho, O. and B. Lindquist, *Image thresholding by indicator kriging.* IEEE Transactions on Pattern Analysis and Machine Intelligence, 1999. **21**(7): p. 590-602.
93. Vincent, L. and P. Soille, *Watersheds in digital spaces: an efficient algorithm based on immersion simulations.* IEEE Computer Architecture Letters, 1991. **13**(06): p. 583-598.
94. Smal, P., P. Gouze, and O. Rodriguez, *An automatic segmentation algorithm for retrieving sub-resolution porosity from X-ray tomography images.* Journal of Petroleum Science and Engineering, 2018. **166**: p. 198-207.
95. Houston, A.N., et al., *Adaptive-window indicator kriging: A thresholding method for computed tomography images of porous media.* Computers & Geosciences, 2013. **54**: p. 239-248.
96. Oh, W. and B. Lindquist, *Image thresholding by indicator kriging.* IEEE Transactions on Pattern Analysis and Machine Intelligence, 1999. **21**(7): p. 590-602.
97. Figueiredo, M.A.T. and A.K. Jain, *Unsupervised learning of finite mixture models.* IEEE Transactions on Pattern Analysis and Machine Intelligence, 2002. **24**(3): p. 381-396.
98. Schlüter, S., et al., *Image processing of multiphase images obtained via X-ray microtomography: A review.* Water Resources Research, 2014. **50**(4): p. 3615-3639.
99. Rabbani, A. and M. Babaei, *Image-based modeling of carbon storage in fractured organic-rich shale with deep learning acceleration.* Fuel, 2021. **299**: p. 120795.
100. Menet, S., P. Saint-Marc, and G. Medioni. *Active contour models: overview, implementation and applications*. in *1990 IEEE International Conference on Systems, Man, and Cybernetics Conference Proceedings*. 1990.
101. ZHANG, Y., P. MOSTAGHIMI, and R.T. ARMSTRONG, *On the challenges of greyscale-based quantifications using X-ray computed microtomography.* Journal of Microscopy, 2019. **275**(2): p. 82-96.

102. An, S., et al., *Lattice-Boltzmann simulation of dissolution of carbonate rock during CO2-saturated brine injection.* Chemical Engineering Journal, 2021. **408**: p. 127235.
103. Andrew, M., B. Bijeljic, and M.J. Blunt, *Pore-scale contact angle measurements at reservoir conditions using X-ray microtomography.* Advances in Water Resources, 2014. **68**: p. 24-31.
104. Bishop, C.M., *Pattern Recognition and Machine Learning*. 2006: Springer.
105. Chauhan, S., et al., *Phase segmentation of X-ray computer tomography rock images using machine learning techniques: an accuracy and performance study.* Solid Earth, 2016. **7**(4): p. 1125-1139.
106. Chauhan, S., et al., *Processing of rock core microtomography images: Using seven different machine learning algorithms.* Computers & Geosciences, 2016. **86**: p. 120-128.
107. Purswani, P., et al., *Evaluation of image segmentation techniques for image-based rock property estimation.* Journal of Petroleum Science and Engineering, 2020. **195**: p. 107890.
108. Mohri, M., A. Rostamizadeh, and A. Talwalkar, *Foundations of machine learning*. 2018: MIT press.
109. Wang, W., H. Liao, and Y. Huang. *Rock fracture tracing based on image processing and SVM*. in *Third International Conference on Natural Computation (ICNC 2007)*. 2007.
110. Liang, H. and J. Zou, *Rock Image Segmentation of Improved Semi-supervised SVM–FCM Algorithm Based on Chaos.* Circuits, Systems, and Signal Processing, 2020. **39**(2): p. 571-585.
111. Li, B., et al., *Fracture and vug characterization and carbonate rock type automatic classification using X-ray CT images.* Journal of Petroleum Science and Engineering, 2017. **153**: p. 88-96.
112. Iwaszenko, S. and A. Smoliński, *Texture features for bulk rock material grain boundary segmentation.* Journal of King Saud University - Engineering Sciences, 2021. **33**(2): p. 95-103.
113. Wang, Y.D., et al., *Deep neural networks for improving physical accuracy of 2D and 3D multi-mineral segmentation of rock micro-CT images.* Applied Soft Computing, 2021. **104**: p. 107185.
114. Akkus, Z., et al., *Deep Learning for Brain MRI Segmentation: State of the Art and Future Directions.* Journal of Digital Imaging, 2017. **30**(4): p. 449-459.
115. Grigorescu, S., et al., *A survey of deep learning techniques for autonomous driving.* Journal of Field Robotics, 2020. **37**(3): p. 362-386.
116. Alzahid, Y.A., et al., *Oil mobilization and solubilization in porous media by in situ emulsification.* Journal of Colloid and Interface Science, 2019. **554**: p. 554-564.
117. Armstrong, R.T., et al., *Porous Media Characterization Using Minkowski Functionals: Theories, Applications and Future Directions.* Transport in Porous Media, 2018.
118. Hussaini, S.R. and J. Dvorkin, *Specific surface area versus porosity from digital images.* Journal of Petroleum Science and Engineering, 2021. **196**: p. 107773.
119. Sahimi, M., *Flow and transport in porous media and fractured rock: from classical methods to modern approaches*. 2011: John Wiley & Sons.
120. AlRatrout, A., et al., *Automatic measurement of contact angle in pore-space images.* Advances in Water Resources, 2017. **109**: p. 158-169.
121. Huang, J., et al., *Diffusion tortuosity in complex porous media from pore-scale numerical simulations.* Computers & Fluids, 2019. **183**: p. 66-74.
122. Fu, J., H.R. Thomas, and C. Li, *Tortuosity of porous media: Image analysis and physical simulation.* Earth-Science Reviews, 2021. **212**: p. 103439.
123. Nakashima, Y. and S. Kamiya, *Mathematica Programs for the Analysis of Three-Dimensional Pore Connectivity and Anisotropic Tortuosity of Porous Rocks using X-ray*

Computed Tomography Image Data. Journal of Nuclear Science and Technology, 2007. **44**(9): p. 1233-1247.
124. Agbogun, H.M.D., T.A. Al, and E.M.A. Hussein, *Three dimensional imaging of porosity and tracer concentration distributions in a dolostone sample during diffusion experiments using X-ray micro-CT.* Journal of Contaminant Hydrology, 2013. **145**: p. 44-53.
125. Mostaghimi, P., B. Bijeljic, and M.J. Blunt, *Simulation of Flow and Dispersion on Pore-Space Images.* SPE Journal, 2012. **17**(04): p. 1131-1141.
126. Arns, C., et al., *Virtual permeametry on microtomographic images*. Vol. 45. 2004. 41-46.
127. Liu, J., G.G. Pereira, and K. Regenauer-Lieb, *From characterisation of pore-structures to simulations of pore-scale fluid flow and the upscaling of permeability using microtomography: A case study of heterogeneous carbonates.* Journal of Geochemical Exploration, 2014. **144**: p. 84-96.
128. Liu, M. and P. Mostaghimi, *Reactive transport modelling in dual porosity media.* Chemical Engineering Science, 2018. **190**: p. 436-442.
129. Liu, M. and P. Mostaghimi, *Pore-scale simulation of dissolution-induced variations in rock mechanical properties.* International Journal of Heat and Mass Transfer, 2017. **111**: p. 842-851.
130. Liu, J., R. Freij-Ayoub, and K. Regenauer-Lieb, *Rock plasticity from microtomography and upscaling.* Journal of Earth Science, 2015. **26**(1): p. 53-59.
131. Schrank, C.E., et al., *Thermal-elastic stresses and the criticality of the continental crust.* Geochemistry, Geophysics, Geosystems, 2012. **13**(9).
132. Ramstad, T., P.-E. Øren, and S. Bakke, *Simulation of Two-Phase Flow in Reservoir Rocks Using a Lattice Boltzmann Method.* SPE Journal, 2010. **15**(04): p. 917-927.
133. Armstrong, R.T., et al., *Flow regimes during immiscible displacement.* Petrophysics, 2017. **58**(01): p. 10-18.
134. Lu, X., et al., *3D microstructure design of lithium-ion battery electrodes assisted by X-ray nano-computed tomography and modelling.* Nature Communications, 2020. **11**(1): p. 2079.
135. Tan, C., et al., *Three-dimensional image based modelling of transport parameters in lithium–sulfur batteries.* Physical Chemistry Chemical Physics, 2019. **21**(8): p. 4145-4154.
136. Arand, F. and J. Hesser, *Accurate and efficient maximal ball algorithm for pore network extraction.* Computers & Geosciences, 2017. **101**: p. 28-37.
137. Dong, H. and M.J. Blunt, *Pore-network extraction from micro-computerized-tomography images.* Physical Review E, 2009. **80**(3): p. 036307.
138. Silin, D. and T. Patzek, *Pore space morphology analysis using maximal inscribed spheres.* Physica A: Statistical Mechanics and its Applications, 2006. **371**(2): p. 336-360.
139. Lindquist, W.B., et al., *Medial axis analysis of void structure in three-dimensional tomographic images of porous media.* Journal of Geophysical Research: Solid Earth, 1996. **101**(B4): p. 8297-8310.
140. Rabbani, A., S. Jamshidi, and S. Salehi, *An automated simple algorithm for realistic pore network extraction from micro-tomography images.* Journal of Petroleum Science and Engineering, 2014. **123**: p. 164-171.
141. Rabbani, A., M. Babaei, and F. Javadpour, *A Triple Pore Network Model (T-PNM) for Gas Flow Simulation in Fractured, Micro-porous and Meso-porous Media.* Transport in Porous Media, 2020. **132**(3): p. 707-740.
142. Gostick, J.T., *Versatile and efficient pore network extraction method using marker-based watershed segmentation.* Physical Review E, 2017. **96**(2): p. 023307.

143. Baychev, T.G., et al., *Reliability of Algorithms Interpreting Topological and Geometric Properties of Porous Media for Pore Network Modelling.* Transport in Porous Media, 2019. **128**(1): p. 271-301.
144. Constantin, P. and C. Foias, *Navier-stokes equations*. 1988: University of Chicago Press.
145. White, J.A., R.I. Borja, and J.T. Fredrich, *Calculating the effective permeability of sandstone with multiscale lattice Boltzmann/finite element simulations.* Acta Geotechnica, 2006. **1**(4): p. 195-209.
146. Sun, Z., R.E. Logé, and M. Bernacki, *3D finite element model of semi-solid permeability in an equiaxed granular structure.* Computational Materials Science, 2010. **49**(1): p. 158-170.
147. McClure, J.E., et al., *Estimating interfacial areas resulting from lattice Boltzmann simulation of two-fluid-phase flow in a porous medium*, in *Developments in Water Science*, C.T. Miller, et al., Editors. 2004, Elsevier. p. 23-35.
148. Ferréol, B. and D.H. Rothman, *Lattice-Boltzmann simulations of flow through Fontainebleau sandstone.* Transport in Porous Media, 1995. **20**(1): p. 3-20.
149. Shabro, V., et al., *Finite-Difference Approximation for Fluid-Flow Simulation and Calculation of Permeability in Porous Media.* Transport in Porous Media, 2012. **94**(3): p. 775-793.
150. Chung, T., et al., *Approximating Permeability of Microcomputed-Tomography Images Using Elliptic Flow Equations.* SPE Journal, 2019. **24**(03): p. 1154-1163.
151. Chung, T., et al., *Voxel agglomeration for accelerated estimation of permeability from micro-CT images.* Journal of Petroleum Science and Engineering, 2020. **184**: p. 106577.
152. Bakke, S. and P.-E. Øren, *3-D Pore-Scale Modelling of Sandstones and Flow Simulations in the Pore Networks.* SPE Journal, 1997. **2**(02): p. 136-149.
153. Blunt, M.J., et al., *Detailed physics, predictive capabilities and macroscopic consequences for pore-network models of multiphase flow.* Advances in Water Resources, 2002. **25**(8): p. 1069-1089.
154. Sorbie, K.S. and A. Skauge, *Can Network Modeling Predict Two-Phase Flow Functions?* Petrophysics - The SPWLA Journal of Formation Evaluation and Reservoir Description, 2012. **53**(06): p. 401-409.
155. AlRatrout, A., M.J. Blunt, and B. Bijeljic, *Wettability in complex porous materials, the mixed-wet state, and its relationship to surface roughness.* Proceedings of the National Academy of Sciences, 2018. **115**(36): p. 8901-8906.
156. Jettestuen, E., H.A. Friis, and J.O. Helland, *A locally conservative multiphase level set method for capillary-controlled displacements in porous media.* Journal of Computational Physics, 2021. **428**: p. 109965.
157. Prodanović, M. and S.L. Bryant, *A level set method for determining critical curvatures for drainage and imbibition.* Journal of Colloid and Interface Science, 2006. **304**(2): p. 442-458.
158. Jettestuen, E., J.O. Helland, and M. Prodanović, *A level set method for simulating capillary-controlled displacements at the pore scale with nonzero contact angles.* Water Resources Research, 2013. **49**(8): p. 4645-4661.
159. Huang, H., P. Meakin, and M. Liu, *Computer simulation of two-phase immiscible fluid motion in unsaturated complex fractures using a volume of fluid method.* Water Resources Research, 2005. **41**(12).
160. Ferrari, A. and I. Lunati, *Direct numerical simulations of interface dynamics to link capillary pressure and total surface energy.* Advances in Water Resources, 2013. **57**: p. 19-31.
161. Boek, E.S. and M. Venturoli, *Lattice-Boltzmann studies of fluid flow in porous media with realistic rock geometries.* Computers & Mathematics with Applications, 2010. **59**(7): p. 2305-2314.

162. Soulaine, C., et al., *The Impact of Sub-Resolution Porosity of X-ray Microtomography Images on the Permeability.* Transport in Porous Media, 2016. **113**(1): p. 227-243.
163. Singh, A., et al., *On Representative Elementary Volumes of Grayscale Micro-CT Images of Porous Media.* Geophysical Research Letters, 2020. **47**(15): p. e2020GL088594.
164. Saenger, E.H., et al., *Digital carbonate rock physics.* Solid Earth, 2016. **7**(4): p. 1185-1197.
165. Andrä, H., et al., *Digital rock physics benchmarks—Part I: Imaging and segmentation.* Computers & Geosciences, 2013. **50**: p. 25-32.
166. Garfi, G., et al., *The Sensitivity of Estimates of Multiphase Fluid and Solid Properties of Porous Rocks to Image Processing.* Transport in Porous Media, 2020. **131**(3): p. 985-1005.
167. Pot, V., X. Zhong, and P.C. Baveye, *Effect of resolution, reconstruction settings, and segmentation methods on the numerical calculation of saturated soil hydraulic conductivity from 3D computed tomography images.* Geoderma, 2020. **362**: p. 114089.
168. Leu, L., et al., *Fast X-ray Micro-Tomography of Multiphase Flow in Berea Sandstone: A Sensitivity Study on Image Processing.* Transport in Porous Media, 2014. **105**(2): p. 451-469.
169. Saxena, N., et al., *Imaging and computational considerations for image computed permeability: Operating envelope of Digital Rock Physics.* Advances in Water Resources, 2018. **116**: p. 127-144.
170. Arns, C.H., M.A. Knackstedt, and N.S. Martys, *Cross-property correlations and permeability estimation in sandstone.* Physical Review E, 2005. **72**(4): p. 046304.
171. Hilfer, R. and A. Lemmer, *Differential porosimetry and permeametry for random porous media.* Physical Review E, 2015. **92**(1): p. 013305.
172. Saxena, N., et al., *Rock properties from micro-CT images: Digital rock transforms for resolution, pore volume, and field of view.* Advances in Water Resources, 2019. **134**: p. 103419.
173. Arns, C.H., et al. *Pore-Type Partitioning for Complex Carbonates: Effective Versus Total Porosity and Applications to Electrical Conductivity*. in *SPWLA 59th Annual Logging Symposium*. 2018.
174. Yang, X., et al., *Intercomparison of 3D pore-scale flow and solute transport simulation methods.* Advances in Water Resources, 2016. **95**: p. 176-189.
175. Liu, Z., et al., *Pore-Scale Characterization of Two-Phase Flow Using Integral Geometry.* Transport in Porous Media, 2017. **118**(1): p. 99-117.
176. Krizhevsky, A., I. Sutskever, and G.E. Hinton, *ImageNet classification with deep convolutional neural networks*, in *Proceedings of the 25th International Conference on Neural Information Processing Systems - Volume 1*. 2012, Curran Associates Inc.: Lake Tahoe, Nevada. p. 1097-1105.
177. Silver, D., et al., *A general reinforcement learning algorithm that masters chess, shogi, and Go through self-play.* Science, 2018. **362**(6419): p. 1140-1144.
178. Silver, D., et al., *Mastering the game of Go with deep neural networks and tree search.* Nature, 2016. **529**(7587): p. 484-489.
179. Senior, A.W., et al., *Improved protein structure prediction using potentials from deep learning.* Nature, 2020. **577**(7792): p. 706-710.
180. Rosenblatt, F., *The perceptron: A probabilistic model for information storage and organization in the brain.* Psychological Review, 1958. **65**(6): p. 386-408.
181. Fukushima, K., *Neocognitron: A self-organizing neural network model for a mechanism of pattern recognition unaffected by shift in position.* Biological Cybernetics, 1980. **36**(4): p. 193-202.
182. Werbos, P.J., *Backpropagation through time: what it does and how to do it.* Proceedings of the IEEE, 1990. **78**(10): p. 1550-1560.

183. Khotanzad, A. and J.-H. Lu. *Distortion invariant character recognition by a multi-layer perceptron and back-propagation learning*. in *ICNN*. 1988.
184. Goryn, D. and M. Kaveh. *Conjugate gradient learning algorithms for multilayer perceptrons*. in *Proceedings of the 32nd Midwest Symposium on Circuits and Systems*. 1989. IEEE.
185. Lecun, Y., et al., *Gradient-based learning applied to document recognition.* Proceedings of the IEEE, 1998. **86**(11): p. 2278-2324.
186. LeCun, Y., et al., *Backpropagation Applied to Handwritten Zip Code Recognition.* Neural Computation, 1989. **1**(4): p. 541-551.
187. Bronstein, M.M., et al. *Geometric Deep Learning: Grids, Groups, Graphs, Geodesics, and Gauges*. 2021. arXiv:2104.13478.
188. Maturana, D. and S. Scherer. *VoxNet: A 3D Convolutional Neural Network for real-time object recognition*. in *2015 IEEE/RSJ International Conference on Intelligent Robots and Systems (IROS)*. 2015.
189. Bengio, Y., A. Courville, and P. Vincent *Representation Learning: A Review and New Perspectives*. arXiv e-prints, 2012.
190. Schuster, M. and K.K. Paliwal, *Bidirectional recurrent neural networks.* IEEE Transactions on Signal Processing, 1997. **45**(11): p. 2673-2681.
191. Giles, C.L., G.M. Kuhn, and R.J. Williams, *Dynamic recurrent neural networks: Theory and applications.* IEEE Transactions on Neural Networks, 1994. **5**(2): p. 153-156.
192. Mikolov, T., et al. *Extensions of recurrent neural network language model*. in *2011 IEEE International Conference on Acoustics, Speech and Signal Processing (ICASSP)*. 2011.
193. Connor, J.T., R.D. Martin, and L.E. Atlas, *Recurrent neural networks and robust time series prediction.* IEEE Transactions on Neural Networks, 1994. **5**(2): p. 240-254.
194. Goodfellow, I.J., et al. *Generative Adversarial Networks*. 2014. arXiv:1406.2661.
195. Zhang, X., et al. *SegGAN: Semantic Segmentation with Generative Adversarial Network*. in *2018 IEEE Fourth International Conference on Multimedia Big Data (BigMM)*. 2018.
196. Han, C., et al. *GAN-based synthetic brain MR image generation*. in *2018 IEEE 15th International Symposium on Biomedical Imaging (ISBI 2018)*. 2018. IEEE.
197. Ar Rushood, I., et al. *Segmentation of X-Ray Images of Rocks Using Deep Learning*. in *SPE Annual Technical Conference and Exhibition*. 2020.
198. Wang, Y., et al., *CT-image of rock samples super resolution using 3D convolutional neural network.* Computers & Geosciences, 2019. **133**: p. 104314.
199. Wang, Y.D., R.T. Armstrong, and P. Mostaghimi, *Enhancing Resolution of Digital Rock Images with Super Resolution Convolutional Neural Networks.* Journal of Petroleum Science and Engineering, 2019. **182**: p. 106261.
200. Wang, Y.D., R.T. Armstrong, and P. Mostaghimi, *Boosting Resolution and Recovering Texture of 2D and 3D Micro-CT Images with Deep Learning.* Water Resources Research, 2020. **56**(1): p. e2019WR026052.
201. Chen, H., et al., *Super-resolution of real-world rock microcomputed tomography images using cycle-consistent generative adversarial networks.* Physical Review E, 2020. **101**(2): p. 023305.
202. Niu, Y., et al., *Geometrical-Based Generative Adversarial Network to Enhance Digital Rock Image Quality.* Physical Review Applied, 2021. **15**(6): p. 064033.
203. Mosser, L., O. Dubrule, and M.J. Blunt, *Reconstruction of three-dimensional porous media using generative adversarial neural networks.* Physical Review E, 2017. **96**(4): p. 043309.
204. Mosser, L., O. Dubrule, and M.J. Blunt, *Stochastic Reconstruction of an Oolitic Limestone by Generative Adversarial Networks.* Transport in Porous Media, 2018. **125**(1): p. 81-103.

205. Feng, J., et al., *An end-to-end three-dimensional reconstruction framework of porous media from a single two-dimensional image based on deep learning.* Computer Methods in Applied Mechanics and Engineering, 2020. **368**: p. 113043.
206. Sudakov, O., E. Burnaev, and D. Koroteev, *Driving Digital Rock towards Machine Learning: predicting permeability with Gradient Boosting and Deep Neural Networks*. 2018.
207. Alqahtani, N., et al., *Machine learning for predicting properties of porous media from 2d X-ray images.* Journal of Petroleum Science and Engineering, 2020. **184**: p. 106514.
208. Alqahtani, N.J., et al., *Flow-Based Characterization of Digital Rock Images Using Deep Learning.* SPE Journal, 2021: p. 1-12.
209. Santos, J.E., et al., *PoreFlow-Net: A 3D convolutional neural network to predict fluid flow through porous media.* Advances in Water Resources, 2020. **138**: p. 103539.
210. Chung, T., et al., *CNN-PFVS: Integrating Neural Network and Finite Volume Models to Accelerate Flow Simulation on Pore Space Images.* Transport in Porous Media, 2020. **135**(1): p. 25-37.
211. Wang, Y.D., et al., *ML-LBM: Predicting and Accelerating Steady State Flow Simulation in Porous Media with Convolutional Neural Networks.* Transport in Porous Media, 2021. **138**(1): p. 49-75.
212. Mostaghimi, P., et al., *Cleat-scale characterisation of coal: An overview.* Journal of Natural Gas Science and Engineering, 2017. **39**: p. 143-160.
213. Raeini, A.Q., M.J. Blunt, and B. Bijeljic, *Direct simulations of two-phase flow on micro-CT images of porous media and upscaling of pore-scale forces.* Advances in Water Resources, 2014. **74**: p. 116-126.
214. Tuller, M., R. Kulkarni, and W. Fink, *Segmentation of X-Ray CT Data of Porous Materials: A Review of Global and Locally Adaptive Algorithms*, in *Soil–Water–Root Processes: Advances in Tomography and Imaging*. 2013. p. 157-182.
215. Harbaugh, J.W., *Chapter 7 Carbonate Oil Reservoir Rocks*, in *Developments in Sedimentology*, G.V. Chilingar, H.J. Bissell, and R.W. Fairbridge, Editors. 1967, Elsevier. p. 349-398.
216. Biswal, B., et al., *Stochastic multiscale model for carbonate rocks.* Physical Review E, 2007. **75**(6): p. 061303.
217. Choquette, P.W. and L.C. Pray, *Geologic nomenclature and classification of porosity in sedimentary carbonates.* AAPG bulletin, 1970. **54**(2): p. 207-250.
218. Pittman, E.D., *Microporosity in carbonate rocks.* AAPG Bulletin, 1971. **55**(10): p. 1873-1878.
219. Lin, Q., et al., *Quantification of sub-resolution porosity in carbonate rocks by applying high-salinity contrast brine using X-ray microtomography differential imaging.* Advances in Water Resources, 2016. **96**: p. 306-322.
220. Peters, C.A., *Accessibilities of reactive minerals in consolidated sedimentary rock: An imaging study of three sandstones.* Chemical Geology, 2009. **265**(1): p. 198-208.
221. Othman, F., et al., *Fines migration during supercritical CO2 injection in sandstone.* Journal of Natural Gas Science and Engineering, 2018. **56**: p. 344-357.
222. Boone, M.A., et al., *3D mapping of water in oolithic limestone at atmospheric and vacuum saturation using X-ray micro-CT differential imaging.* Materials Characterization, 2014. **97**: p. 150-160.
223. Long, H., et al. *Multi-scale imaging and modeling workflow to capture and characterize microporosity in sandstone*. in *International Symposium of the Society of Core Analysts, Napa Valley, California, USA*. 2013.
224. Knackstedt, M., et al., *3D imaging and flow characterization of the pore space of carbonate core samples.* 2006.

225. Ronneberger, O., P. Fischer, and T. Brox. *U-Net: Convolutional Networks for Biomedical Image Segmentation*. in *Medical Image Computing and Computer-Assisted Intervention – MICCAI 2015*. 2015. Cham: Springer International Publishing.
226. Wan, J., et al., *Deep Learning for Content-Based Image Retrieval: A Comprehensive Study*, in *Proceedings of the 22nd ACM international conference on Multimedia*. 2014, Association for Computing Machinery: Orlando, Florida, USA. p. 157–166.
227. Alzubaidi, F., et al., *Automated lithology classification from drill core images using convolutional neural networks.* Journal of Petroleum Science and Engineering, 2021. **197**: p. 107933.
228. Niu, Y., et al., *An Innovative Application of Generative Adversarial Networks for Physically Accurate Rock Images With an Unprecedented Field of View.* Geophysical Research Letters, 2020. **47**(23): p. e2020GL089029.
229. Kamrava, S., P. Tahmasebi, and M. Sahimi, *Enhancing images of shale formations by a hybrid stochastic and deep learning algorithm.* Neural Networks, 2019. **118**: p. 310-320.
230. Varfolomeev, I., I. Yakimchuk, and I. Safonov, *An Application of Deep Neural Networks for Segmentation of Microtomographic Images of Rock Samples.* Computers, 2019. **8**(4): p. 72.
231. Janssens, N., M. Huysmans, and R. Swennen, *Computed Tomography 3D Super-Resolution with Generative Adversarial Neural Networks: Implications on Unsaturated and Two-Phase Fluid Flow.* Materials, 2020. **13**(6): p. 1397.
232. Zhu, J.-Y., et al. *Unpaired Image-to-Image Translation using Cycle-Consistent Adversarial Networks*. 2017. arXiv:1703.10593.
233. Cantrell, D.L. and R.M. Hagerty, *Microporosity in arab formation carbonates, Saudi Arabia.* GeoArabia, 1999. **4**(2): p. 129-154.
234. Irajian, A.-A., et al., *Porosity and Rock-Typing in Hydrocarbon Reservoirs Case Study in Upper Member of Dalan Formation in Kish Gas Field, South of Zagros, Iran.* Open Journal of Geology, 2016. **6**(06): p. 399.
235. Ji, Y., et al., *Characterization of Pore Geometry of Indiana Limestone in Relation to Mechanical Compaction.* Oil Gas Sci. Technol. – Rev. IFP Energies nouvelles, 2012. **67**(5): p. 753-775.
236. Ghous, A., et al. *3D Characterisation of Microporosity in Carbonate Cores*. in *SPWLA Middle East Regional Symposium*. 2007.
237. Bultreys, T., et al., *Investigating the relative permeability behavior of microporosity-rich carbonates and tight sandstones with multiscale pore network models.* Journal of Geophysical Research: Solid Earth, 2016. **121**(11): p. 7929-7945.
238. Eltom, H., et al., *MICROPOROSITY IN THE UPPER JURASSIC ARAB-D CARBONATE RESERVOIR, CENTRAL SAUDI ARABIA: AN OUTCROP ANALOGUE STUDY.* Journal of Petroleum Geology, 2013. **36**(3): p. 281-297.
239. Kingston, A., et al., *Reliable automatic alignment of tomographic projection data by passive auto-focus.* Medical Physics, 2011. **38**(9): p. 4934-4945.
240. Bultreys, T., L. Van Hoorebeke, and V. Cnudde, *Multi-scale, micro-computed tomography-based pore network models to simulate drainage in heterogeneous rocks.* Advances in Water Resources, 2015. **78**: p. 36-49.
241. Canny, J., *A Computational Approach to Edge Detection.* IEEE Transactions on Pattern Analysis and Machine Intelligence, 1986. **PAMI-8**(6): p. 679-698.
242. Lim, B., et al. *Enhanced Deep Residual Networks for Single Image Super-Resolution*. in *2017 IEEE Conference on Computer Vision and Pattern Recognition Workshops (CVPRW)*. 2017.
243. Rumelhart, D.E., G.E. Hinton, and R.J. Williams, *Learning representations by back-propagating errors.* Nature, 1986. **323**(6088): p. 533-536.

244. Drozdzal, M., et al. *The Importance of Skip Connections in Biomedical Image Segmentation*. in *Deep Learning and Data Labeling for Medical Applications*. 2016. Cham: Springer International Publishing.
245. Panichev, O. and A. Voloshyna. *U-net based convolutional neural network for skeleton extraction*. in *Proceedings of the IEEE/CVF Conference on Computer Vision and Pattern Recognition Workshops*. 2019.
246. Sørensen, T.J., *A method of establishing groups of equal amplitude in plant sociology based on similarity of species content and its application to analyses of the vegetation on Danish commons*. 1948, København: I kommission hos E. Munksgaard.
247. Dice, L.R., *Measures of the Amount of Ecologic Association Between Species.* Ecology, 1945. **26**(3): p. 297-302.
248. Lee, K., et al. *Superhuman Accuracy on the SNEMI3D Connectomics Challenge*. 2017. arXiv:1706.00120.
249. Jaccard, P., *THE DISTRIBUTION OF THE FLORA IN THE ALPINE ZONE.1.* New Phytologist, 1912. **11**(2): p. 37-50.
250. Legland, D., K. Kiêu, and M.-F. Devaux, *COMPUTATION OF MINKOWSKI MEASURES ON 2D AND 3D BINARY IMAGES.* Image Analysis & Stereology; Vol 26, No 2 (2007)DO - 10.5566/ias.v26.p83-92, 2011.
251. Legland, D. *imMinkowski*. 2021 16/4/2021]; Available from: https://www.mathworks.com/matlabcentral/fileexchange/33690-imminkowski.
252. Gostick, J., et al., *PoreSpy: A Python Toolkit for Quantitative Analysis of Porous Media Images.* Journal of Open Source Software, 2019. **4**(37).
253. Schmid, P.J. and D.S. Henningson, *Optimal energy density growth in Hagen–Poiseuille flow.* Journal of Fluid Mechanics, 1994. **277**: p. 197-225.
254. Mortensen, N.A., F. Okkels, and H. Bruus, *Reexamination of Hagen-Poiseuille flow: Shape dependence of the hydraulic resistance in microchannels.* Physical Review E, 2005. **71**(5): p. 057301.
255. Wang, Y.D., et al., *Accelerated Computation of Relative Permeability by Coupled Morphological and Direct Multiphase Flow Simulation.* Journal of Computational Physics, 2020. **401**: p. 108966.
256. Jia, F., J. Liu, and X.-C. Tai, *A regularized convolutional neural network for semantic image segmentation.* Analysis and Applications, 2021. **19**(01): p. 147-165.
257. Caliva, F., et al. *Distance Map Loss Penalty Term for Semantic Segmentation*. 2019. arXiv:1908.03679.
258. Tao, A., K. Sapra, and B. Catanzaro, *Hierarchical multi-scale attention for semantic segmentation.* arXiv preprint arXiv:2005.10821, 2020.
259. Tan, M. and Q. Le. *Efficientnet: Rethinking model scaling for convolutional neural networks*. in *International Conference on Machine Learning*. 2019. PMLR.
260. Hajizadeh, A., A. Safekordi, and F.A. Farhadpour, *A multiple-point statistics algorithm for 3D pore space reconstruction from 2D images.* Advances in Water Resources, 2011. **34**(10): p. 1256-1267.
261. Kaestner, A., E. Lehmann, and M. Stampanoni, *Imaging and image processing in porous media research.* Advances in Water Resources, 2008. **31**(9): p. 1174-1187.
262. Saenger, E.H., et al., *Digital rock physics: Effect of fluid viscosity on effective elastic properties.* Journal of Applied Geophysics, 2011. **74**(4): p. 236-241.
263. Mostaghimi, P., M. J. Blunt, and B. Bijeljic, *Computations of Absolute Permeability on Micro-CT Images*. Vol. 45. 2012.
264. ØRen, P.-E. and S. Bakke, *Process Based Reconstruction of Sandstones and Prediction of Transport Properties.* Transport in Porous Media, 2002. **46**(2): p. 311-343.
265. Armstrong, R.T., et al., *Beyond Darcy's law: The role of phase topology and ganglion dynamics for two-fluid flow.* Physical Review E, 2016. **94**(4): p. 043113.

266. Rücker, M., et al., *From connected pathway flow to ganglion dynamics.* Geophysical Research Letters, 2015. **42**(10): p. 3888-3894.
267. Liu, X., J. Sun, and H. Wang, *Numerical simulation of rock electrical properties based on digital cores.* Applied Geophysics, 2009. **6**(1): p. 1-7.
268. Zhao, J., et al., *Numerical simulation of the electrical properties of fractured rock based on digital rock technology.* Journal of Geophysics and Engineering, 2013. **10**(5).
269. Brunette, E.S., R.C. Flemmer, and C.L. Flemmer. *A review of artificial intelligence*. in *2009 4th International Conference on Autonomous Robots and Agents*. 2000.
270. Cuddy, S.J., *Litho-Facies and Permeability Prediction From Electrical Logs Using Fuzzy Logic.* 2000.
271. Kohli, A. and P. Arora, *Application of Artificial Neural Networks for Well Logs*, in *International Petroleum Technology Conference*. 2014, International Petroleum Technology Conference: Doha, Qatar.
272. Mohaghegh, S.D., *Data-Driven Reservoir Modeling*. 2017: SPE.
273. Pollock, J., et al., *Machine Learning for Improved Directional Drilling*, in *Offshore Technology Conference*. 2018, Offshore Technology Conference: Houston, Texas, USA.
274. Mohaghegh, S., et al., *Petroleum reservoir characterization with the aid of artificial neural networks.* Journal of Petroleum Science and Engineering, 1996. **16**(4): p. 263-274.
275. Mohaghegh, S., *Virtual-Intelligence Applications in Petroleum Engineering: Part 1—Artificial Neural Networks.* Journal of Petroleum Technology, 2000. **52**(09): p. 64-73.
276. Wang, Y.D., R.T. Armstrong, and P. Mostaghimi, *Enhancing resolution of digital rock images with Super Resolution Convolutional Neural Networks.* Journal of Petroleum Science and Engineering, 2019: p. 106261.
277. Balan, B., S. Mohaghegh, and S. Ameri, *State-Of-The-Art in Permeability Determination From Well Log Data: Part 1- A Comparative Study, Model Development*, in *SPE Eastern Regional Meeting*. 1995, Society of Petroleum Engineers: Morgantown, West Virginia. p. 10.
278. Zhu, L., et al., *Intelligent Logging Lithological Interpretation With Convolution Neural Networks.* Petrophysics, 2018. **59**(06): p. 799-810.
279. Rumelhart, D.E., G.E. Hinton, and R.J. Williams, *Learning internal representations by error propagation*, in *Parallel distributed processing: explorations in the microstructure of cognition, vol. 1*, E.R. David, L.M. James, and C.P.R. Group, Editors. 1986, MIT Press. p. 318-362.
280. Van der Linden, J.H., G.A. Narsilio, and A. Tordesillas, *Machine learning framework for analysis of transport through complex networks in porous, granular media: A focus on permeability.* Physical Review E, 2016. **94**(2): p. 022904.
281. Rabbani, A. and M. Babaei, *Hybrid pore-network and lattice-Boltzmann permeability modelling accelerated by machine learning.* Advances in Water Resources, 2019. **126**: p. 116-128.
282. Cire, D.C., et al., *Flexible, high performance convolutional neural networks for image classification*, in *Proceedings of the Twenty-Second international joint conference on Artificial Intelligence - Volume Volume Two*. 2011, AAAI Press: Barcelona, Catalonia, Spain. p. 1237-1242.
283. Zeiler, M.D. and R. Fergus *Visualizing and Understanding Convolutional Networks*. arXiv e-prints, 2013.
284. Chen, T. and C. Guestrin *XGBoost: A Scalable Tree Boosting System*. arXiv e-prints, 2016.
285. Keys, R., *Cubic convolution interpolation for digital image processing.* IEEE Transactions on Acoustics, Speech, and Signal Processing, 1981. **29**(6): p. 1153-1160.

286. van der Walt, S., et al., *scikit-image: image processing in Python.* PeerJ, 2014. **2**: p. e453.
287. Ioffe, S. and C. Szegedy, *Batch normalization: accelerating deep network training by reducing internal covariate shift*, in *Proceedings of the 32nd International Conference on International Conference on Machine Learning - Volume 37*. 2015, JMLR.org: Lille, France. p. 448-456.
288. Nair, V. and G.E. Hinton, *Rectified linear units improve restricted boltzmann machines*, in *Proceedings of the 27th International Conference on International Conference on Machine Learning*. 2010, Omnipress: Haifa, Israel. p. 807-814.
289. Xavier, G., B. Antoine, and B. Yoshua, *Deep Sparse Rectifier Neural Networks*. 2011, PMLR. p. 315-323.
290. Sussillo, D. and L.F. Abbott *Random Walk Initialization for Training Very Deep Feedforward Networks*. arXiv e-prints, 2014.
291. Riesenhuber, M. and T. Poggio, *Hierarchical models of object recognition in cortex.* Nature Neuroscience, 1999. **2**: p. 1019.
292. Srivastava, N., et al., *Dropout: a simple way to prevent neural networks from overfitting.* The Journal of Machine Learning Research, 2014. **15**(1): p. 1929-1958.
293. Huber, P.J., *Robust Estimation of a Location Parameter.* Ann. Math. Statist., 1964. **35**(1): p. 73-101.
294. Holland, P.W. and R.E. Welsch, *Robust regression using iteratively reweighted least-squares.* Communications in Statistics-theory and Methods, 1977. **6**(9): p. 813-827.
295. Kingma, D.P. and J. Ba, *Adam: A method for stochastic optimization.* arXiv preprint arXiv:1412.6980, 2014.
296. Abadi, M., et al. *TensorFlow: A system for large-scale machine learning*. ArXiv e-prints, 2016.
297. Bear, J., *Dynamics of Fluids in Porous Media*. 1972, Dover Publications.
298. Carman, P.C., *Flow of gases through porous media.* 1956.
299. Katz, A.J. and A.H. Thompson, *Quantitative prediction of permeability in porous rock.* Physical Review B, 1986. **34**(11): p. 8179-8181.
300. Pan, C., M. Hilpert, and C.T. Miller, *Pore-scale modeling of saturated permeabilities in random sphere packings.* Physical Review E, 2001. **64**(6): p. 066702.
301. Coenen, J., E. Tchouparova, and X. Jing. *Measurement parameters and resolution aspects of micro X-ray tomography for advanced core analysis*. 2004.
302. Fredrich, J.T., A.A. DiGiovanni, and D.R. Noble, *Predicting macroscopic transport properties using microscopic image data.* Journal of Geophysical Research: Solid Earth, 2006. **111**(B3).
303. Bhatnagar, P.L., E.P. Gross, and M. Krook, *A Model for Collision Processes in Gases. I. Small Amplitude Processes in Charged and Neutral One-Component Systems.* Physical Review, 1954. **94**(3): p. 511-525.
304. Jin, G., T.W. Patzek, and D.B. Silin, *Direct Prediction of the Absolute Permeability of Unconsolidated and Consolidated Reservoir Rock*, in *SPE Annual Technical Conference and Exhibition*. 2004, Society of Petroleum Engineers: Houston, Texas. p. 15.
305. Mostaghimi, P., B. Bijeljic, and M. Blunt, *Simulation of Flow and Dispersion on Pore-Space Images.* SPE Journal, 2012. **17**(04): p. 1131-1141.
306. Al-Kharusi, A.S. and M.J. Blunt, *Network extraction from sandstone and carbonate pore space images.* Journal of Petroleum Science and Engineering, 2007. **56**(4): p. 219-231.
307. Krizhevsky, A., I. Sutskever, and G.E. Hinton. *Imagenet classification with deep convolutional neural networks*. in *Advances in neural information processing systems*. 2012.
308. Szegedy, C., et al. *Going deeper with convolutions*. in *Proceedings of the IEEE conference on computer vision and pattern recognition*. 2015.

309. Girshick, R., et al. *Rich feature hierarchies for accurate object detection and semantic segmentation*. in *Proceedings of the IEEE conference on computer vision and pattern recognition*. 2014.
310. Sermanet, P., et al., *Overfeat: Integrated recognition, localization and detection using convolutional networks.* 2013.
311. Long, J., E. Shelhamer, and T. Darrell. *Fully convolutional networks for semantic segmentation*. in *2015 IEEE Conference on Computer Vision and Pattern Recognition (CVPR)*. 2015.
312. Lin, G., et al. *Efficient piecewise training of deep structured models for semantic segmentation*. in *Proceedings of the IEEE conference on computer vision and pattern recognition*. 2016.
313. Varfolomeev, I., I. Yakimchuk, and I. Safonov, *An Application of Deep Neural Networks for Segmentation of Microtomographic Images of Rock Samples.* 2019. **8**(4): p. 72.
314. Ar Rushood, I., et al., *Segmentation of X-Ray Images of Rocks Using Deep Learning*, in *SPE Annual Technical Conference and Exhibition*. 2020, Society of Petroleum Engineers: Virtual. p. 13.
315. Alqahtani, N., et al., *Machine learning for predicting properties of porous media from 2d X-ray images.* Journal of Petroleum Science and Engineering, 2019: p. 106514.
316. Kamrava, S., P. Tahmasebi, and M. Sahimi, *Linking Morphology of Porous Media to Their Macroscopic Permeability by Deep Learning.* Transport in Porous Media, 2019.
317. Alqahtani, N., R.T. Armstrong, and P. Mostaghimi, *Deep Learning Convolutional Neural Networks to Predict Porous Media Properties*, in *SPE Asia Pacific Oil and Gas Conference and Exhibition*. 2018, Society of Petroleum Engineers: Brisbane, Australia. p. 10.
318. Belagiannis, V., et al. *Robust optimization for deep regression*. in *Proceedings of the IEEE international conference on computer vision*. 2015.
319. Lathuilière, S., et al., *A comprehensive analysis of deep regression.* 2019.
320. Simonyan, K. and A. Zisserman *Very Deep Convolutional Networks for Large-Scale Image Recognition*. 2014. arXiv:1409.1556.
321. He, K., et al. *Deep residual learning for image recognition*. in *Proceedings of the IEEE conference on computer vision and pattern recognition*. 2016.
322. Xie, S., et al. *Aggregated residual transformations for deep neural networks*. in *Proceedings of the IEEE conference on computer vision and pattern recognition*. 2017.
323. Hong, J. and J. Liu, *Rapid estimation of permeability from digital rock using 3D convolutional neural network.* Computational Geosciences, 2020. **24**(4): p. 1523-1539.
324. Kamrava, S., P. Tahmasebi, and M. Sahimi, *Linking Morphology of Porous Media to Their Macroscopic Permeability by Deep Learning.* Transport in Porous Media, 2020. **131**(2): p. 427-448.
325. Sudakov, O., E. Burnaev, and D. Koroteev, *Driving digital rock towards machine learning: Predicting permeability with gradient boosting and deep neural networks.* Computers & Geosciences, 2019. **127**: p. 91-98.
326. Tembely, M., A.M. AlSumaiti, and W. Alameri, *A deep learning perspective on predicting permeability in porous media from network modeling to direct simulation.* Computational Geosciences, 2020. **24**(4): p. 1541-1556.
327. Tian, J., et al., *Surrogate permeability modelling of low-permeable rocks using convolutional neural networks.* Computer Methods in Applied Mechanics and Engineering, 2020. **366**: p. 113103.
328. Tian, J., et al., *Permeability prediction of porous media using a combination of computational fluid dynamics and hybrid machine learning methods.* Engineering with Computers, 2020.

329. Wu, J., X. Yin, and H. Xiao, *Seeing permeability from images: fast prediction with convolutional neural networks.* Science Bulletin, 2018. **63**(18): p. 1215-1222.
330. Riegler, G., A. Osman Ulusoy, and A. Geiger. *Octnet: Learning deep 3d representations at high resolutions*. in *Proceedings of the IEEE conference on computer vision and pattern recognition*. 2017.
331. Herring, A., et al., *Multiphase Flows in Sandstones.* 2018.
332. Wu, Z., C. Shen, and A. Van Den Hengel, *Wider or deeper: Revisiting the resnet model for visual recognition.* Pattern Recognition, 2019. **90**: p. 119-133.
333. Zhang, Q., et al. *Image segmentation with pyramid dilated convolution based on ResNet and U-Net*. in *International Conference on Neural Information Processing*. 2017. Springer.
334. Hara, K., H. Kataoka, and Y. Satoh. *Can spatiotemporal 3d cnns retrace the history of 2d cnns and imagenet?* in *Proceedings of the IEEE conference on Computer Vision and Pattern Recognition*. 2018.
335. Paszke, A., et al., *Automatic differentiation in pytorch.* 2017.
336. Caruana, R., S. Lawrence, and C.L. Giles. *Overfitting in neural nets: Backpropagation, conjugate gradient, and early stopping*. in *Advances in neural information processing systems*. 2001.
337. Botchkarev, A., *Performance metrics (error measures) in machine learning regression, forecasting and prognostics: Properties and typology.* arXiv preprint arXiv:1809.03006, 2018.
338. Lathuilière, S., et al. *Deepgum: Learning deep robust regression with a gaussian-uniform mixture model*. in *Proceedings of the European Conference on Computer Vision (ECCV)*. 2018.
339. Rothe, R., R. Timofte, and L. Van Gool, *Deep Expectation of Real and Apparent Age from a Single Image Without Facial Landmarks.* International Journal of Computer Vision, 2018. **126**(2): p. 144-157.
340. Arns, C.H. and P.M. Adler, *Fast Laplace solver approach to pore-scale permeability.* Physical Review E, 2018. **97**(2): p. 023303.
341. Gerke, K.M., et al., *Finite-difference method Stokes solver (FDMSS) for 3D pore geometries: Software development, validation and case studies.* Computers & Geosciences, 2018. **114**: p. 41-58.
342. Diskin, T., et al. *Deep robust regression*. in *2017 IEEE 7th International Workshop on Computational Advances in Multi-Sensor Adaptive Processing (CAMSAP)*. 2017.
343. Sun, K., et al. *Deep High-Resolution Representation Learning for Human Pose Estimation*. in *2019 IEEE/CVF Conference on Computer Vision and Pattern Recognition (CVPR)*. 2019.
344. Guo, Y., et al. *Deep Learning for 3D Point Clouds: A Survey*. 2019. arXiv:1912.12033.
345. Thung, K.-H. and C.-Y. Wee, *A brief review on multi-task learning.* Multimedia Tools and Applications, 2018. **77**(22): p. 29705-29725.
346. Deng, L., G. Hinton, and B. Kingsbury. *New types of deep neural network learning for speech recognition and related applications: an overview*. in *2013 IEEE International Conference on Acoustics, Speech and Signal Processing*. 2013.
347. Cao, D., et al., *Multi-task learning for digital rock segmentation and characteristic parameters computation.* Journal of Petroleum Science and Engineering, 2021: p. 109202.
348. Tatarchenko, M., A. Dosovitskiy, and T. Brox. *Octree generating networks: Efficient convolutional architectures for high-resolution 3d outputs*. in *Proceedings of the IEEE International Conference on Computer Vision*. 2017.

349. Zeng, J., et al., *Shale gas reservoir modeling and production evaluation considering complex gas transport mechanisms and dispersed distribution of kerogen.* Petroleum Science, 2021. **18**(1): p. 195-218.
350. Zhang, Q., et al., *A New Upscaling Method for Fluid Flow Simulation in Highly Heterogeneous Unconventional Reservoirs.* Geofluids, 2020. **2020**: p. 6213183.
351. Mehmani, A., S. Kelly, and C. Torres-Verdín, *Leveraging digital rock physics workflows in unconventional petrophysics: A review of opportunities, challenges, and benchmarking.* Journal of Petroleum Science and Engineering, 2020. **190**: p. 107083.
352. Tahmasebi, P., F. Javadpour, and S.F. Enayati, *Digital Rock Techniques to Study Shale Permeability: A Mini-Review.* Energy & Fuels, 2020. **34**(12): p. 15672-15685.
353. Clerke, E.A., et al., *Application of Thomeer Hyperbolas to decode the pore systems, facies and reservoir properties of the Upper Jurassic Arab D Limestone, Ghawar field, Saudi Arabia: A "Rosetta Stone" approach.* GeoArabia, 2008. **13**(4): p. 113-160.
354. Buiting, J.J.M. and E.A. Clerke, *Permeability from porosimetry measurements: Derivation for a tortuous and fractal tubular bundle.* Journal of Petroleum Science and Engineering, 2013. **108**: p. 267-278.
355. Thomeer, J.H.M., *Introduction of a Pore Geometrical Factor Defined by the Capillary Pressure Curve.* Journal of Petroleum Technology, 1960. **12**(03): p. 73-77.
356. Thomeer, J.H., *Air Permeability as a Function of Three Pore-Network Parameters.* Journal of Petroleum Technology, 1983. **35**(04): p. 809-814.

Appendix

The MICP tests are performed using POREMASTER® by Quantachrome instruments on the 6 mm core plugs after X-ray imaging. For the MICP experiment analysis, a methodology presented by [353, 354] is followed. This method fits multiple Thomeer hyperbolas [355, 356] to quantify the different pore systems in carbonates using superposition. This enables the identification of the porosity of macro- and micropores systems and their pore throat distribution. The pore volume fraction of each pore is determined based on the volume of mercury injected ***(%BV_{occ})***. The pore volume fraction obtained from the MICP for the macropore system is used to choose a safe threshold to complete the ground truth (watershed) segmentation. The pore throats distribution is estimated based on the minimum entry pressure ***(P_d)*** from Thomeer Hyperbola. The conductivity of the micropore system is then estimated based on the average pore throats for the single-phase permeability simulation. In the below figures, we show the Thomeer Hyperbolas (Figure A and B) and the pore throat distribution (Figure C) for the ILS and MEC samples.

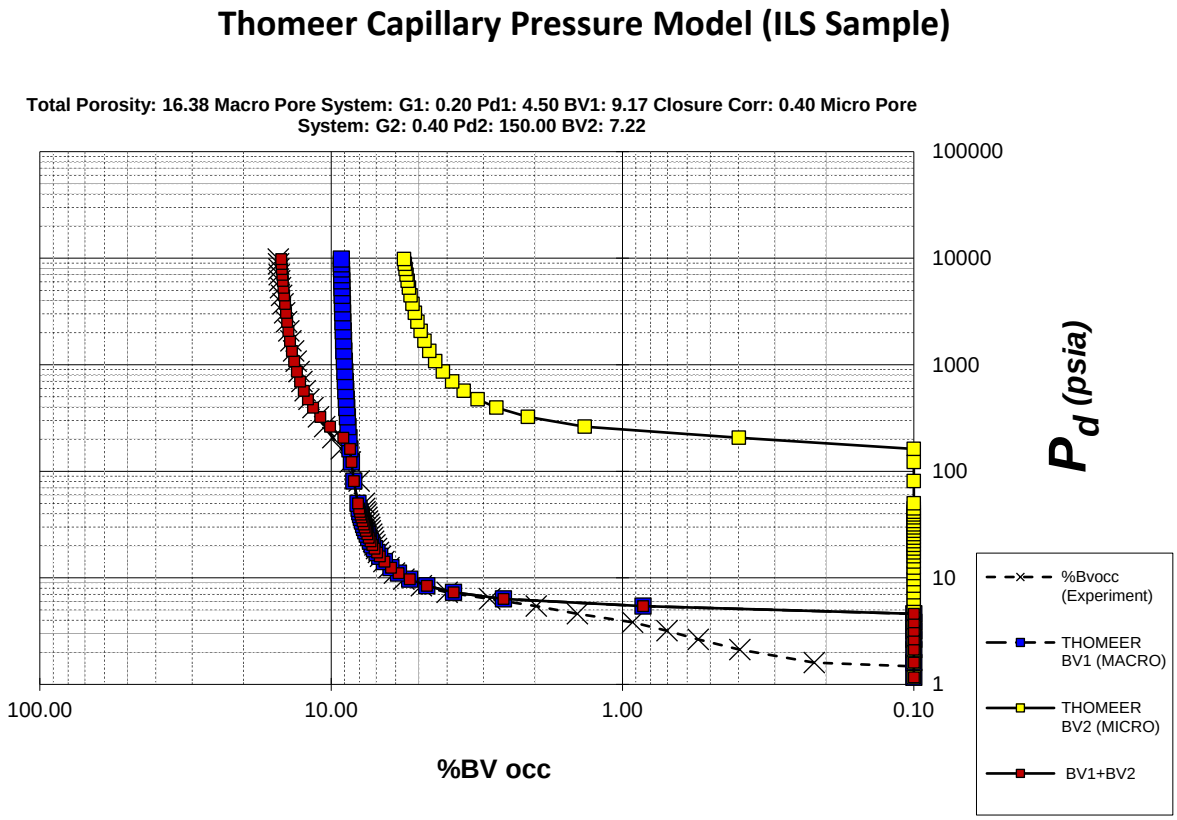

Figure A: The estimation of porosity contribution of each pore system in the ILS samples using Thomeer Hyperbola.

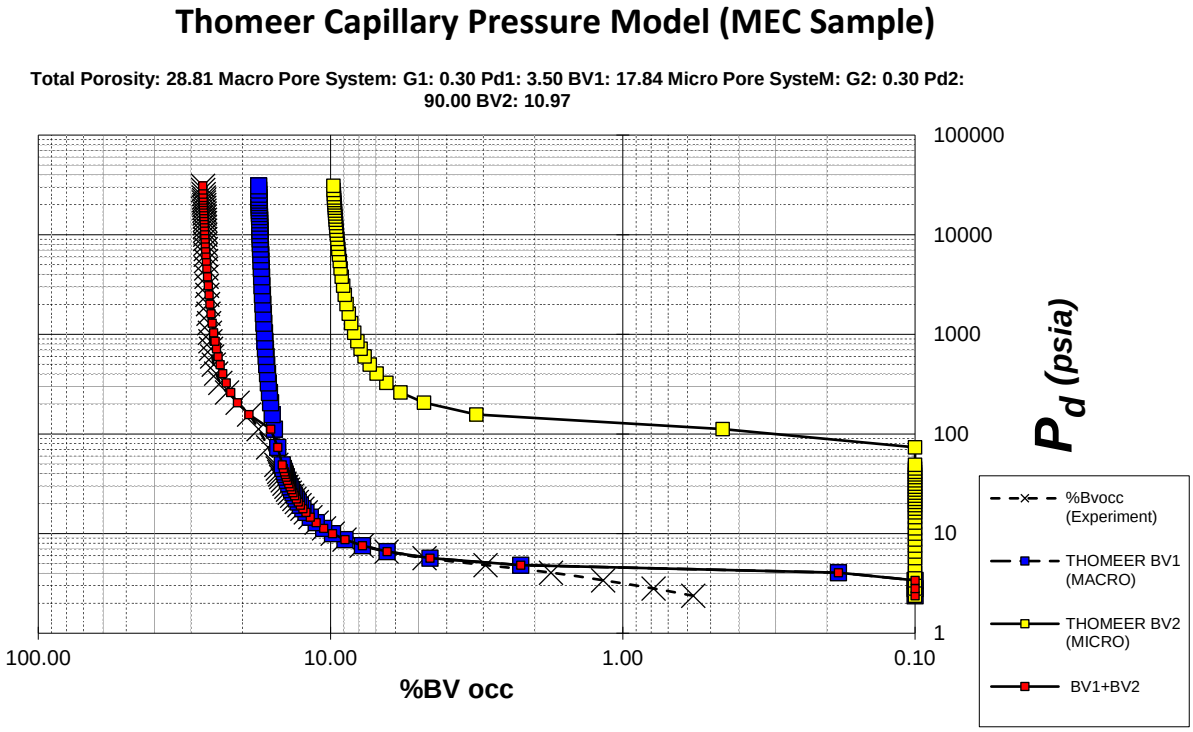

Figure B: The estimation of porosity contribution of each pore system in the MEC samples using Thomeer Hyperbola.

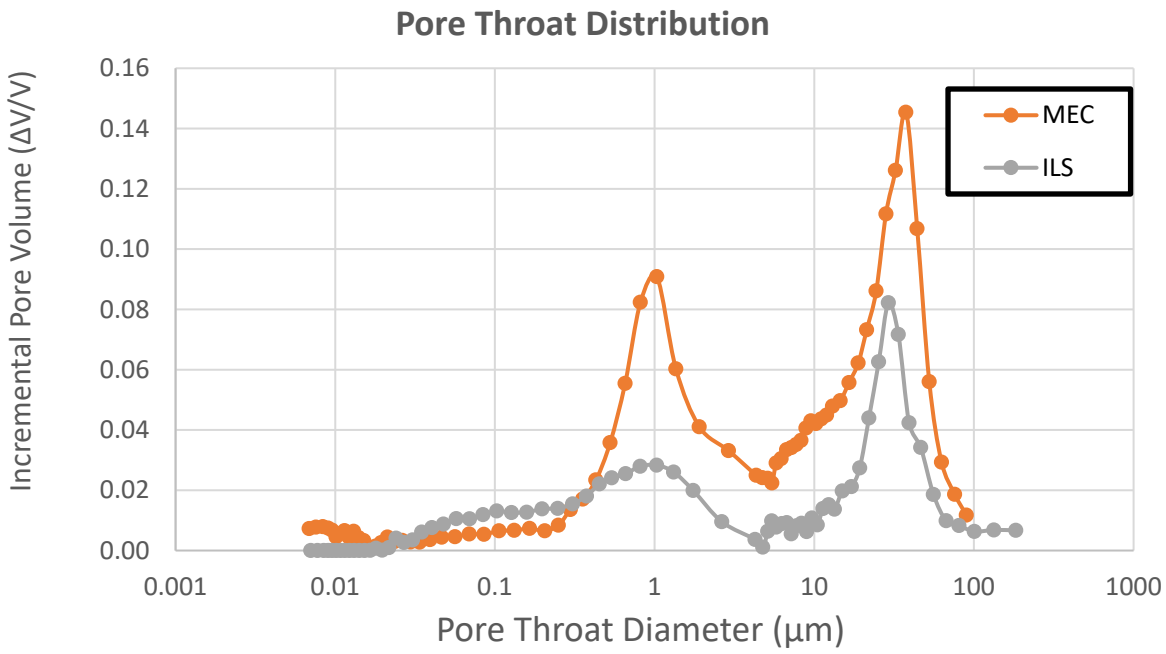

Figure C: Pore throat distribution of the ILS and MEC samples based on the MICP test